MODELING AND ESTIMATION OF SCATTERING ATTENUATION AND SCINTILLATION EFFECTS ON OPTICAL WIRELESS COMMUNICATION SYSTEMS IN SOUTH AFRICA

Olabamidele O. Kolawole

Supervised by: Professor Thomas J.O. Afullo

Dr. Modisa Mosalaosi

A thesis submitted in fulfillment of the requirement for the

degree of

Doctor of Philosophy in Electronic Engineering

School of Engineering

University of KwaZulu-Natal

South Africa

December, 2021

As the candidate's supervisor, I agree to the submission of this thesis.

Date of Submission: _____

Supervisor: _____

Professor Thomas J.O. Afullo

Declaration 1 - Plagiarism

I, **Olabamidele Olanrewaju Kolawole**, declare that:

1. The research reported in this thesis, except where otherwise indicated, is my original research.

2. This thesis has not been submitted for any degree or examination at any other university.

3. This thesis does not contain other persons' data, pictures, graphs or other information, unless specifically acknowledged as being sourced from other persons.

4. This thesis does not contain other persons' writing, unless specifically acknowledged as being sourced from other researchers. Where other written sources have been quoted, then:

a. Their words have been re-written but the general information attributed to them has been referenced

b. Where their exact words have been used, then their writing has been placed in italics and inside quotation marks, and referenced.

5. This thesis does not contain text, graphics or tables copied and pasted from the Internet, unless specifically acknowledged, and the source being detailed in the thesis and in the References sections.

Signed: ……

Declaration 2 – Publications

DETAILS OF CONTRIBUTION TO PUBLICATIONS that form part and/or include research presented in this thesis. The following journal papers emanating from this work have been either published or are in preparation for submission:

1. Visibility Modeling and Prediction for Free Space Optical Communication Systems for South Africa. *Published in International Journal on Communications Antenna and Propagation (IRECAP).*

2. Terrestrial Free Space Optical Communication Systems Availability based on Meteorological Visibility Data for South Africa. *Published in South African Institute of Electrical Engineers (SAIEE) Africa Research Journal.*

3. Analysis of Scintillation Effects on Free Space Optical Communication Links in South Africa. *Published in Photonics (MDPI) Journal.*

The following conference papers have been published during this doctoral research:

1. Estimation of Optical Wireless Communication Link Availability Using Meteorological Visibility Data for Major Locations in South Africa. *Published as conference proceedings in 2019 PhotonIcs & Electromagnetics Research Symposium - Spring (PIERS-Spring).*

2. Initial Modeling of Atmospheric Turbulence Effect on Optical Wireless Communication Links in South Africa. *Published as conference proceedings in Southern Africa Telecommunication Networks and Applications Conference (SATNAC) 2019.*

3. Initial Estimation of Scintillation Effect on Free Space Optical Links in South Africa. *Published as conference proceedings in IEEE AFRICON 2019.*

Signed: ……..

Dedication

To the Glory of the Almighty God.

Acknowledgements

First and foremost, I am eternally thankful to God Almighty, for giving me the fortitude, strength, inspiration, and endurance to overcome the challenges I experienced on this journey, and for blessing me exceedingly.

I wish to express my profound gratitude to my main supervisor, Professor Thomas J.O. Afullo, for his invaluable guidance, immeasurable support, tutelage, and patience throughout my MSc and PhD studies. I also appreciate my co-supervisor, Dr Modisa Mosalaosi, for his mentorship, constructive criticisms, and continuous belief in my abilities all through the course of this program. I have benefitted immensely from their wealth of knowledge, experience, professionalism and humanity.

My special thanks to the members of staff of the School of Electrical, Electronics and Computer Engineering, University of KwaZulu-Natal (UKZN) for all their professional guidance and support during the course of my MSc and PhD studies. Their names include but are not limited to: Professor Tom Walingo, Dr Pradeep Kumar, Dr Rudiren Carpanen, Ms. Bennedin Mokoena, Mr. Dheena Govender, Mr. Sphamandla Nqayi, Ms. Thokozani Mpisi, Mr. Thula Nzuza, Mr. Johnson Mpisi, Mr. Conrad Hlambisa, and Mr. Urajh Roopnundu.

I sincerely appreciate the members of staff of the School of Mathematics, Statistics and Computer Science, UKZN, for their expert consultations and assistance during my studies. They include but are not limited to: Ms. Princess Nhlangulela, Dr Selvan Moopanar, Dr Proscovia Namayanja and Dr Sivuyile Mgobhozi.

Words are not enough to appreciate my wife and jewel of inestimable value, Mrs Feroza Morris-Kolawole and my son, Elias Olaoluwa Kolawole for their constant love, kindness, all-round support, prayers, and encouragement. Whenever I count my blessings, you both are top of the list. I love you both with every fibre of my being. We will continue to grow and shine together!

I wish to extend my deepest gratitude to my parents: Pastor O.A. Kolawole and Mrs. G.F. Kolawole; my ever loving and kind sisters: Mrs. Gbemisola, O. Adekanmbi, Mrs. Ololade A. Gamdu and Ms. Toluwalase T. Kolawole, and my Granny: Ms. Khadijah Dawood; for all their encouragement, unwavering support, effectual prayers, understanding and patience throughout the period of my studies. Your inspiration and motivation make me strive for greater accomplishments every day.

This work would not have been possible without the unwavering support of people who surround me. I sincerely appreciate all my academic mentors, friends and colleagues such as Dr Akintunde Alonge, Dr Elijah Olurotimi, Dr Dauda Ayanda, Olukolade Ajayi, Williams Oso, Uchechukwu Maduagwu, Okikioluwa Oyedeji, Opeyemi Olalere, Dr Oluwakorede Oluyide and many others too numerous to mention.

Special thanks to the South African Weather Service (SAWS) for providing me with the data used in this thesis.

May God Almighty bless you all abundantly!

Abstract

Optical wireless communication (OWC) is a viable complementary solution for next-generation communication networks saddled with meeting the great demands of high data rates and fast internet connectivity. Its numerous advantages include: high data throughput; secure transmission; license-free spectrum; relative low cost of deployment; flexible network connectivity; etc. However, OWC system performance is severely degraded by atmospheric conditions such as fog and scintillation. Most of the proposed FSOC and hybrid FSOC systems in the literature are limited in their capacity to predict the extent to which atmospheric disturbances will impact on the performance of FSOC links in each location where they are to be deployed. This is because of the complexities involved in accessing and analyzing the information on the unique meteorological and climatic characteristics of the locations of interest prior to FSOC link deployment. This important information is necessary for determining the fade margin required by FSOC systems to withstand atmospheric disturbances in various locations of deployment. The effects of other atmospheric conditions such as gas absorption, molecular scattering, and aerosol absorption on the transmission wavelengths of interest (850 and 1550 nm) are negligible, and as such, were not considered in this study. This research, therefore, focuses on the investigation and modeling of scattering attenuation and irradiance fluctuations based on the unique climatic peculiarities of nine major cities in each of the provinces of South Africa where OWC links are to be deployed. These cities are Bloemfontein, Cape Town, Durban, Johannesburg, Kimberley, Mafikeng, Mbombela, Polokwane, and Port Elizabeth.

Meteorological data of visibility, wind speed, relative humidity, temperature, fractional sunshine, and atmospheric pressure from 1st January 2010 till 30th June 2018, for each of the locations of interest, are statistically processed and used in the investigation, estimation, and modeling of atmospheric phenomena affecting the performance of OWC signals. To achieve this, visibility modeling and prediction for OWC systems are performed using regression analysis. The results obtained show that various simple and multiple linear regression models reliably forecast visibility from other meteorological parameters considered in this study. The model's selection may be influenced not only by its performance but also by the parameters' availability. While caution is taken to avoid model over-specification, multiple linear regression models are preferable over simple regression models. The significance of the results obtained is the validated alternatives the simple and multiple linear regression models provide while saving costs and avoiding the complexities of measuring FSO visibility in the investigated locations.

The relationship between atmospheric visibility and aerosol scattering attenuation has been established by various aerosol scattering models based on the Mie scattering theory. This is made possible because the radii of aerosol particles in the atmosphere are approximately equal to the infra-red wavelengths of optical

signals. Thus, the cumulative distribution of visibility and aerosol scattering attenuations based on the Ijaz fog and Kim models for transmission wavelengths of 850 and 1550 nm in nine cities in South Africa are presented. The Ijaz fog and Kim models are also used in computing the probabilities of exceedance, deceedance, and encountering of different aerosol scattering attenuations for 850 and 1550 nm. The impact of these specific attenuations on free space optical communication (FSOC) link performance are investigated for all the various locations of interest. The results show that during foggy weather, the optical signals transmitted at 1550 nm encounter more scattering attenuation than those transmitted at the 850 nm wavelength. The reverse is the case during clear weather periods. Modeling of the minimum required visibility cumulative distribution functions (CDF) during foggy and clear weather conditions for both optical wavelengths is also presented. These CDFs are employed in evaluating the FSOC link availabilities in various cities in South Africa.

The analysis of atmospheric turbulence effects on terrestrial SISO FSOC links based on the root-mean-square (RMS) and ground wind speeds CDF, probability distribution function (PDF), and percentage of time (POT) peculiar to various cities in South Africa is presented. These wind speed distributions are used in computing the refractive index structure parameters based on the Hufnagel-Andrews-Phillips (HAP) model. The scintillation indices, as well as the effective number of large-scale and small-scale turbulence eddies, are calculated based on the modified Rytov theory and presented for periods not exceeding 50%, 99%, 99.9%, and 99.99% of the time. The scintillation profile comprising the values of these parameters is computed for Gaussian beam waves transmitted at a wavelength of 1550 nm over specific link distances for the locations of interest.

Finally, link availability, optimal link length, data rate, outage probability, and bit error rate (BER) performance analysis for intensity modulated and direct detection (IM/DD) OWC systems based on different modulation schemes while considering the effect of pointing errors, are investigated under the influence of weak, and moderate to strong atmospheric turbulence regimes in various cities in South Africa. Irrespective of the metrics used for performance evaluation, it has been shown that FSOC links transmitting at 1550 nm outperform those at 850 nm for all locations under study. This is because of the inherent characteristics of minimal absorption effects on optical signals transmitted in the short-wavelength infrared range (1530–1560 nm). Thus, playing a major role in the better BER performance of the FSOC links transmitting in this wavelength range over weak and moderate to strong atmospheric turbulence regimes as compared to those transmitting in the near IR range (780–1400 nm).

Table of Contents

List of Figures

List of Tables

List of Abbreviations

APD	Avalanche Photodiode
AR	Augmented Reality
BER	Bit Error Rate
BDPSK	Binary Differential Phase Shift Keying
BPSK	Binary Phase-Shift Keying
CDF	Cumulative Distribution Function
CI	Confidence Interval
CSIR	Council for Scientific and Industrial Research
DP-QPSK	Dual Polarization Quadrature Phase Shift Keying
eMBB	Enhanced Mobile Broadband
FESTER	First European South African Transmission ExpeRiment
FNP	Flying Network Platform
FSO	Free Space Optics
FSOC	Free Space Optical Communication
GPR	Gaussian Process Regression
GRNN	Generalized Regression Neural Network
HAP	Hufnagel-Andrews-Phillips
iBurst	High Capacity Spatial Division Multiple Access
IEEE	Institute of Electrical and Electronics Engineers
IM/DD	Intensity Modulation and Direct Detection
IMT-2020	International Mobile Telecommunications 2020
IoT	Internet of Things
IoV	Internet of Vehicles

IR	Infra-Red
ITU	International Telecommunication Union
IV	Independent variable
LOS	Line-of-Sight
MBE	Mean Bias Error
MIoT	Massive Internet of Things
MLP	Multi-Layer Perceptron Neural Network
MLR	Multiple Linear Regression
MMW	Millimeter Wave
MIMO	Multiple-Input Multiple-Output
MISO	Multiple-Input Single-Output
M-MIMO	Massive Multiple-Input Multiple-Output
mMTC	Massive Machine Type Communication
MPE	Mean Percentage Error
MR	Mixed Reality
NGN	Next-Generation Network
NR	New Radio
NRZ	Non-Return-to-Zero
OOK	On-Off Keying
O-OFDM	Optical Orthogonal Frequency Division Multiplexing
OWC	Optical Wireless Communication
PDF	Probability Distribution Function
POT	Percentage of Time
PPM	Pulse Position Modulation

QAM	Quadrature Amplitude Modulation
RF	Radio Frequency
RMS	Root-mean-square
RMSE	Root Mean Square Errors
RZ	Return-to-Zero
SAWS	South Africa Weather Service
SE	Standard Error
SIMO	Single-Input Multiple-Output
SISO	Single-Input Single-Output
SIM	Subcarrier Intensity Modulation
SLR	Simple Linear Regression
SNR	Signal-to-Noise Ratio
SSE	Error Sum of Squares
uRLLC	Ultra-Reliable Low Latency Communication
UWB	Ultra-Wide Band
VIF	Variance Inflation Factor
VR	Virtual Reality
V2X	Vehicle-to-Everything
Wi-Fi	Wireless Fidelity
WiMAX	Worldwide Interoperability for Microwave Access
3G	Third Generation
3GPP	Third Generation Partnership Project
4G	Fourth Generation
5G	Fifth Generation

List of Symbols

α	Atmospheric attenuation coefficient or Effective number of large-scale turbulence eddies.
$\alpha_a(V)$	Total extinction coefficient in decibel per unit length
a	Altitude from the reference height a_o to the height of the other (second) FSOC transceiver above the ground in metres
a_o	Height of the first FSOC transceiver above the ground in metres,
a_s	Reference height of the ground above sea level in metres
A_o	Fraction of the collected power by a circular detector aperture
$A_a(L,V)$	Scattering losses or atmospheric attenuation in dB
AP	Atmospheric pressure
A_{Rx}	Area of the receiver lens
b_0	Estimate of β_0
b_1	Estimate of β_1
b_j	Estimate of β_j
b_m	Estimate of β_m
b_{FSH}	Estimate of β_{FSH}
b_{RH}	Estimate of β_{RH}
b_s	Beam slew rate associated with a satellite moving with respect to an observer on the ground in rad/s
b_{WS}	Estimate of β_{WS}
$\beta_{sa}(\lambda), L_{Sca}$	Aerosol scattering coefficient or specific atmospheric attenuation in dB/km
β	Regression coefficient of an MLR model in vectorized form or Effective number of small-scale turbulence eddies
β_0	Intercept
β_1	Regression coefficient of the only independent variable in the SLR model
β_{FSH}	Regression coefficient of the FSH independent variable
β_I	Regression coefficient of interaction terms
β_j	Regression coefficients of the independent variables in the regression model

β_m	m^{th} slope parameter or the m^{th} regression coefficient in an MLR model
β_{RH}	Regression coefficient of the RH independent variable
β_{WS}	Regression coefficient of the WS independent variable
C	Speed of light
$corr(M_i, M_j)$	Correlation matrix
C_n^2	Refractive index structure parameter in $m^{-2/3}$
D	Diameter of the receiver aperture in metres
e_i	Residual terms
$\in$	Error term in vectorized form
$\in_i$	Error terms
ξ	Pointing error parameter
E	Mean of a variable
E_p	Energy of the photon
$erf(.)$	Error function
$erfc(.)$	Complementary error function
F	Phase front radius of curvature of the beam at the receiver
F_o	Phase front radius of curvature of the beam at the transmitter
$F[V_{\min}]$	CDFs of minimum required visibilities
F_A , F_a	Excess noise factor
$f_I(I)$	PDF of the Gamma-gamma turbulence distribution
$F_I(I)$	CDF of the Gamma-gamma turbulence distribution
F_n	Amplifier noise figure
$f_\gamma(\gamma)$	SNR PDFs based on the Lognormal and Gamma-gamma turbulence models
$F_\gamma[\gamma_{th}]$	CDF of the instantaneous SNR
F_{SL}	Free space path loss in dB
FSH	Fractional sunshine
g , g_a	APD gain
G_{Rx}	Gain of the receive lens in dB
G_{Tx}	Gain of the transmit lens in dB

$G_{u,v}^{s,t}$	Meijer G function
$\Gamma(\bullet)$	Gamma function
h	Planck's constant
H_0	Null hypothesis
H_1	Alternative hypothesis
I	Dimensions of the in-phase signals
I	Signal intensity
I_0	Transmitted signal intensity
J	Dimensions of the quadrature signals
λ	Wavelength of an optical signal
$\lambda_\circ$	Maximum spectrum wavelength of the solar band
k	Wave number of the plane wave in m^{-1}
k_A , k_a	Ionization factor
K_B , K_b	Boltzmann constant
$K_{\alpha-\beta}(\bullet)$	Modified Bessel function of the second kind and of order $\alpha-\beta$
L	Propagation distance in km
L_{Av}	Link availability
L_b	Lower bound term
L_{Geo}	Optical geometric loss in dB
$L_m(L)$	Optical link margin
$L_m(L)_{\text{Link A}}$	Link margin for FSO link A
$L_m(L)_{\text{Link B}}$	Link margin for FSO link B
l_o	Inner scale of turbulence
L_o	Outer scale of turbulence
M	Scaling factor or even number of bits per symbol for square constellations
MLR_{ALL}	Multiple linear regression model containing the RH, FSH and WS predictor variables
n	Actual amount of sunshine hours in a day
N	Maximum possible amount of daylight hours
$\boldsymbol{N}$	Normal distribution
N_b	Receiver sensitivity in watts

Ns	Number of samples
η_x	Nondimensional low-pass cutoff frequency
η_{xo}	Artificial quantity
$P(e\|\gamma)$	Conditional BER performance of the FSO link based on a specific modulation scheme
$p(I)$, $f_I(I)$	Probability distribution function (PDF) of a lognormal variable
P_{BPSK}	BER of BPSK SISO FSOC links in the presence of atmospheric turbulence and pointing errors
$P_{BPSK}(e/\gamma)$	Conditional BER for BPSK SISO FSOC links in the absence of atmospheric turbulence
$P_{(I\times J)QAM}$	BER of I × J rectangular SIM-QAM SISO FSOC links in the presence of atmospheric turbulence and pointing errors
$P_{(I\times J)QAM}(e/\gamma)$	Conditional probability of error for I × J rectangular SIM-QAM signals in the absence of atmospheric turbulence
p_j	Coefficients of the minimum required visibility polynomial
P_{MQAM}	BER of M-ary square SIM-QAM SISO FSOC links in the presence of atmospheric turbulence and pointing errors
$P_{MQAM}(e/\gamma)$	Conditional probability of error for M-ary square SIM-QAM signals in the absence of atmospheric turbulence
P_{Tx}	Power of the transmitted optical signal in dBm
P_{Rx}, P_x	Average optical power detected at the receiver in dBm
P_{RZ-OOK}	BER of RZ-OOK SISO FSOC links in the presence of atmospheric turbulence and pointing errors
$P_{RZ-OOK}(e/\gamma)$	Conditional BER for RZ-OOK SISO FSOC links in the absence of atmospheric turbulence
p-value	Probability value
q	Charge of an electron
$q_\circ$	Particle size distribution parameter
Q_l	Nondimensional inner-scale parameter
Q_o	Nondimensional outer-scale parameter

$Q(\cdot)$	Q-function of a random variable
r	Radius of a circular detector aperture
R	Correlation coefficient
R	APD load resistance
$\Re$	Responsivity
R_b	Bit rate
R_D	Data rate
R_s	Sensitivity of the receiver in dBm
R^2	Coefficient of Determination
R_m^2	Coefficient of determination (R^2) obtained by regressing the m^{th} predictor on the remaining predictors in an MLR model
R_{FSH}^2	Coefficient of determination obtained by regressing FSH on the RH and WS independent variables
R_{RH}^2	Coefficient of determination obtained by regressing RH on the FSH and WS independent variables
R_{WS}^2	Coefficient of determination obtained by regressing WS on the RH and FSH independent variables
RH	Relative humidity
θ	Transmit beam divergence angle in radians
Θ_o	Beam curvature parameter at the transmitter
Θ_1	Curvature parameter of the beam at the receiver
Λ_o	Fresnel ratio of the beam at the transmitter
Λ_1	Fresnel ratio of the beam at the receiver
T	Receiver temperature
$tStat$	t-statistic
T_{th}	Optical threshold
$Temp$	Temperature
τ_{Rx}	Receiver efficiency
τ_{Tx}	Transmitter efficiency
$\tau(\lambda, L)$	Transmittance of the atmosphere in km^{-1}
U_b	Upper bound term

V	Meteorological visual range in km
$V_{\min}(L,V)$	Minimum required visibility
VIF	Variance inflation factor
VIF_{FSH}	Variance inflation factor obtained by regressing *FSH* (output) on *RH* and *WS*
VIF_{RH}	Variance inflation factor obtained by regressing *RH* (output) on *FSH* and *WS*
VIF_{RH+WS}	Variance inflation factor obtained by regressing *RH+WS* (output) on *FSH*
VIF_{RH-WS}	Variance inflation factor obtained by regressing *RH-WS* (output) on *FSH*
VIF_{WS}	Variance inflation factor obtained by regressing *WS* (output) on *RH* and *FSH*
$\text{VIF}_{FSH\times WS}$	Variance inflation factor obtained by regressing *FSH*×*WS* (output) on *RH*
VSB_{ALL}	Estimated visibility using the MLR model containing the RH, FSH and WS predictor variables.
VSB_{AP}	Estimated visibility from the AP predictor variable
VSB_{BLOEM}	Estimated visibility using the best MLR model for Bloemfontein
VSB_{DBN}	Estimated visibility using the best SLR model for Durban
VSB_{FSH}	Estimated visibility from the FSH predictor variable
$VSB_{FSH\times WS}$	Estimated visibility using the MLR model containing interaction terms $FSH\times WS$ and the RH predictor variable
VSB_{JHB}	Estimated visibility using the best MLR model for Johannesburg
VSB_{KIM}	Estimated visibility using the best MLR model for Kimberley
VSB_{M}	Measured visibility
VSB_{MPU}	Estimated visibility using the best MLR model for Mpumalanga
VSB_{PE}	Estimated visibility using the best SLR model for Port Elizabeth
VSB_{POL}	Estimated visibility using the best MLR model for Polokwane
VSB_{RH}	Estimated visibility from the RH predictor variable
$VSB_{RH\&FSH}$	Estimated visibility using the MLR model containing the RH and FSH predictor variables.
VSB_{RH+WS}	Estimated visibility using the MLR model containing interaction terms $RH+WS$ and the FSH predictor variable
VSB_{RH-WS}	Estimated visibility using the MLR model containing interaction terms $RH-WS$ and the FSH predictor variable
VSB_{Temp}	Estimated visibility from the $Temp$ predictor variable

VSB_{WS}	Estimated visibility from the WS predictor variable
σ^2	Variance
σ_1^2	Rytov variance for a plane wave
σ_B^2	Rytov variance for a Gaussian-beam wave
σ_G^2	Rytov variance for a Gaussian-beam wave with inner scale
σ_x^2	Normalized large-scale (refractive) variance
σ_y^2	Normalized small-scale (diffractive) variance
σ_{Inx}^2	Large-scale log–irradiance variance
σ_{Iny}^2	Small-scale log–irradiance variance
σ_N^2 , σ_n^2	Total APD receiver noise
σ_s	Standard deviation of the jitter at the receiver
σ_{Sh}^2	Shot noise
σ_{SI}^2	Scintillation index parameter
σ_{sw}^2	Rytov variance for the spherical wave
σ_{Th}^2	Thermal noise
W_o	Beam radius at the transmitter
W_1	Beam radius in free space at the receiver
W_g	Ground wind speed in m/s
W_i , w_i	Weights of the Hermite polynomial
W_L	Beam waist of a Gaussian beam
W_{Leq}	Equivalent beam waist or radius at the receiver
W_{rms}	Root-mean-square (RMS) wind speed in m/s
WS	Wind speed
x_i	Independent variable
x_{im}	mth Independent variable of an MLR model
$\overline{x}$	Sample means of random variable **X**
X	Independent variable of an MLR model in vectorized form
X_{Rx}	Aggregate loss at the receiver in dB
X_{Tx}	Aggregate loss at the transmitter in dB

γ_o	Instantaneous SNR at the receiver
$\bar{\gamma}$	Average SNR at the receiver
γ_{th}	Threshold SNR
y_i	Output/dependent variable
$\hat{y}_i$	Estimate of y_i
$\bar{y}$	Sample means of random variable **Y**
Y	Output/dependent variable of an MLR model in vectorized form
z_i	Zeros of the Hermite polynomial

Chapter 1

1 Introduction

1.1 Background of the Study

Optical wireless communication (OWC) technology generally known as Free-space optical communication (FSOC) is a bidirectional, line-of-sight (LOS) communication that uses the atmosphere as an unguided propagation medium of optically modulated information signals. FSOC systems use a combination of electrical-to-optical circuits to transmit user information onto an optical carrier, and then use optical-to-electrical circuits to convert back to the electrical domain at the receiver [1]-[3].

FSOC systems have gained tremendous research and commercial attention over the last few decades due to the numerous advantages they provide and the development margins they exhibit. The high data rate transmission and unrivaled user data security level they provide, as well as the comparatively cheap operational cost and license-free installation, are some of the reasons why FSOC links are used in contemporary communication networks [4]-[6]. Indeed, FSOC is a promising complementary solution platform for 5G backhaul networks, whether as a standalone or hybrid technology[4], [7]. Many of the limitations of microwave communication are not present in FSOC links [7].

In spite of their numerous features and prospective applications, FSOC systems have yet to gain widespread commercial adoption. This is due to the fact that performance, dependability, and availability of FSOC systems, are highly susceptible to atmospheric and meteorological conditions as the laser beam propagates through the atmosphere [7], [8]. Attenuation due to absorption and scattering is a significant factor that affects the performance of FSOC links and can cause major performance deterioration or even outages in dense fog, snow, haze, dust or rainy weather ([1], [2], [6], [9]-[12]). This is because the composition of the atmosphere, particularly during foggy weather, has similar particle size distributions compared with the size of infra-red (IR) wavelengths. This could cause the IR optical beam to be scattered or absorbed, which would lower the performance and availability of the FSOC link [13], [14].

Absorption and scattering of information-carrying photons may result in loss of signal power and redirection of LOS communication at the receiver. Consequently, both impairments result in erroneous data recovery at the receiver [1], [7]. Several specific attenuation models have been developed to estimate the

aerosol scattering attenuation based on meteorological visibility ranging from 0.1 – 50 km over transmission wavelengths of 400 – 1550 nm [15]-[19].

The Kruse model was developed mainly for estimating scattering attenuation during haze conditions for optical to near infra-red (IR) wavelengths over visibility ranges of 0–50 km. However, the Kruse model is not suitable for visibility under fog conditions [18], [19]. The Nabousli et al. model was developed for wavelengths of 690–1550 nm for visibility in the presence of advection and radiation fog conditions. The optical threshold for the models was not stated, and the models are not suitable for estimating scattering attenuation in haze and clear weather conditions [15], [18].

The Grabner et al. and Nadeem et al. models were both developed from empirical data of visibility under fog conditions for two optical wavelengths of 830 and 1550 nm. Both models are clearly not independent models because their root mean square errors (RMSE) are quite large when compared to other universal models; thus, they are only suitable for the specific locations for which they were developed [17], [18], [20]. Ferdinandov et al. proposed new empirical models for aerosol and molecular scattering coefficients in the lower troposphere using analytical methods. These models were developed for wavelengths of 300–1100 nm and visibility ranges of 0.1–50 km. However, the Ferdinandov models are not verified by experimental work, and there are clear differences in the performance of the models when compared with other independent models [16], [18].

The Ijaz fog model was developed to investigate fog attenuation of optical signals for visibilities between 1 and 1000 metres. The model performance indicates that the scattering attenuation results are valid for wavelengths of 600–1600 nm, where the results show that fog attenuation is wavelength dependent for all ranges of visibility considered. This is in contrast to the claim by the Kim model that fog attenuation is independent of all optical wavelength ranges for visibilities less than 500 metres [18], [19], [21]. The Kim model is a modification of the Kruse model, and it was developed to correct the misconception that optical signals transmitted at a wavelength of 1550 nm were less affected by aerosol scattering attenuation when compared with shorter wavelengths of 780 and 850 nm. The Kim models are suitable for estimating scattering attenuation of optical signals for visibility under haze and clear weather conditions but unsuitable for fog investigations [18], [19], [21].

Furthermore, in clear sunny weather with negligible aerosols, atmospheric turbulence, which generates the scintillation effect, degrades the performance of the FSOC links. Atmospheric turbulence causes random fluctuations in the refractive index of the atmospheric medium. Along the propagation path, temperature

changes and/or mixing of hot and cold air masses generate pockets of eddies of varied densities. These turbulence eddies result in intensity and phase variations in information-carrying photons, which may result in irreversible information loss [22]-[25]. Some optical scintillation models for plane, spherical and Gaussian beam waves taking into account the absence and presence of microscale and macroscale turbulence eddies have been investigated and reported in [26]-[28].

Various mathematical models, such as gamma–gamma, log-normal, k-distribution, and negative exponential models, have been researched and proposed to characterize the influence of turbulence on FSOC information signals [1], [2]. Turbulence can be classified as weak, moderate, or strong depending on the degree of intensity scintillations induced by the existence of turbulence eddies. The log-normal model is best suited for received signal characterization during weak turbulence conditions, while the negative exponential model is best suited for strong turbulence conditions only; however, the gamma–gamma model has been found to be ideal for characterizing moderate to strong turbulence conditions [1], [9]. All of these atmospheric impairments have been thoroughly investigated theoretically, and multiple channel models have been developed in order to evaluate the key metrics of a communication system, such as outage probability, bit error rate, and so on [21], [29], [30].

1.2 Problem Formulation and Motivation

The performance of FSOC links are highly susceptible to climatic and weather conditions in locations of deployment, as well as physical phenomena [7], [8]. The majority of proposed FSOC and hybrid FSOC systems in literature are limited in their capacity to predict the extent to which atmospheric disturbances will impact on the performance of FSOC links in each location where they are to be installed. This is because the information and computational analyses of the unique meteorological and climatic characteristics of the locations of interest are usually not studied prior to FSOC deployment. This information is very important for determining the required fade margin for FSOC systems so that designed links can withstand atmospheric impairments in their various locations of deployment. It is therefore imperative to thoroughly investigate and estimate the extent to which various atmospheric phenomena will impact on the performance and availability of FSOC links in locations of interest. In this thesis, the South African geographical space is the area of focus with keen interest in nine cities, one in each of the provinces of South Africa. These cities are: Bloemfontein, Cape Town, Durban, Johannesburg, Kimberley, Mafikeng, Mbombela, Polokwane and Port Elizabeth. These selected cities are urban places with considerable population, hence great demand for high data rates and fast internet connectivity.

The climate of South Africa is considered highly variable spatially and temporally. The spatial variations in elevation across the country contribute significantly to this diversity. The Council for Scientific and Industrial Research (CSIR) developed the Köppen-Geiger climate classification for South Africa, which characterizes the country as semi-arid with influences from temperate and tropical zones [31], [32]. Northern steppe climates may be found at Mafikeng, Kimberley, and Bloemfontein; Bloemfontein has cold arid weather, whereas Mafikeng and Kimberley are mostly arid and hot. The climates of Johannesburg and Mbombela are mildly temperate, with the former being high-veld and the latter being low-veld. Durban has a humid subtropical climate, but Cape Town has a Mediterranean climate, with warm summers and rainy winters. Polokwane has an arid Bush-veld climate with hot summers and chilly winters, whereas Port Elizabeth has a southern coastal climate with rain throughout the year [33]-[35]. The aim of this study is to determine the attenuations based on the atmospheric conditions peculiar to all the climatic zones of South Africa.

1.3 Research Objectives

1) To determine regression models based on meteorological parameters to reliably forecast atmospheric visibility in all the locations of interest.
2) To compute the probabilities of exceedance, deceedance and encountering of different aerosol scattering attenuations for 850 and 1550 nm FSOC links from meteorological visibility data collected for various cities in South Africa.
3) To model the minimum required visibility CDFs during foggy and clear weather conditions for 850 and 1550 nm FSOC links in order to compute the availability of these links in the aforementioned locations.
4) To compute the scintillation profile for Gaussian beam FSOC signals using the modified Rytov theory for various locations in South Africa over periods that do not exceed 50%, 99%, 99.9%, and 99.99% of the time.
5) To investigate the outage probability and bit error rate (BER) analysis for FSOC links employing different modulation schemes while considering the effect of pointing errors over weak, moderate to strong atmospheric turbulence regimes in various cities of South Africa.

1.4 Contributions

Six research articles were directly influenced by the research undertaken in preparation for this thesis: three conference papers and three journal articles. Each article's title, authors, type, publication status, and brief synopsis are provided. The three journal papers for which the candidate is acknowledged as the lead author are presented in the following chapters of this thesis (i.e. Articles 1, 3 and 6).

1.4.1 Article 1

Title	Visibility Modeling and Prediction for Free Space Optical Communication Systems for South Africa
Authors	Olabamidele O. Kolawole, Modisa Mosalaosi and Thomas J.O. Afullo
Type	Journal Paper
Status	Published in *International Journal on Communications Antenna and Propagation (IRECAP)*, 2020, vol. 10, no. 3, DOI: 10.15866/irecap.v10i3.18008
Summary	This paper proposes regression models based on meteorological parameters to reliably estimate atmospheric visibility. For Cape Town, South Africa, the meteorological parameters utilized were relative humidity, temperature, fractional sunshine, air pressure, and wind speed. The results obtained show that various simple and multiple linear regression models adequately predict visibility. While caution is taken to avoid model over-specification, multiple linear regression models are preferable over simple linear regression models. The significance of the model parameters is achieved in the case of multiple linear regression models by limiting the impacts of multicollinearity. The model's selection may be influenced not only by its performance but also by the availability of the parameters. The methodology used in deriving the regression models for Cape Town, were also extended to seven other major cities spatially located within the South African geographical space; and their results presented therein. This study shows that meteorological parameters at a location can be utilized to model and perhaps forecast optical signal visibility.

1.4.2 Article 2

Title	Estimation of Optical Wireless Communication Link Availability Using Meteorological Visibility Data for Major Locations in South Africa
Authors	Olabamidele O. Kolawole, Thomas J.O. Afullo and Modisa Mosalaosi
Type	Conference Paper
Status	Published in *Proceedings of the 2019 PhotonIcs & Electromagnetics Research Symposium - Spring (PIERS-Spring)*, June 2019. DOI: 10.1109/PIERS-Spring46901.2019.9017842
Summary	This paper presents the cumulative distributions of visibility under fog conditions from data spanning 8 years; based on visibility measurements for average worst month, worst year and hour most fog events occurred in a major city in each of the nine provinces of South Africa. The fog cumulative distribution based on average worst month

measurements was then converted into Mie scattering attenuation distributions for OWC links propagating at 850nm using the Kim and Ijaz Fog models. The availability of a typical 850 nm OWC link is then calculated for all the desired locations of interest. The results presented show that the links in the province of Mpumalanga and the coastal cities of Cape Town and Port Elizabeth are highly susceptible to aerosol scattering attenuations; hence their noticeable degradation in availability over link distances between 0 – 1 km.

1.4.3 Article 3

Title	Terrestrial Free Space Optical Communication Systems Availability based on Meteorological Visibility Data for South Africa
Authors	Olabamidele O. Kolawole, Thomas J.O. Afullo and Modisa Mosalaosi
Type	Journal Paper
Status	Published in *South African Institute of Electrical Engineers (SAIEE) Africa Research Journal*, 2022, vol. 113, no. 1, DOI: 10.23919/SAIEE.2022.9695423
Summary	This journal paper expands on the previous study done in Article 2. Statistical evaluation of meteorological visibility data collected for various cities in South Africa is employed in the computation of the probabilities of exceedance, deceedance and encountering of different aerosol scattering attenuations for 850 and 1550 nm FSOC links. This was achieved after the analysis of the cumulative distribution of visibility and aerosol scattering attenuations based on the Ijaz and Kim models for the aforementioned links. Thereafter, the link margin equations derived, were implemented in evaluating and modeling of the minimum required visibility CDFs for two FSOC links in foggy and clear weather conditions. These computations were then implemented in determining the availability performances for two commercial FSOC links. Achievable SNRs, data rates, and BERs for FSOC systems employing IM/DD with non-return-to-zero on-off keying (NRZ-OOK) modulation under the influence of weak turbulence are presented for all the locations of interest. Due to their high wind velocities, altitudes, and refractive index structure parameter values, the links deployed in the cities of Mafikeng and Kimberley have the lowest BER performances as shown in the results. Also, the 1550 nm FSO link outperforms the one transmitting at 850 nm based on all the performance metrics used.

1.4.4 Article 4

Title	Initial Modeling of Atmospheric Turbulence Effect on Optical Wireless Communication Links in South Africa

Authors	Olabamidele O. Kolawole, Thomas J.O. Afullo and Modisa Mosalaosi
Type	Conference Paper
Status	Published in *Proceedings of the Southern Africa Telecommunication Networks and Applications Conference (SATNAC) 2019,* Sept. 2019
Summary	In places where the aerosol scattering effects of fog are negligible, irradiance fluctuations are primarily responsible for the losses experienced by transmitted optical signals. The objective of this conference paper was to model the effect of irradiance fluctuations on optical plane wave signals for horizontal-path propagation using the modified Rytov theory for major cities across South Africa. According to the results, conventional OWC links deployed for usage in Kimberley and Mafikeng would encounter greater atmospheric turbulence losses than links deployed for use in the coastal cities of Port Elizabeth, Durban, and Cape Town. This is because the inland cities of Kimberley and Mafikeng have high altitudes above sea level and greater refractive index structure parameter values. The refractive index structure parameter values were computed using the modified Hufnagel-Valley model.

1.4.5 Article 5

Title	Initial Estimation of Scintillation Effect on Free Space Optical Links in South Africa
Authors	Olabamidele O. Kolawole, Thomas J.O. Afullo and Modisa Mosalaosi
Type	Conference Paper
Status	Published in *Proceedings of the IEEE AFRICON Conference 2019,* Sept. 2019. DOI: 10.1109/AFRICON46755.2019.9134032
Summary	With similar objectives to Article 4, this conference paper investigates the impact of irradiance fluctuations on FSOC links based on the horizontal-path transmission of spherical and plane wave optical signals using the modified Rytov theory for major locations across South Africa. The results obtained also show that FSOC links deployed to places with high altitudes, ground wind speeds, and refractive index structure parameter values based on the modified Hufnagel-Valley model (Kimberley, Mafikeng, and Johannesburg) experience more scintillation losses than coastal cities (Cape Town, Durban, and Port Elizabeth) due to their much lower altitudes. In spite of the small differences in the optimal link distances achieved between FSOC links transmitting spherical and plane wave optical signals, optical plane wave fronts cover more link lengths when propagating information signals between FSOC transceivers.

1.4.6 Article 6

Title	Analysis of Scintillation Effects on Free Space Optical Communication Links in South Africa
Authors	Olabamidele O. Kolawole, Thomas J.O. Afullo and Modisa Mosalaosi
Type	Journal Paper
Status	Published in *Photonics (MDPI) Journal*, 2022, vol. 9, no. 7, DOI: 10.3390/photonics9070446
Summary	The analysis of the impacts of atmospheric turbulence on terrestrial SISO FSOC links based on wind speeds prevalent in several South African cities is presented in this journal paper. Ground wind speed data from the SAWS was statistically processed, and the resultant CDF, PDF, and percentage of time plots for each location of interest are shown. The refractive index structure parameters based on ground and root-mean-square (RMS) wind speeds in clear and sunny weather are calculated using the Hufnagel-Andrews-Phillips (HAP) model. The scintillation index values not exceeded 50%, 99%, 99.9%, and 99.99% of the time; based on the zero inner scale and infinite outer scale model and finite inner scale and finite outer scale model, are computed for Gaussian beam waves. Aerosol scattering losses based on visibilities not exceeding 50%, 99%, 99.9%, and 99.99% of the time are presented for several South African cities. Outage probability and BER analysis are then performed for OOK, BPSK, and SIM-QAM SISO FSOC links deployed at various locations of interest, while taking into consideration the influence of pointing errors over weak and moderate to strong atmospheric turbulence regimes.

1.5 Thesis Overview

This chapter introduces the background of this study. It also provides the problem formulation and motivation, as well as the research contributions that have been made.

Chapter 2 presents the regression models based on meteorological factors in order to reliably estimate atmospheric visibility. Simple linear regression (SLR) and multiple linear regression (MLR) techniques are employed. Meteorological data from January 2010 until December 2017 for Cape Town was obtained from the South African Weather Service (SAWS) and various regression models are derived from it. The meteorological parameters considered are relative humidity, temperature, fractional sunshine, atmospheric pressure, wind speed, and visibility. The average monthly values of these weather factors from January

2010 until December 2016 are computed and presented in Table 1.1. For the SLR models, each of the meteorological parameters is regressed against atmospheric visibility as shown in Figures 1.1-1.5.

Additional information about the SLR and MLR models, as well as the various tests used to investigate model performance, such as normality, variance, standard error, and so on, is provided. Two approaches to combating the effects of multicollinearity in the MLR models where the significance of some predictors may be diminished, namely, the removal of highly correlated predictors and the introduction of interaction terms, are presented. The results of the performance of the SLR and MLR models when tested with measured average visibility data from January to December 2017 are analysed. These regression techniques are also carried out on other cities in South Africa, and the models are presented.

Table 1.1: Average monthly measured visibility, relative humidity, temperature, fractional sunshine hours, atmospheric pressure, and wind speed values from 2010 – 2016.

Average Visibility (km)	Average Relative Humidity (%)	Average Temperature (^{o}C)	Average Fraction of Sunshine Hours	Average Atmospheric Pressure (mb)	Average Wind Speed (m/s)
28.27	67.37	22.01	0.7962	1007.42	6.67
28.56	68.11	21.69	0.8045	1007.40	6.11
26.39	70.94	20.30	0.7362	1009.00	5.44
25.34	71.54	17.50	0.7258	1012.08	4.64
20.91	77.20	15.04	0.6013	1012.85	4.01
20.57	76.59	12.79	0.5701	1014.87	4.03
23.26	75.76	12.50	0.6309	1016.77	3.96
21.89	75.31	13.16	0.6011	1014.07	4.36
24.41	70.94	14.39	0.6369	1014.37	4.63
26.56	67.99	16.90	0.7180	1012.13	5.30
27.87	65.61	18.49	0.7460	1010.85	6.21
30.49	65.43	20.99	0.8201	1008.78	6.44

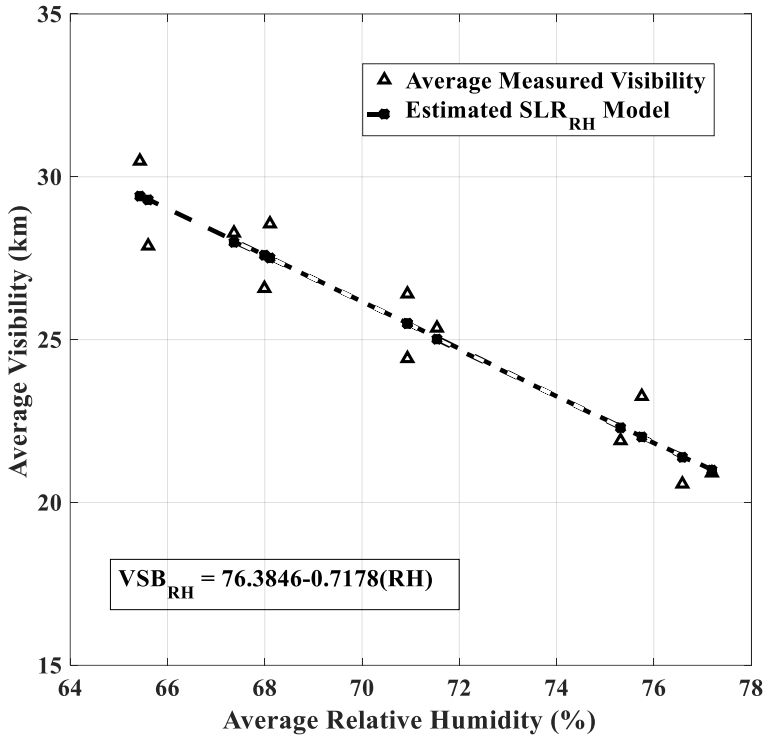

Figure 1.1: Average visibility (km) against average relative humidity (%).

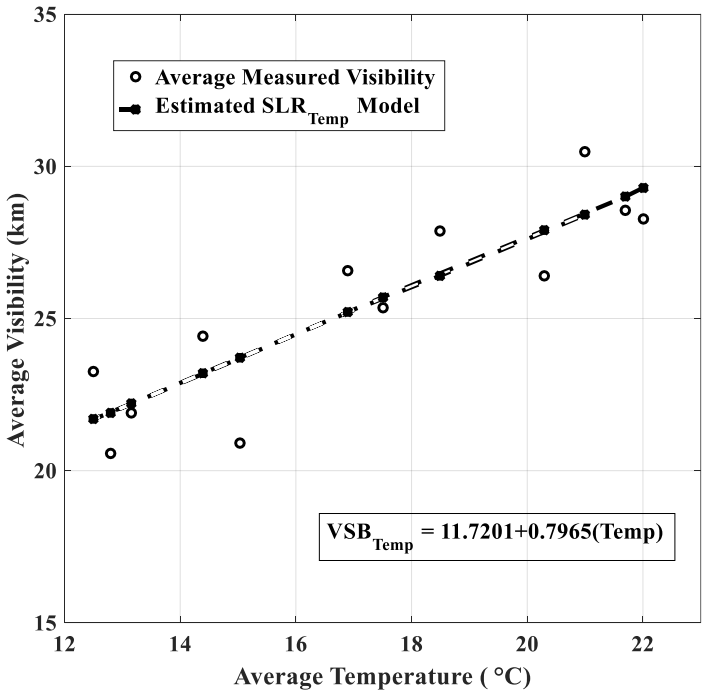

Figure 1.2: Average visibility (km) against average temperature (^{o}C).

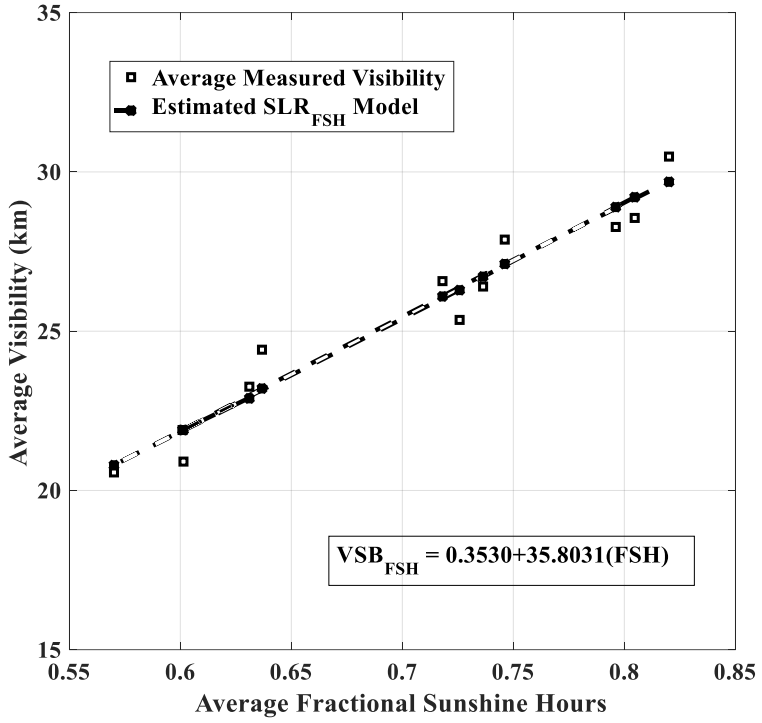

Figure 1.3: Average visibility (km) against average fractional sunshine hours.

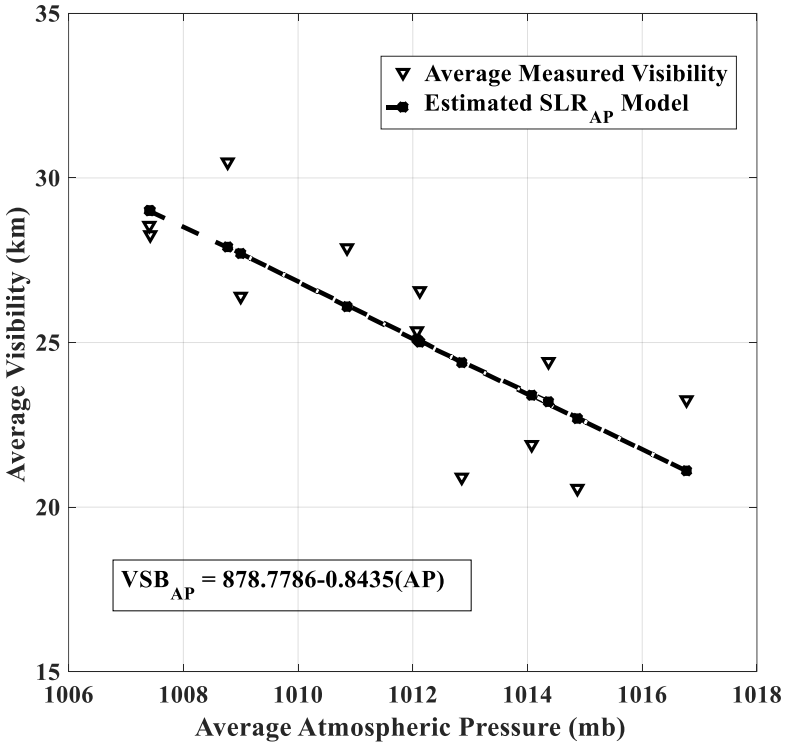

Figure 1.4: Average visibility (km) against average atmospheric pressure (mb).

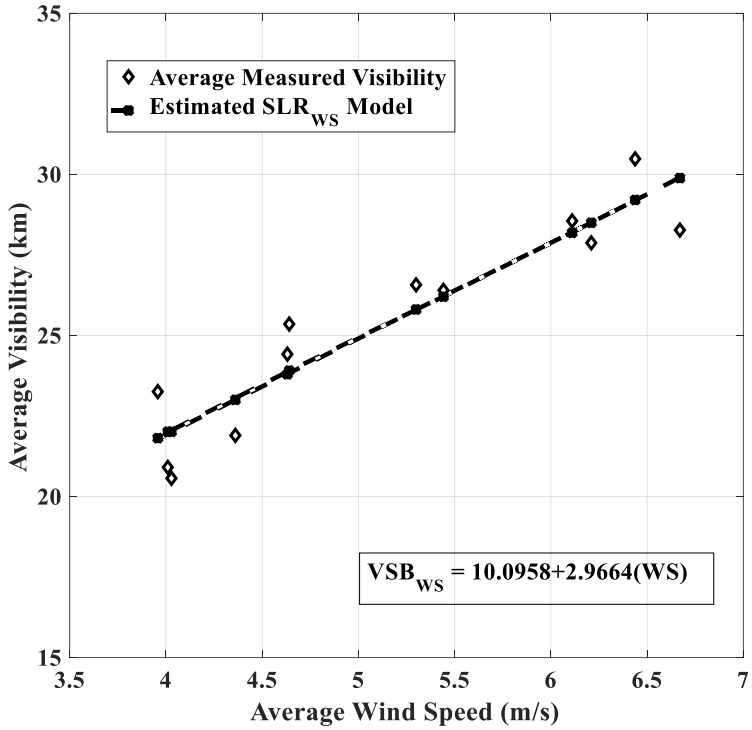

Figure 1.5: Average visibility (km) against average wind speed (m/s).

Various aerosol scattering models based on the Mie scattering theory have established the relationship between aerosol scattering attenuation and atmospheric visibility for IR wavelengths ([15]-[21], [36], [37]). This is because the atmospheric particle radii are approximately equal to the IR wavelengths [13, 14]. Using the appropriate aerosol scattering model in computing the associated specific attenuation encountered by transmitted optical signals is important in calculating the required fade margin for FSOC systems. Some of these aerosol scattering models are suitable only for a small range of optical wavelengths [17], [20], [37]. Others are not suitable for visibility under fog conditions [19], [37]. Therefore, in Chapter 3, the Kim model is employed to compute the specific attenuation for visibility under haze and clear weather conditions, while the Ijaz fog model is used for estimating the attenuation for visibility under foggy weather.

The Kim and Ijaz fog models are also used in the computations of probabilities of exceeding and encountering various aerosol scattering attenuations based on the unique cumulative distribution functions (CDF) of visibility for all the locations of interest. This was achieved for two optical wavelengths, namely, 850 and 1550 nm. The optical link margins for two FSOC links based on the selected wavelengths are shown, while the minimum required visibility CDFs are computed. The resultant link availability plots from

the calculated and approximated CDFs are also presented. Signal to noise ratio, bit error rate, and data rate computations and results for non-return-to-zero on-off keying (NRZ-OOK) FSOC links are analyzed.

In Chapter 4, the analysis of the effects of atmospheric turbulence on FSOC links transmitting at a wavelength of 1550 nm is presented. The choice of selecting this wavelength stems from the findings that at 1550 nm, the eyes are less sensitive to light and, therefore, the eye safety requirement is more relaxed and the interference due to ambient light sources is considerably reduced when compared to optical beams at the 850 nm wavelength [9]. The CDF, probability distribution function (PDF) and percentage of time (POT) analyses of ground wind speed data obtained from the SAWS as well as the application of the Hufnagel-Andrews-Phillips (HAP) model are used in computing the refractive index structure parameters (C_n^2) for various cities in South Africa.

These C_n^2 are then employed in calculating the scintillation indices of the locations of interest for periods not exceeding 50%, 99%, 99.9%, and 99.99% of the time. The scintillation indices as well as the effective number of large-scale and small-scale turbulence eddies are computed based on the zero inner scale and infinite outer scale model and finite inner scale and finite outer scale model for the afore-mentioned time intervals in the locations of interest. Derivations of the CDFs of the Lognormal and Gamma-gamma turbulence distributions while considering the effects of pointing errors are presented. Also, the outage probability and bit error rate analyses, taking into account the effects of pointing errors in weak and moderate to strong turbulence regimes, are carried out for FSOC links employing various IM/DD schemes deployed in the locations of study.

Chapter 5 is the concluding chapter. Concise summaries of the key research contributions and outcomes provided in this thesis, as well as further recommendations for future study, are presented.

Chapter 2

2 Journal Article 1

Visibility Modeling and Prediction for Free Space Optical Communication Systems for South Africa

Olabamidele O. Kolawole, Modisa Mosalaosi, Thomas J.O. Afullo

Published: *International Journal on Communications Antenna and Propagation (IRECAP)*, 2020, vol. 10, no. 3, DOI: 10.15866/irecap.v10i3.18008

2.1 Abstract

Due to the cost and complexity in the measurement of Free Space Optical (FSO) visibility, this paper presents regression models based on meteorological factors to reliably estimate atmospheric visibility. The meteorological factors used are relative humidity, temperature, fractional sunshine, atmospheric pressure and wind speed for Cape Town, South Africa. Initially, Simple Linear Regression (SLR) models are developed and presented. To improve the performance of the regression, the SLR model is extended to a Multiple Linear Regression model (MLR) where three of the meteorological factors are taken into consideration simultaneously. It was found that by implementing MLR, the model performance improves considerably. However, it was also found that the model had effects of multicollinearity due to some of the predictor variables being highly correlated. To mitigate the effects of multicollinearity, two approaches are proposed, 1) removing the problematic terms from the regression model and 2) introducing interaction terms. Both approaches are seen to have little impact on the overall performance of the MLR model while the estimated model coefficients are significant at 5% significant level. In general, it is found through application of standard statistical tests that both SLR and MLR models can be used adequately to determine visibility at a location.

2.2 Introduction

The ever-increasing variety of bandwidth-intensive mobile applications has led to an unprecedented rapid growth of the internet. This kind of growth may especially be attributed to the Internet of Things (IoT) technologies that have revolutionized the extent to which a massive number of devices are connected in a network. Through a unique addressing scheme, these devices are capable of interacting as well as cooperating amongst themselves to accomplish intended tasks [1]. The number of connected devices to the internet is expected to continue to surge upwards over time. Currently, promising solutions to support such growing demand in connectivity is through the fifth generation (5G) wireless communication systems where millimetre wave (MMW) as well as massive multiple-input multiple-output (M-MIMO) antenna technologies are to be integrated. However, due to strict regulations in the usage of the radio frequency (RF) spectrum, the transmission rates for mobile technologies operating in the RF spectrum are limited by the available RF spectrum. Some of the operational standards include Wi-Fi (IEEE 802.11), UWB (IEEE 802.15), WiMAX (IEEE 802.16), iBurst (IEEE 802.20), and the cellular based 3G and 4G [2]. To date, the capability to support numerous service requirements in order to realize elastic and ubiquitous connectivity remains a major challenge [3]. Ideally, a convergent, cost-effective, and pervasive network penetration for the next-generation network (NGN) is required. However, optical wireless communication (OWC) systems may be deployed as an alternative solution to the spectrum limitation. OWC is an attractive broadband access technology that offers high data rates as well as improved capacity. Therefore, OWC can attend to some of the bandwidth requirements of numerous applications and services of the NGNs cost effectively [2], [4].

A terrestrial OWC system, as is with any communication system, consists of the transmitter, the channel, and receiver. The focus of this work will only be on the free space as a channel. The performance of a communication system is highly dependent on the channel condition, and the effective design of the communication system depends on the understanding of that channel. The optical field produced at the transmitter is radiated through the atmospheric channel to the receiving end. Due to the resultant effects of scattering and absorption (wavelength-dependent) introduced by the molecular structure and atmospheric aerosols along the transmission path, transmission loss occurs. In this light, this paper aims to utilize meteorological parameters to estimate meteorological visibility of a radiated optical field. Visibility is a key parameter in determining the attenuation of optical signals. By definition, it is perhaps logical to precede with an intuitive analogy of visibility in terms of eyesight. In this way, it is defined as the meteorological optical range defining how far away objects may be seen under certain conditions (snow, fog, rain etc.). In other words, there is a certain contrast ratio threshold below which an observer cannot discern the difference

between light and dark objects. In the case of free space optical receivers, the threshold contrast ratio is analogous to receiver sensitivity i.e. how long can the optical beam travel before it is "invisible" to the optical receiver. Generally, visibility is measured in airports at visible wavelengths over long periods of time. Even though commercial FSO systems use infra-red (IR) wavelengths, their propagation is quite similar to those of visible wavelength with an added advantage that they have improved penetration. The significance of this assertion lies in the fact that available visibility data are measured at visible wavelengths, therefore predictions made off of this data cannot in anyway undermine the effects of atmospheric conditions on optical propagation.

Atmospheric visibility studies are common in the environmental sciences fraternity (global warming, climatology etc.), with its greater application in the aviation industry and to some extent in generating automated warnings for motorists during adverse weather conditions [5]. It has been found in several research work [6]-[7] that visibility has a strong relationship with numerous meteorological factors such as temperature, relative humidity and fractional sunshine. These relationships are typically obtained through simple linear regression analysis. In [8], however, they have extended the simple regression models to incorporate several parameters in one regression analysis to obtain a multiple regression model. Throughout these works, the focus of [8]-[13] were on the performance of the models which in turn informed their choice of best or acceptable models.

This was done through standard statistical tests such as the coefficient of determination, R^2, root mean square error, RMSE, mean bias error, MBE and mean percentage error, MPE. In this paper, a thorough regression analysis is presented suitable for free space optical communications. In our view, prior research work available in literature is not suitable for optical communication system design as it lacks statistical value.

Firstly, as mentioned before, the focus of the modeling technique in previous works is on the accuracy of the model instead of its statistical power. The risk of such an approach lies in the fact that a model can perform well for a given sample of a population, but may not do so if a different sample is selected. In this work, this deficit is addressed by testing the significance of model parameter coefficients before a conclusion is made about its suitability. Secondly, in the multiple regression model, there is a strong evidence of multicollinearity observable from the results of [8]-[13]. In the presence of multicollinearity, the statistical power of the model is lost making it difficult to specify the correct model. In this work, multicollinearity is investigated and mitigated for it to improve the usefulness of the model. The performance of each model is then assessed and some conclusions drawn.

The rest of the paper is organized as follows: Section 2.3 presents the methodological approach used in model validation and acknowledges the data source. The regression analysis and modeling is introduced in Section 2.4 with simple linear regression and its extension to multiple linear regression discussed in Section 2.5. Visibility is estimated in Section 2.6 using MLR and its performance is compared to those of SLR. The evident effects of multicollinearity are assessed in Section 2.7 and quantified through the variance inflation factor which are then mitigated for in Section 2.8. The general findings are presented in Section 2.9 through the discussion of results while Section 2.10 provides the conclusion.

2.3 Data and Methodology

This research work is a case study of a warm-summer Mediterranean climatic region of Cape Town, South Africa. Its climatic profile is characterized by warm and dry summers with mean monthly temperatures not exceeding 22 ^{o}C during the warmest month. During the coldest month, average temperatures range between -3 ^{o}C and 18 ^{o}C with mild to chilly rainy weather experienced in winter, sometimes accompanied by snowfall. Similar climatic conditions are prevalent in Spain, Portugal, western Washington, central Chile, southern Australia etc. Mediterranean climatic regions experience between 2650 to 3400 hours of sunshine annually with a yearly average solar radiation of up to 3200 kWh/m^2 [14]-[17].

The average monthly visibility for an eight year period starting from January 2010 to December 2017 for Cape Town were provided by the South African Weather Services (SAWS). The same source provided data for other meteorological parameters used in this work i.e. relative humidity, temperature, sunshine hours, atmospheric pressure and wind speed spanning the same time period as well. The measured data is populated as monthly averages over the measurement period and used in the modeling process. The relationship between visibility and the aforementioned meteorological parameters is described using linear regression models.

The statistical significance of the regression model coefficients is tested by means of the t-test for zero-slope coefficients. All correlation coefficients were appropriately tested by computing the coefficient of determination, R^2. Moreover, the extent to which multicollinearity is present was tested through variance inflation factors (VIF). As a rule of thumb, a VIF more than 5 is considered a strong indication of multicollinearity and a reason for concern. To show the significance/uncertainty of the regression coefficients, a 5% significance level was used as a benchmark against the *p*-values of the estimated model coefficients.

2.4 Simple Linear Regression (SLR) Model

Simple linear regression is a statistical technique through which a relationship between two quantitative variables can be studied and summarized. In its structure, one variable is the outcome (dependent) while the other is the independent (predictor) variable. The adjective "simple" is derived from the fact that the model is only concerned with a single independent variable (IV). The extension of this treatment to two or more IVs is referred to as multiple linear regression, which will be discussed later in the paper. In a simple linear regression model (SLR), the relationship between an output variable *y* and an independent variable *x* can be illustrated based on the regression equation of the form

$$y_i = \beta_0 + \beta_1 x_i + \in_i \qquad i = 1, 2, 3, ..., n \tag{2.1}$$

where β_0 is the intercept and β_1 is the slope parameter. By applying the least squares technique, the line of best fit can be determined by minimizing the sum of the squares of the difference between the observed data points and the corresponding fitted data values provided by the model. In general, the actual observation y_i is predicted by the best fit line as follows:

$$\hat{y}_i = b_0 + b_1 x_i \tag{2.2}$$

where b_0 and b_1 are the estimates of β_0 and β_1, respectively. Before application of the SLR model to a dataset, it is necessary to evaluate its appropriateness.

The suitability of the model relies on considering several underlying assumptions about the population prediction errors as being reasonable. Under these assumptions, all subsequent tests, confidence intervals, and hypothesis tests that arise in the regression analysis assume that the model is appropriate. Without a proper validity of the model correctness, all the formulas and methodologies used going forward are of little use in the prediction process and model consistency. The application of SLR models assumes the following:

- The mean of the response variable, $E(y_i)$, for each value of the IV, x_i, is a linear function of x_i;
- The errors, $\in_i$, are independent;
- The errors, $\in_i$, for each value of the IV, x_i, are normally distributed;
- The errors, $\in_i$, for each value of the IV, x_i, have equal variances.

The conditions stated above may collectively be summarized to describe the errors as independent, normal random variables with zero mean, $E(\in_i) = 0$ and constant variance, σ^2. The unknown actual error terms, $\in_i = y_i - E(y_i)$ may be estimated through the residual terms, $e_i = y_i - \hat{y}_i$, which is simply the difference between the observed data point y_i and the corresponding estimated value $\hat{y}_i$. In this work, meteorological

data measured in Cape Town is used to estimate visibility in FSO communication systems that may be deployed at the location. The atmospheric parameters available for this study are temperature, relative humidity, atmospheric pressure, wind speed and fraction of sunshine hours. The latter simply describes the ratio between the actual amount of sunshine hours in a day (n) and the maximum possible amount of daylight hours (N). By regressing the measured visibility on these five parameters, linear relationships are developed with varied degrees of linearity and significance of coefficients, β_0 and β_1. The fitted models for each IV are obtained as follows:

$$VSB_{RH} = 76.3846 - 0.7178 \times (RH) \tag{2.3}$$

$$VSB_{Temp} = 11.7201 + 0.7965 \times (Temp) \tag{2.4}$$

$$VSB_{FSH} = 0.3530 + 35.8031 \times (FSH) \tag{2.5}$$

$$VSB_{AP} = 878.7786 - 0.8435 \times (AP) \tag{2.6}$$

$$VSB_{WS} = 10.0958 + 2.9664 \times (WS) \tag{2.7}$$

where RH is the relative humidity in %, $Temp$ is the temperature in °C, FSH is the fractional sunshine hours (n/N), AP is the atmospheric pressure in mb and WS is the wind speed in m/s. VSB_{RH}, VSB_{Temp}, VSB_{FSH}, VSB_{AP}, and VSB_{WS} are estimated visibilities in km from each of the SLR models with IVs: RH, $Temp$, FSH, AP and WS respectively. In order to assess the normality of the actual error terms, the residuals $\left(y_i - \hat{y}_i\right)$ are obtained and their probability plotted. The idea is to visually assess whether the residuals come from a population with a normal distribution. If the residuals have a normal distribution, then it is expected that they will appear along a reference line with little to no indication of curvatures in the plot.

The probability of residuals obtained from all the five models are plotted in Figure 2.1. In all the five cases, there is visually no indication for concern in terms of normality as the residuals satisfactorily hugs the reference line. The other condition required for the application of SLR models is that the error terms have a uniform variance, σ^2. By plotting the error bars alongside the predicted model, the error variance can be observed along the best fit line as shown in Figure 2.2. It is observed, in all five models, that there are data points whose error variance differs significantly from others (at most three data points), e.g. $\in_3$, $\in_5$ of the Temp-based model. However, this is not enough to suggest that the error variance in general is not uniform

since most of the data points exhibit relatively constant error variance. The performance of each model is shown in Tables 2.1 through 2.5 in terms of the root mean square error (RMSE), correlation coefficient (*R*) and *p*-value. The *p*-value gives indication on the hypothesis that the model is significant or otherwise at a specific % confidence level. Perhaps more important than the accuracy of the model is the significance of the model parameters used in the prediction process.

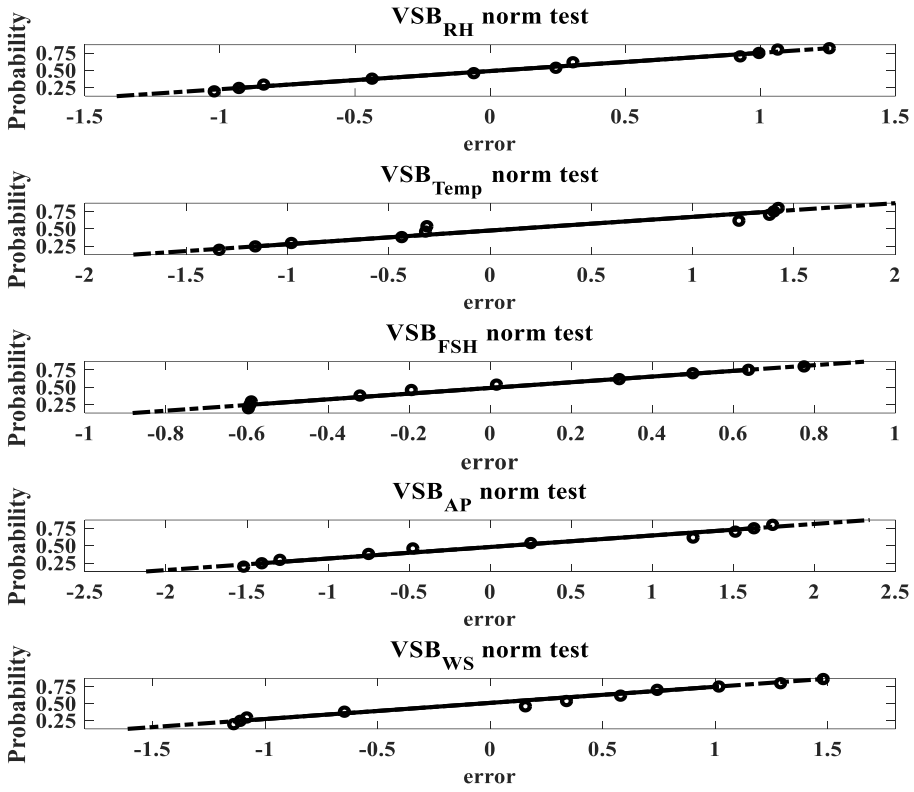

Figure 2.1: Normality test for all the IVs

In general, for linear regression models, it is often useful to determine the *t*-statistic in order to make sound inferences with regards to the regression coefficients. A hypothesis test is performed on each coefficient *j* for the null hypothesis that it is equal to zero i.e. the corresponding model term is insignificant - against the alternative that it is different from zero. By definition, a hypothesis test on coefficient *j*, with $H_0 : \beta_j = 0$ and $H_1 : \beta_j \neq 0$, the t -statistic is given by,

$$tStat = \frac{b_j}{SE\left(b_j\right)} \tag{2.8}$$

where $SE\left(b_j\right)$ is the standard error of the estimated coefficient b_j.

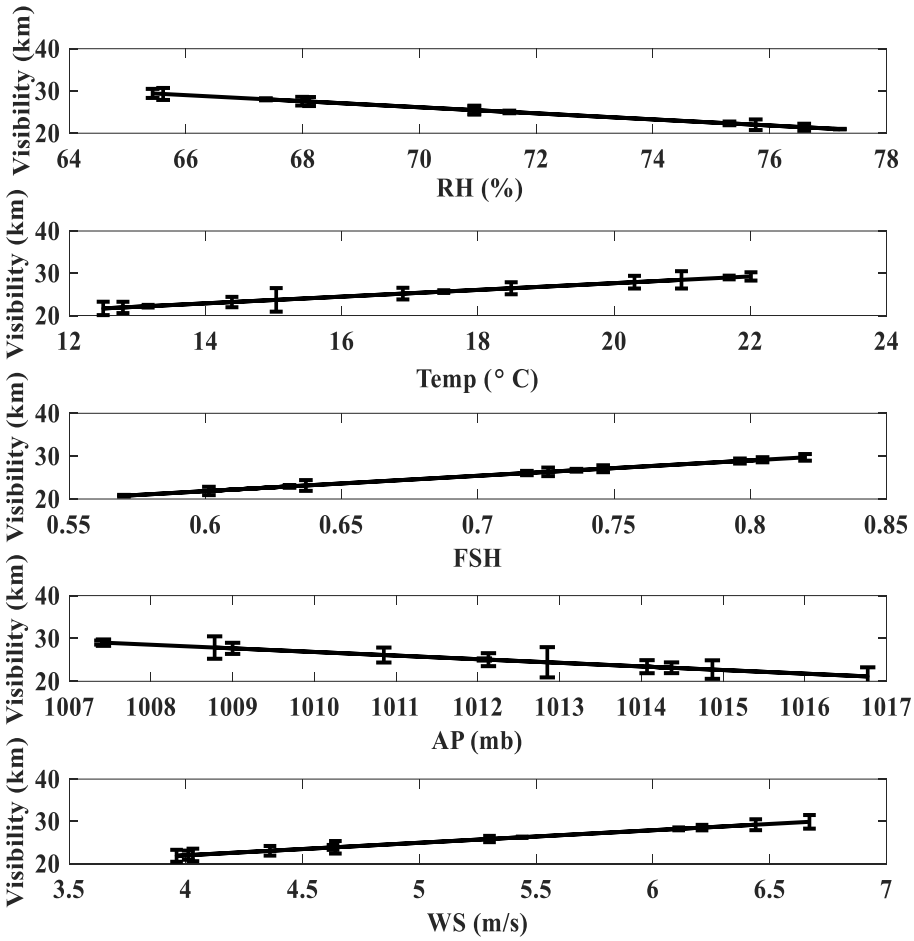

Figure 2.2: Error bars for variance test for all the IVs.

It can be seen from Tables 2.1 - 2.5 that *tStat* = Estimate/SE for all estimated coefficients. Since each model consists of two terms, the independent variable and the constant, the t-statistic tests for the significance of each term in the presence of the other. Considering the model derived from FSH, the intercept term is not significant at 5% significant level as indicated by its *p*-value of 0.8542 which is greater than 0.05. However, both terms of the models derived from *RH, Temp, AP* and *WS* are significant at 5% significant level. In terms of model performance, the *FSH*-based model easily outperforms the other four having the highest correlation coefficient, lowest RMSE, and smallest *p*-value as shown in Tables 2.1 through 2.5. The *RH*-based model follows secondly, outperforming the *Temp*-, *AP*- and *WS*-based models across all the three metrics. Before making a decision on the best model in the prediction of visibility, the issue of an insignificant predictor under the *FSH*-based model is re-visited. In view of the fact that the intercept term is not a predictor variable, there is no specific hypothesis regarding its usefulness so it might be best to exclude it in order to simplify the model.

Table 2.1: SLR_{RH} estimated coefficients

	Estimate	SE	*tStat*	*p*-value
Intercept	76.3846	4.9871	15.3165	2.8601×10^{-8}
RH	-0.7178	0.0701	-10.2451	1.2726×10^{-6}
Model	RMSE = 0.995	R = 0.9555	*p*-value = 1.3×10^{-6}	

Table 2.2: SLR_{TEMP} estimated coefficients

	Estimate	SE	*tStat*	*p*-value
Intercept	11.7201	2.3550	4.9767	0.0006
Temp	0.7965	0.1347	5.9124	0.0001
Model	RMSE = 1.5913	R = 0.8818	*p*-value = 1.5×10^{-4}	

Table 2.3: SLR_{FSH} estimated coefficients

	Estimate	SE	*tStat*	*p*-value
Intercept	0.353	1.8715	0.1886	0.8542
FSH	35.8031	2.6587	13.4665	9.8104×10^{-8}
Model	RMSE = 0.771	R = 0.9735	*p*-value = 9.8×10^{-8}	

Table 2.4: SLR_{AP} estimated coefficients

	Estimate	SE	*tStat*	*p*-value
Intercept	878.7786	199.6018	4.4027	0.0013
AP	-0.8435	0.1973	-4.2755	0.0016
Model	RMSE = 2.006	R = 0.8040	*p*-value = 1.6×10^{-3}	

Table 2.5: SLR_{WS} estimated coefficients

	Estimate	SE	*tStat*	*p*-value
Intercept	10.0958	1.8815	5.3658	3.1642×10^{-4}
WS	2.9664	0.359	8.264	8.8506×10^{-6}
Model	RMSE = 1.206	R = 0.9340	*p*-value = 1.6×10^{-3}	

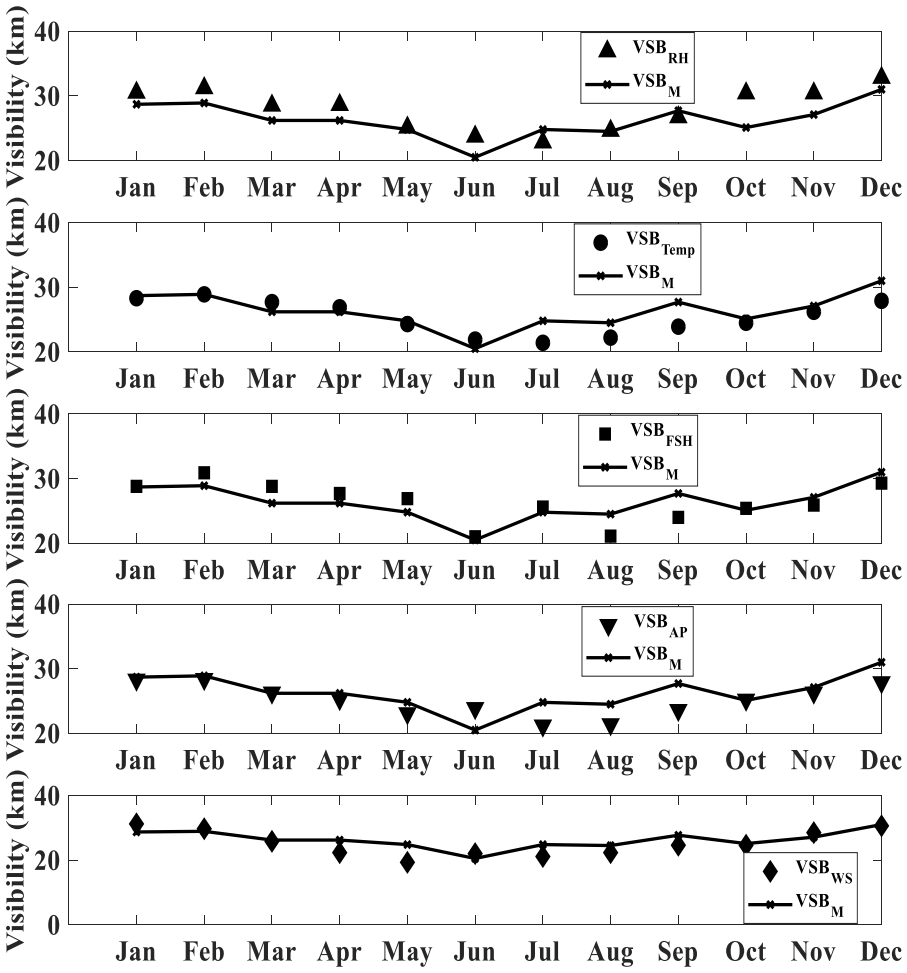

Figure 2.3: Measured and estimated visibility for all IVs from January-December, 2017.

One further advantage of leaving out an insignificant term is that an extra degree of freedom is gained, which is valuable considering the small number of samples (Ns = 12). The *FSH*-based model will now be reduced to simply $y_i = \beta_1 x_i + \in_i$. After regressing visibility on FSH with $\beta_0 = 0$, it turns out that there is little change in the model performance in terms of the correlation coefficient, R = 0.9741 compared to the previous R = 0.9735. More impressively, the significance of the *FSH* coefficient has improved a great deal as indicated by a t -statistic value of 120.02 compared to the previous 13.47. This is a culmination of reduced standard error in the estimation of the *FSH* coefficient, previously at SE = 2.66 and currently at SE = 0.30. This indicates an almost ten-fold reduction in the standard error in estimating β_1. Thus, in the adjusted model, the expected variance in the β_1 coefficient has significantly been reduced and this improves the model consistency.

2.5 Multiple Linear Regression (MLR) Model

The goal of any regression technique is to model the relationship between the independent (explanatory/regressors) and the dependent (response) variables. Multiple linear regression (MLR) is one such approach that uses several independent variables to predict the outcome of a dependent variable. This, in contrast with a simple linear regression technique in which only two continuous variables are available - an independent variable and a dependent variable, employs rather multiple continuous independent variables to predict a single outcome. In its structure and formulation, it is similar to a simple linear regression except that the linear fit is a plane that cuts through several planes. A multiple regression model is obtained by extending this interpretation to a scenario wherein multiple regressors exist. In such an environment, the dependent variable is related to two or more independent variables. In general, for *m* variables it takes the form:

$$y_i = \beta_0 + \beta_1 x_{i1} + \beta_2 x_{i2} + \cdots + \beta_m x_{im} + \in_i \quad i = 1, 2, \ldots, n \tag{2.9}$$

where β_0 is the intercept. β_j $\left[j = 1, 2, \ldots, m \right]$ are the regression coefficients that measures the unit change in the dependent variable in response to a change in the independent variables. Here $\in_i$ represents the random error term and it is assumed to be normally distributed with mean 0 and constant variance σ^2 i.e. $\in_i \sim \mathbf{N}\left(0, \sigma^2\right)$. The expression in (2.9) may be presented in a more compact form by using the matrix framework. It is straightforward that (2.9) can be re-written in the vectorized form:

$$Y = X\beta + \in \tag{2.10}$$

which can be written in the matrix form:

$$\begin{bmatrix} y_1 \\ y_2 \\ \vdots \\ y_n \end{bmatrix} = \begin{bmatrix} 1 & x_{11} & \cdots & x_{1m} \\ 1 & x_{21} & \cdots & x_{2m} \\ \vdots & \vdots & \ddots & \vdots \\ 1 & x_{n1} & \cdots & x_{nm} \end{bmatrix} \begin{bmatrix} \beta_0 \\ \beta_1 \\ \vdots \\ \beta_m \end{bmatrix} + \begin{bmatrix} \in_1 \\ \in_2 \\ \vdots \\ \in_n \end{bmatrix}$$

where Y is an $n \times 1$ dimensional random vector containing observations, X is an $n \times (m \times 1)$ matrix determined by the regressors, β is an $(m+1) \times 1$ vector of parameters to be determined, and $\in$ is an $n \times 1$ vector of random errors. When performing MLR analysis, the regression coefficients of (2.9) are estimated using the least squares method. These coefficients provide information about the unrelated contributions pertaining to each regressor variable towards predicting the outcome variable. Contrary to simple linear regression, the degree of correlation between pairs of regressor variables must be inferred.

2.6 Estimation of Visibility Using MLR

It has been shown in previous research contributions [6]-[8], as it shall also be done here, that visibility can be estimated from several meteorological factors. Factors such as relative humidity (RH), temperature $(Temp)$, fractional sunshine hours (FSH), atmospheric pressure (AP) and wind speed (WS) have been shown to have a strong relationship with visibility and have thus been utilized in its prediction. In this work, data spanning a period of eight years is used to facilitate the prediction process. In the development of the MLR model, reference will be made to the simple linear regression models based on each of the aforementioned five IVs for comparison and completeness. Similar to SLR, in its application, MLR takes the following assumptions:

- The mean of the response variable, $E(Y_i)$, for each regressor value set $(x_{i1}, x_{i2}, \ldots, x_{im})$ is a linear function of the regressors.
- The errors, $\in_i$, are independent.
- The errors, $\in_i$, for each regressor value set $(x_{i1}, x_{i2}, \ldots, x_{im})$, are normally distributed.
- The errors, $\in_i$, for each regressor value set $(x_{i1}, x_{i2}, \ldots, x_{im})$, have equal variances.

In summary, these assumptions may be understood to describe a process whose error terms are independent, normally distributed, random with zero mean and constant variance. Verifying the validity of the assumptions for a multiple regression model in a comprehensive manner is not a trivial task, however, the thoroughness with which this is done speaks to the confidence that can be placed on the model. As observed in Section 2.4, the errors generated by regressing visibility on RH, $Temp$, FSH, AP and WS are fairly random, independent and normally distributed. In extension to this view, the errors generated by applying MLR is expected to be random, independent and normally distributed as well. The MLR model for estimating visibility is determined to be:

$$VSB_{ALL} = 35.6326 - 0.3540(RH) + 23.6978(FSH) - 0.3219(WS) \tag{2.11}$$

The performance of the MLR model in (2.11) is summarized in Table 2.6. Clearly this model outperforms the SLR models presented in Section 2.4 in terms of the correlation coefficient, R = 0.9915, and RMSE = 0.4915. However, further analysis of the model reveals that the *WS* predictor term of the model is not significant at 5% significant level. The *p*-value for the *WS* term is 0.5233. In summary, the MLR model has significantly improved the model accuracy but has also drastically increased the standard error in the prediction of the model coefficients. The increased variance in the estimation of model coefficients makes it difficult to comprehend the effects of individual predictors towards observed changes in visibility. Ultimately, there is a limited research conclusion that can be drawn from the model.

Table 2.6: MLR estimated coefficients

	Estimate	SE	*tStat*	*p*-value
Intercept	35.6326	9.3473	3.8121	0.0051
RH	-0.3540	0.0972	-3.6422	0.0066
FSH	23.6978	4.6715	5.0728	0.0010
WS	-0.3219	0.4823	-0.6673	0.5233
Model	RMSE = 0.4915	R = 0.9915	*p*-value =	2.0294×10^{-7}

With a quick glance at equations (2.3) - (2.7) in conjunction with (2.11), it can be seen that there is an increased variance in the coefficient estimates i.e. minor changes in the model can result in highly sensitive estimates. Two observations are notable: 1) The significance of wind speed in the prediction of visibility has diminished greatly in MLR compared to SLR. 2) There is a direct proportional relationship between wind speed and visibility when using SLR, while the relationship is inversely proportional when using MLR (the sign has been reversed). This is an indication that the expected value of visibility for a change in each predictor is not a linear function of the changes in the predictors. Simply put, in the MLR model, the change in visibility cannot be attributed to a change in a single predictor whilst holding others constant. Thus, the linearity assumption is violated. Theoretically, it is reasonable to assume that the issues raised above may partly be due to the fact that the IVs are related to one another in some way. It is expected that the meteorological factors be related to each other at a given location, giving rise to the phenomenon of multicollinearity.

2.7 Multicollinearity of Visibility Predictors

Multicollinearity is a phenomenon that arises due to having two or more predictors in a regression model with a moderate or high degree of correlation. Its presence reduces the precision of the estimate of coefficients, which weakens the statistical power of the regression model. In the presence of multicollinearity, the significance of some predictors may be diminished making it difficult to determine the role of each predictor. Assuming that multicollinearity exists, the critical question is: to what extent are the IVs correlated? Conceptually, the idea is to figure out if any of the predictors measure the same or similar construct. The dependence between multiple variables can be evaluated by computing a correlation matrix. In this work, the correlation analysis has been performed using Pearson's parametric correlation test. In its application, the correlation coefficient, R, between two random variables $\mathbf{X}$ and $\mathbf{Y}$ with n series of measurements sampled such that they are presented in the form x_i and y_i for $i = 1,2,3,\ldots,n$, then the

sample correlation coefficient may be used to estimate the population correlation between **X** and **Y**. The sample correlation coefficient is calculated as:

$$R = \frac{\sum_{i=1}^{n}(x_i - \bar{x})(y_i - \bar{y})}{\sqrt{\sum_{i=1}^{n}(x_i - \bar{x})^2 (y_i - \bar{y})^2}} \tag{2.12}$$

where $\bar{x}$ and $\bar{y}$ are the sample means of **X** and **Y**, respectively. For a given system of study with *n* random variables $M_1, \ldots, M_n$, its correlation matrix is an $n \times n$ matrix whose i, j entry represents $corr(M_i, M_j)$. It is common practice to create a graphical display of the correlation matrix, this can be done using the statistical toolbox in MATLAB. The plot shows correlations among pairs of variables in *M*. The scatter plots of variable pairs appear in the off diagonal while the histograms of the variables appear along the diagonal. The least squares method is used to determine the best fit line between variables with correlation coefficients also displayed on each graph pair as shown in Figure 2.4. The correlation coefficients, *R* (extracted into the *R*-matrix below), indicate which pairs of variables have correlations significantly different from zero. The significance of the correlations are determined by calculating the *p*-values for each variable pair and displayed as *p*-matrix below:

$$R = \begin{bmatrix} & VSB & RH & Temp & FSH & AP & WS \\ VSB & 1.0000 & -09554 & 0.8819 & 0.9735 & -0.8041 & 0.9339 \\ RH & -0.9554 & 1.0000 & -0.8060 & -0.8976 & 0.7397 & -0.9297 \\ Temp & 0.8819 & -0.8060 & 1.0000 & 0.9480 & -0.9804 & 0.9144 \\ FSH & 0.9735 & -0.8976 & 0.9480 & 1.0000 & -0.8842 & 0.9264 \\ AP & -0.8041 & 0.7397 & -0.9804 & -0.8842 & 1.0000 & -0.8900 \\ WS & 0.9339 & -0.9297 & 0.9144 & 0.9264 & -0.8900 & 1.0000 \end{bmatrix}$$

$$p = \begin{bmatrix} & VSB & RH & Temp & FSH & AP & WS \\ VSB & 1.0000 & 0.0000 & 0.0001 & 0.0000 & 0.0016 & 0.0000 \\ RH & 0.0000 & 1.0000 & 0.0015 & 0.0001 & 0.0060 & 0.0000 \\ Temp & 0.0001 & 0.0015 & 1.0000 & 0.0000 & 0.0000 & 0.0000 \\ FSH & 0.0000 & 0.0001 & 0.0000 & 1.0000 & 0.0001 & 0.0000 \\ AP & 0.0016 & 0.0060 & 0.0000 & 0.0001 & 1.0000 & 0.0001 \\ WS & 0.0000 & 0.0000 & 0.0000 & 0.0000 & 0.0001 & 1.0000 \end{bmatrix}$$

Evidently, the output pairwise *p*-values are all less than 5% significant level, indicating that all pairs of variables have correlations significantly greater than zero. That is, there is a fairly strong linear relationship between the predictor variables. For example, *AP* and *Temp* are strongly correlated (*R* = -0.9804), while *RH* and *AP* are moderately correlated (*R* = 0.7397).

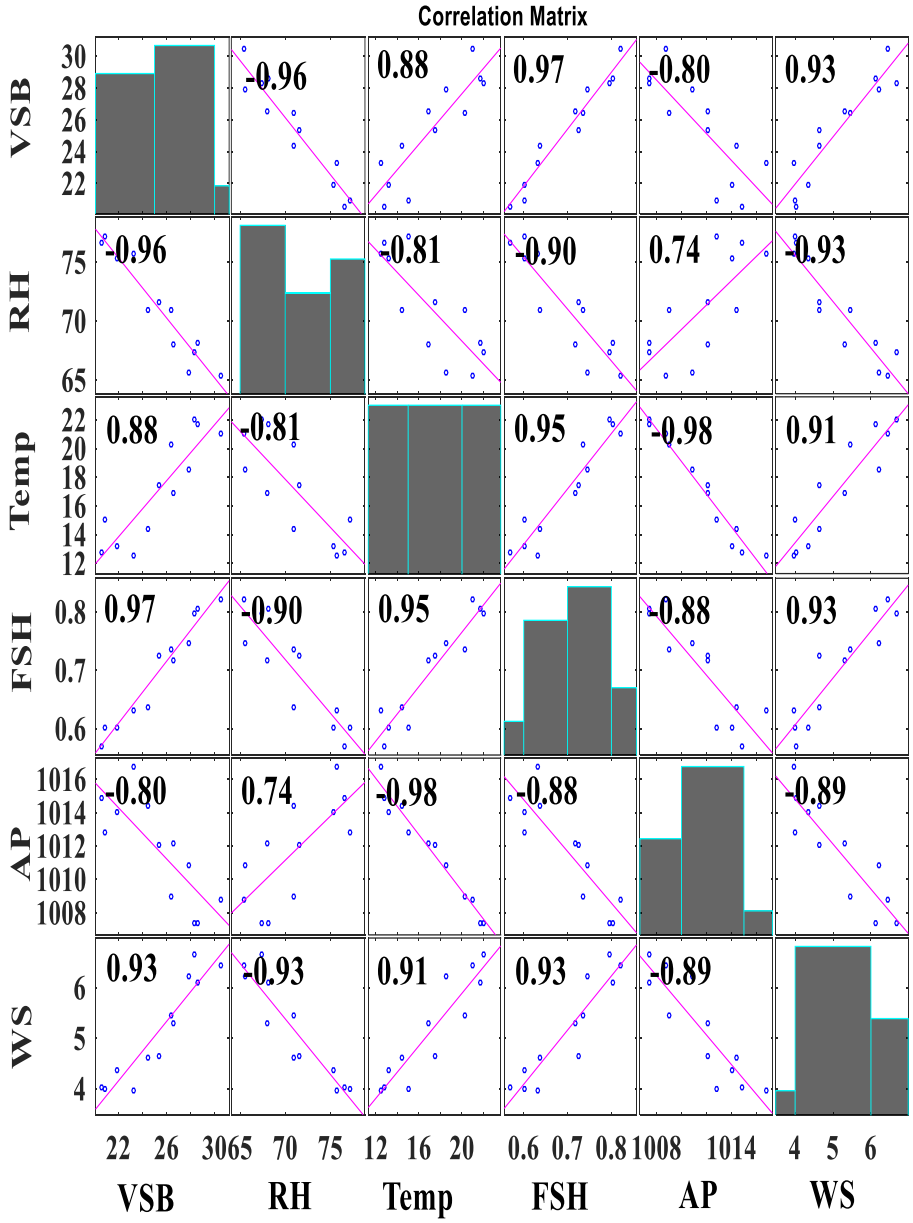

Figure 2.4: Correlation Matrix for Visibility and all the IVs.

It may not be adequate to assess the severity of multicollinearity in a regression analysis by analysing the correlation coefficients, usually, a variance inflation factor (VIF) is used. This factor is the ratio between the variance of a predictor in a model with multiple predictors and the variance of the predictor in a model with a single term [18]. It basically quantifies the extent to which the variance is inflated, as the name suggests. Considering a model in which x_m is the only outcome predictor (as in the SLR case in (2.1)), it can be shown that the variance of the estimated coefficient b_m is given by:

$$\sigma^2(b_m) = \frac{\sigma^2}{\sum_{i=1}^{n}\left(x_{im} - \bar{x}\right)^2} \tag{2.13}$$

In a multiple linear regression model where multicollinearity is present, such as in (2.9), the variance of b_m is inflated. The inflated variance can be calculated as:

$$\sigma^2(b_m) = \frac{\sigma^2}{\sum_{i=1}^{n}\left(x_{im} - \bar{x}\right)^2} \times \frac{1}{1 - R_m^2} \tag{2.14}$$

where R_m^2 is the coefficient of determination (R^2) obtained by regressing the m^{th} predictor on the remaining predictors. According to (2.14), the higher the correlation between predictor x_{im} and the other predictors, R_m^2, the greater the variance of b_m. By taking the ratio of the two variances, the proportion of inflation can be determined. Thus, VIF is found as follows:

$$\sigma^2(b_m) = \frac{\frac{\sigma^2}{\sum_{i=1}^{n}\left(x_{im} - \bar{x}\right)^2} \times \frac{1}{1 - R_m^2}}{\frac{\sigma^2}{\sum_{i=1}^{n}\left(x_{im} - \bar{x}\right)^2}} = \frac{1}{1 - R_m^2} \tag{2.15}$$

For all the m predictors available in the MLR model there exist a corresponding variance inflation factor. The objective is to determine the extent of "inflation" on the variance of the estimated regression coefficient b_m as a result of correlation among predictor variables. It is straightforward from (2.15) that a VIF of 1 indicates no correlation between the m^{th} predictor and the rest of the predictor variables, thus, the variance of b_m is not inflated at all. There is no general agreement on the interpretation of VIF, but the general rule of thumb is that a VIF exceeding 5 warrants further investigation [19] while those in excess of 10 signifies serious multicollinearity [20]. These requires correction for meaningful model interpretation. By regressing *WS*, *FSH* and *RH* on the remaining two variables at a time, the VIF for each predictor variable can be calculated using (2.15). The results are shown in Table 2.7.

The coefficient of determination for *WS*, *RH* and *FSH* are, $R_{WS}^2 = 0.908$, $R_{RH}^2 = 0.873$ and $R_{FSH}^2 = 0.869$ respectively. As shown in Table 2.7, their corresponding VIFs are 10.87, 7.89 and 7.60 respectively. The VIFs for *WS*, *RH* and *FSH* are fairly large. By interpretation, for example, the VIF for *WS* indicates that the variance of the estimated coefficient b_{WS} of predictor *WS* is inflated by a factor of 10.87. It follows then that the estimated coefficients of *RH* (b_{RH}) and *FSH* (b_{FSH}) are inflated by factors of 7.89 and 7.60, respectively.

Table 2.7: Determination of variance inflation factors

		***WS* as output**		
	Estimate	SE	*tStat*	*p*-value
Intercept	9.75147	5.58268	1.74674	0.11463
RH	-0.11889	0.05425	-2.19149	0.05611
FSH	5.50649	2.65601	2.07321	0.06801
Model	RMSE = 0.3397	R^2 = 0.908	VIF = 10.8696	
		***RH* as output**		
	Estimate	SE	*tStat*	*p*-value
Intercept	94.90659	5.15379	18.41492	1.87844×10^{-8}
FSH	-12.53896	15.46406	-0.81085	0.43837
WS	-2.92676	1.33551	-2.19149	0.05611
Model	RMSE = 1.6853	R^2 = 0.873	VIF = 7.8927	
		***FSH* as output**		
	Estimate	SE	*tStat*	*p*-value
Intercept	0.78240	0.61387	1.27453	0.23440
RH	-0.00543	0.00670	-0.81085	0.43837
WS	0.05870	0.02831	2.07321	0.06801
Model	RMSE = 0.0351	R^2 = 0.869	VIF = 7.6046	

2.8 Mitigation for Multicollinearity

It has been shown in the analysis of the MLR model of (2.11) that the model exhibits signs of multicollinearity. Furthermore, it has been ascertained through the evaluation of variance inflation factors that indeed the model has cases of multicollinearity among some of the predictor terms. The objective of modeling visibility with meteorological factors is to obtain a model which is easy to interpret with stable coefficients and statistical significance. The presence of multicollinearity makes it difficult to specify the correct model. In the following sub-sections two approaches are proposed to deal with the effects of multicollinearity.

2.8.1 Removing highly correlated predictors

Based on the results obtained in Section 2.7 and equation (2.15), it is straight forward that the value of VIF can be reduced by removing one of the highly correlated predictor pairs from the model. Using the guidelines provided in Section 2.7 and the results in Table 2.7, the severe multicollinearity effects involving

WS (VIF = 10.87) need to be addressed (since it is above 10). By observing the correlation matrix plot in Figure 2.4, further light is shed on which predictor pairs are highly correlated. It turns out that the three predictor variables which exhibit severe multicollinearity (*WS*, *RH* and *FSH*) in the MLR model, are in fact highly correlated among themselves. The correlation coefficient (*R*) between the sets of *WS* & *RH*, *WS* & *FSH* and *RH* & *FSH* are -0.93, 0.93 and -0.90 respectively. As revealed in Table 2.6, the *WS* predictor term of the model is not significant at 5% significant level as the *p*-value for the *WS* term is 0.5233. Therefore, removing the *WS* term from the model since it is insignificant and regressing visibility on *FSH* and *RH*, the model reduces to:

$$VSB_{RH\&FSH} = 32.4940 - 0.3158(RH) + 21.9255(FSH) \tag{2.16}$$

The performance of model (2.16) is shown in Table 2.8. It is evident from Table 2.8 that all the estimated coefficients for predictor variables included in the models are now significant at 5% significant level. The VIF criteria is used again to assess effects of multicollinearity. It should be noted that for a model with only two predictor terms, the VIFs for the two predictors will be the same i.e. the same R^2 value is obtained after regressing one term on the other. In this case, $VIF_{RH} = VIF_{FSH} = 5.1467$.

Table 2.8: Modeling without highly correlated predictors

	Estimate	SE	*tStat*	*p*-value
Intercept	32.4940	7.8250	4.1526	0.0025
RH	-0.3158	0.07604	-4.1530	0.0025
FSH	21.9255	3.7228	5.8895	0.0002
Model	RMSE = 0.4761	$R^2 = 0.9821$	*p*-value = 1.3804×10^{-8}	

It can be concluded that the effects of multicollinearity has been addressed adequately. Simply put, there is hardly any variance inflation present. Incidentally, the model accuracy does not seem to have been lost in terms of the R^2 value. In fact, the performance observed in Table 2.8 is slightly better than that of (2.11) as shown in Tables 2.6 and 2.8, respectively. The model in (2.16) has a slightly smaller RMSE (0.4761 vs 0.4915) as well as the *p*-value (by an order of 10), while the $R^2 = 0.98$ remains approximately equal.

2.8.2 Introducing interaction terms

A linear combination of predictors is known to alleviate effects of multicollinearity. Even though *RH*, *WS* and *FSH* are not measured in the same way i.e. *RH* is measured as a percentage, *WS* in derived units while *FSH* is a ratio. As shown in Subsection 2.8.1, excluding highly correlated predictors may alleviate effects of multicollinearity. However, it is also possible that such correlated predictors may have a complementary

effect in determining the output variable. In this way, the two variables are combined into one variable. In this work, the meaningful interactions between *RH*, *WS* and *FSH* have been found to be *RH+WS*, *RH-WS*, and *FSH×WS*. The representative formulations are shown in (2.17) and (2.18) below.

$$y_i = \beta_0 + \beta_1(x_{i1} \pm x_{i2}) + \beta_2 x_{i3} + \in_i \tag{2.17}$$

and

$$y_i = \beta_0 + \beta_1(x_{i1} \times x_{i2}) + \beta_2 x_{i3} + \in_i \tag{2.18}$$

In (2.17), x_{i1} and x_{i2} are the i^{th} elements of *RH* and *WS* while x_{i3} represent the i^{th} elements of *FSH*. On the other hand, x_{i1} and x_{i2} are the i^{th} elements of *FSH* and *WS* while x_{i3} represent the i^{th} elements of *RH* in (2.18). The results of these regressions are shown in Table 2.9. It can be observed that all the model term coefficients are significant at 5% significant level.

Table 2.9: Modeling with interaction terms introduced

(*RH+WS*)				
	Estimate	SE	*tStat*	*p*-value
Intercept	35.8690	8.2920	4.3257	0.0019
RH+WS	-0.3572	0.0826	-4.3231	0.0019
FSH	23.9390	3.1756	7.5385	3.5468×10^{-5}
Model	RMSE = 0.4635	$R^2 = 0.9830$	*p*-value = 1.0852×10^{-8}	
(*RH-WS*)				
	Estimate	SE	*tStat*	*p*-value
Intercept	28.4385	7.5419	3.7707	0.0044
RH-WS	-0.2697	0.0715	-3.7742	0.0044
FSH	21.0557	4.2788	4.9209	0.0008
Model	RMSE = 0.5059	$R^2 = 0.9798$	*p*-value = 2.3847×10^{-8}	
(*WS*FSH*)				
	Estimate	SE	*tStat*	*p*-value
Intercept	45.3112	11.7845	3.8450	0.0039
*FSH*WS*	1.4625	0.5242	2.7898	0.0211
RH	-0.3561	0.1404	-2.5359	0.0319
Model	RMSE = 0.7681	$R^2 = 0.9534$	*p*-value = 1.0224×10^{-6}	

Even though the model derived from the *RH+WS* interaction term slightly outperforms the other two in terms of regression standard errors, *p*-values and R^2, all the models produce fairly similar results. Through

visual inspection, there is no sign of multicollinearity since all the model terms are consistent with theoretical basis (significant with no sign reversals). This is also corroborated by the VIFs. By regressing the interaction terms on the remaining predictor, it is found that $VIF_{RH+WS} = 3.9494$, $VIF_{RH-WS} = 6.0205$, and $VIF_{FSH\times WS} = 6.7431$. The model with the *RH+WS* interaction term is also slightly preferred since its VIF = 3.9494 is lesser than 5 while the other two VIFs are slightly higher than the threshold value of 5.

2.9 Discussion of Results

It has been established in this work that visibility can be accurately determined from several meteorological factors. In the first instance, simple regression analysis is used in the estimation of visibility using relative humidity, fractional sunshine, temperature, atmospheric pressure and wind speed. A multiple regression analysis is then introduced to take advantage of the variety of available meteorological factors. The results obtained are summarized in two parts, SLR models and MLR models.

2.9.1 SLR models

As mentioned before, in a regression model it is desired to test the significance of the parameters included in the model. By testing for the significance of the parameter coefficients, a decision can be made regarding the significance of the parameter concerned. All the tests are performed at 5% significant level. In practical terms, it is not enough just to have information about the significance of parameters, generally there exist a hypothesis about the parameters. For example, it is expected that full sunshine hours (clear skies) result in increased visibility. Any result in the contrary merits further investigation as the model integrity may be compromised. The 95% confidence interval (CI) for the model coefficients are presented in Table 2.10 to provide further insight into the model performance. The lower and upper bounds of the confidence interval are denoted L_b and U_b, respectively.

Table 2.10: Confidence intervals for SLR models

	RH		FSH		WS	
CI	β_0	β_{RH}	β_0	β_{FSH}	β_0	β_{WS}
L_b	65.27	-0.87	-3.82	29.88	5.90	2.17
U_b	87.50	-0.56	4.52	41.73	14.29	3.77

As shown in Table 2.10, for the 95% confidence level the confidence interval for the intercept term, β_0 for *FSH* crosses the zero mark. Therefore, this makes it difficult to specify the direction of its effect. This behaviour is significant in the *FSH* model. As mentioned in Section 2.4, the intercept term is not a predictor

variable, therefore it might be reasonable to ignore it in the *FSH* model. By setting $\beta_0 = 0$ in the *FSH* model, the reduced model will only consist of the *FSH* term. The regression now changes to what is commonly known as a regression through the origin (RTO). The confidence interval for the coefficient of *FSH*, β_{FSH} was found to be within [35.6 37.0]. Obviously the CI width for β_{FSH} has narrowed compared to that shown in Table 2.10 (with intercept). As stated in Section 2.4, the model performance generally remains unchanged. However, this model might lack practical interpretation due to the inference that when *FSH* = 0, *VSB* = 0 as well. The difficulty of interpretation arises simply because there is no measurement recorded near *FSH* = 0.

2.9.2 MLR models

In the presence of multiple meteorological factors, a multiple regression model is presented in Section 2.6. By including all the three predictors (based on their high correlation with visibility) in the model, the regression results are shown in Table 2.6. The MLR model performed better than all the SLR models in terms of the Regression SE, R^2, and *p*-value. In comparison, the model performance results can be seen in Table 2.11. The model containing all the predictor variables is denoted MLR_{ALL}.

Table 2.11: Comparison between SLR and MLRALL model

	RH	*FSH*	*WS*	MLR_{ALL}
RMSE	0.9951	0.7713	1.2058	0.4915
R^2	0.9130	0.9477	0.8723	0.9830
p-value	1.3×10^{-6}	9.8×10^{-8}	8.85×10^{-6}	2.0294×10^{-7}

As in simple regression models, the objective is to reliably specify a model with some degree of confidence in the parameters included in the model. For any of the variables x_{im} included in the MLR model, the null hypothesis states that the coefficient β_m is not different from 0, with the alternative stating that β_m is significantly different from 0. The sensitivity of the coefficients of the MLR model parameters is quantified through the 95% confidence intervals.

Table 2.12: CIs of the MLRALL model coefficients

CI	β_0	β_{RH}	β_{FSH}	β_{WS}
L_b	14.0776	-0.5782	12.9253	-1.4341
U_b	57.1876	-0.1299	34.4704	0.7904

In Section 2.7, it was determined through the variance inflation factor (VIF) that the estimated coefficient for *WS* (b_{WS}) is highly inflated. The same conclusion can be reached by observing the CI of the coefficients in question. As seen from Table 2.12, the expected mean value of this coefficient swing from negative to positive values, indicating its lack of significance. The lack of statistical significance in this model parameter makes it difficult to specify a reliable model due to the wide CI of the parameter coefficient. The relatively low RMSE and high R^2 values may be applicable to specific samples and may not be representative of the overall data population. The performance of the MLR_{ALL} model is also shown in Figure 2.5 against the measured data. In the same figure, the results of the normality test are shown. The error distribution does not indicate any significant deviation from the normality assumption. Figure 2.5 also shows the performance of $VSB_{RH\&FSH}$ model (MLR model (2.16) after the removal of the *WS* predictor term) against measured data in the year 2017. The $VSB_{RH\&FSH}$ model contains the *RH* and *FSH* predictor terms alongside its intercept as depicted in Table 2.8.

2.9.2.1 MLR with moderately correlated predictors

In Section 2.7, it was shown that the lack of model specificity in MLR may be due to a severe case of multicollinearity. By regressing each predictor term on the remaining ones, it was established through VIFs that indeed some parameters have strong linear relationships with others. Specifically, it was found that *WS* and *FSH* are highly correlated (R = 0.93). The first approach in dealing with multicollinearity was to eliminate the redundant term in the model i.e. excluding *WS* from the final model. The case where *WS* was eliminated was explored and the results are presented in Table 2.8. Overall, it was found that the issue of multicollinearity was adequately addressed without any loss in model precision. The confidence intervals of the model coefficients also show stability since they no longer cross the zero mark as depicted in Table 2.13.

Table 2.13: CIs of the MLR model coefficients without correlated predictors

CI	β_0	β_{RH}	β_{FSH}
L_b	14.7927	-0.4878	13.5040
U_b	50.1953	-0.1438	30.3471

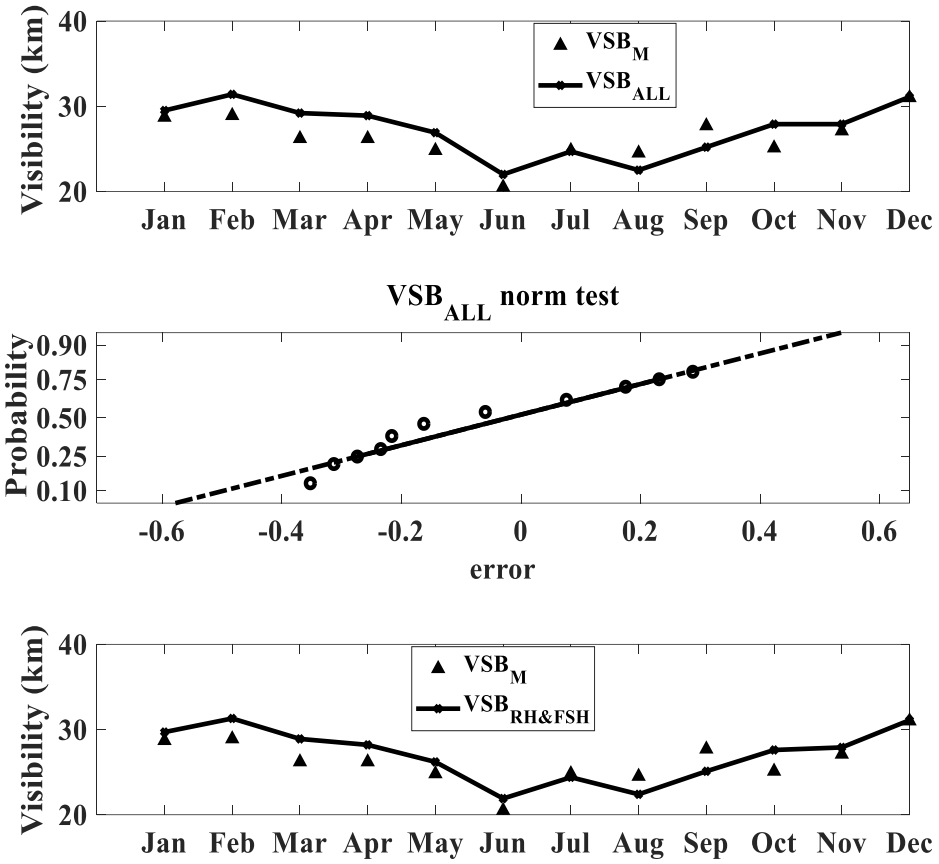

Figure 2.5: MLR model including all the predictors and the error normality test for January-December, 2017.

The performance of the model in which the highly correlated term *WS* is excluded is shown in Figure 2.5. It can be seen that the model estimates the expected visibility satisfactorily throughout the year. In Table 2.13, all the parameter coefficients of the model with *FSH* and *RH* have a narrower CI width than they had in MLR_{ALL} model shown in Table 2.12. The CI width of the intercept term, β_0 is ≈ 35 in Table 2.13 compared to ≈ 43 in Table 2.12 while the coefficient of *RH* has a CI of ≈ 0.344 in Table 2.13 as opposed to ≈ 0.448 in Table 2.12. Also, β_{FSH} has a CI of ≈ 17 in Table 2.13 as opposed to ≈ 22 in Table 2.12.

2.9.2.2 MLR with interaction terms

An alternative approach was presented in Subsection 2.8.2 which deals with effects of multicollinearity. It was shown therein that combining the highly correlated predictor terms in some way can alleviate the effects

of multicollinearity in multiple regression model. In this case, the parameters of concern are *RH*, *WS* and *FSH* which have been shown to be highly correlated. By combining *RH*, *WS* and *FSH* new variables are generated, in this work, *RH+WS*, *RH-WS*, and *WS×FSH* are used.

Table 2.14: CIs of the MLR model coefficients with interaction terms

Model	β_0	β_I	β_{FSH}
RH + WS	L_b = 17.1111	L_b = -0.5441	L_b = 16.7554
	U_b = 54.6269	U_b = -0.1703	U_b = 31.1227
RH - WS	L_b = 11.3775	L_b = -0.4314	L_b =11.3763
	U_b =45.4996	U_b = -0.1081	U_b = 30.7352
Model	β_0	β_I	β_{RH}
WS × FSH	L_b = 18.6528	L_b = 0.2766	L_b = -0.6739
	U_b = 71.9696	U_b = 2.6483	U_b = -0.0384

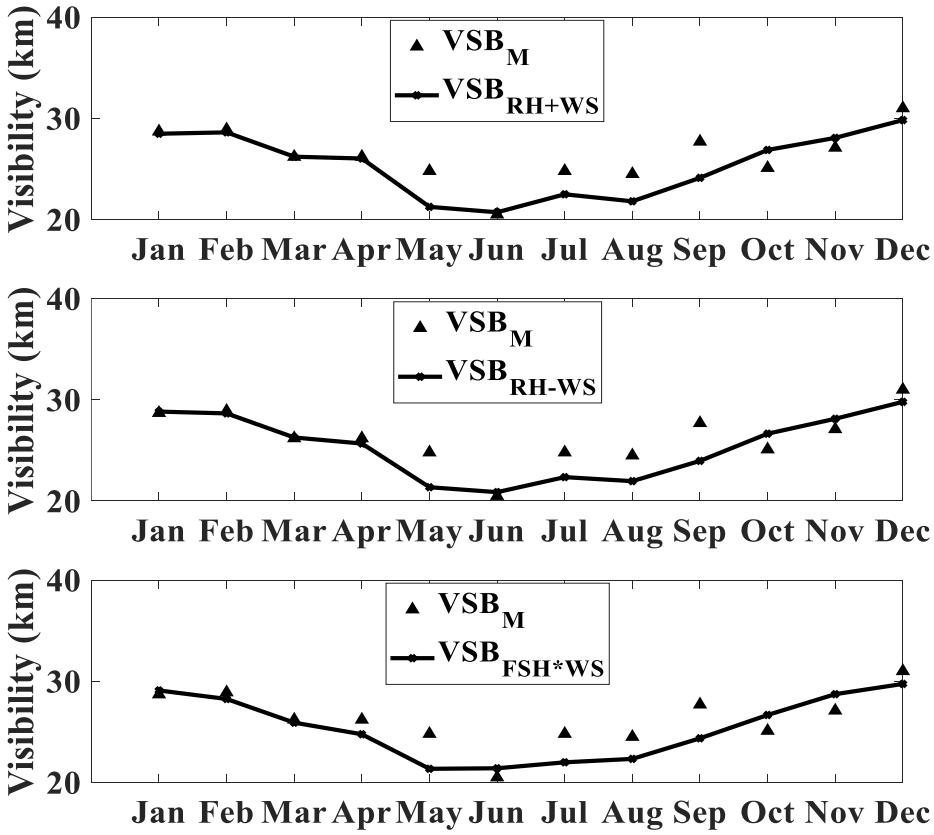

Figure 2.6: MLR fitting with interaction terms for January-December, 2017.

It is possible that other combinations may also work which include these basic terms in their formulation but in this work, these three are considered adequate for the Cape Town location. The model parameter coefficients were tested at 5% significant level as well as by investigating their VIFs. In all cases the coefficients were found to be significant. The confidence intervals for all the three models are shown in Table 2.14. By observing the model parameter coefficient CIs, all the parameters included in all three models are significant. The performance of the models with interaction terms has been summarized in Table 2.9. The monthly estimation of average visibility throughout the year is shown in Figure 2.6 using the models with interaction terms. The measured visibility is denoted as VSB_M while the models with interaction terms are denoted VSB_{RH+WS}, VSB_{RH-WS}, and $VSB_{FSH\times WS}$ for *RH+WS*, *RH-WS*, and *FSH×WS* models, respectively. It can be seen from Figure 2.6 that the regression models estimate visibility accurately throughout the year.

Table 2.15: Regression equations for other cities in South Africa

City	Regression Equation	Correlation Coefficient	Regression Standard Error
Bloemfontein	$VSB_{BLOEM} = 27.9547 + 1.7476\times10^{-4}(Temp \times AP)$	0.9304	0.3531
Johannesburg	$VSB_{JHB} = 10.1288 + (0.1937 \times Temp) + (1.3808 \times WS)$	0.8888	0.6750
Kimberley	$VSB_{KIM} = 40.7399 - 0.0378(RH + WS)$	0.8303	0.2443
Durban	$VSB_{DBN} = 15.4965 + (5.6239 \times FSH)$	0.6580	0.7743
Kruger Mpumalanga	$VSB_{MPU} = 15.9984 - 8.6808\times10^{-5}\left(Temp^{(WS)}\right)$	0.6386	0.7823
Polokwane	$VSB_{POL} = 24.9626 - 0.0135(AP \times FSH)$	0.8431	0.8234
Port Elizabeth	$VSB_{PE} = 16.8358 + (15.4479 \times FSH)$	0.6190	0.7921

2.9.3 FSO Visibility

In the planning process for the deployment of FSO systems, visibility at a location is a key component for designers. The available measured visibility data used in this work is based on a 5% threshold of the visible light. In other words, of the total transmitted signal, 95% is scattered and/or absorbed by the atmosphere. This threshold was adopted by the World Meteorological Organisation as it meets the aeronautical requirements [21]. In principle, the value of 0.05 ensures a reliable resolution of a black object against the horizon in daylight at a wavelength of 550 nm where the human eye has the highest sensitivity. The received 5% intensity of visible light corresponds to around -13 dB of the source intensity. However, the photodiodes

used in FSO systems typically have a receive sensitivity of about -30 dB (~0.001 of the transmitted intensity) or less [22], which is much lower than the eye sensitivity. In contrast with the 5% visible light threshold, FSO receivers can detect down to 0.1% of the transmitted intensity. This translates into longer visibility away from the transmitter for FSO systems as compared to visible light reception by the eye. At a distance L from the source, the signal intensity $I(L) \propto \left(1/L^2\right)$. Therefore, the optical visibility at 0.1% threshold is much higher than that recorded for meteorological visibility. If the transmitted intensity is I_0, when the receiver sensitivity is adjusted from $0.05 \times I_0$ to $0.001 \times I_0$ the optical visibility will be higher than the meteorological visibility by a factor of $\left(10/\sqrt{2}\right)$ for the same wavelength (550 nm) under the same weather conditions. In this view, as a future study it should be considered to translate measured meteorological visibility into optical visibility for determination of atmospheric attenuation coefficients.

2.10 Conclusion

The modeling of visibility has been presented through regression analysis. It has been shown in this study that meteorological parameters at a location can be used adequately to model and possibly predict optical signal visibility. As shown in the discussions, all models presented have a good agreement with the measured data. In the case of multiple regression models, the significance of the model parameters is achieved by reducing the effects of multicollinearity. The choice of the model may not be reliant on just its performance but rather the availability of the parameters as well. SLR models can be used in situations whereby a single meteorological parameter is measured reliably over a long period of time in the absence of others. Otherwise, it is preferable to use MLR models to take into account all the different constructs each parameter describes. However, caution must be exercised when too many parameters are available to avoid model over-specification. In such cases, the fitting algorithm may capture the idiosyncratic properties of that specific data rather than the true underlying trend of how visibility actually varies. In locations where measured visibility data is not available, visibility may be inferred from measurement data collected in locations with similar weather patterns. As part of future work, the performance of these visibility regression models will be compared with various artificial neural network predictive models such as the Generalized Regression Neural Network (GRNN), Multi-Layer Perceptron (MLP) neural network and Gaussian Process Regression (GPR) Delta based method.

References

[1] C. Yu, L. Yu, Y. Wu, Y. He, and Q. Lu, Uplink scheduling and link adaptation for narrowband Internet of Things systems, *IEEE Access, Volume 5, February 2017, Pages 1724-1734.*

[2] I. Alimi, A. Shahpari, V. Ribeiro, N. Kumar, P. Monteiro, and A. Teixeira, Optical wireless communication for future broadband access networks, *2016 21st European conference on networks and optical communications (NOC), pp. 124-128, Lisbon, Portugal, June 2016.*

[3] G. Parca, A. Tavares, A. Shahpari, A. Teixeira, V. Carrozzo, and G. T. Beleffi, FSO for broadband multi service delivery in future networks, *2013 2nd International Workshop on Optical Wireless Communications (IWOW), pp. 67-70, Newcastle upon Tyne, UK, October 2013.*

[4] Z. Ghassemlooy, W. Popoola, and S. Rajbhandari, *Optical wireless communications: system and channel modelling with Matlab*® (CRC press, 2019).

[5] A. Ceruti, T. Bombardi, and L. Piancastelli, Visual Flight Rules Pilots Into Instrumental Meteorological Conditions: a Proposal for a Mobile Application to Increase In-flight Survivability, *International Review of Aerospace Engineering (IREASE), Volume 9,* (Issue 5), *2016, Pages 144-151.*.

[6] A. Usman, G. Ismaila, K. Olaore, and S. Lawal, Developing a model for predicting the visibility for Sokoto using fraction of sunshine hours data, *Research Journal of Applied Sciences, Volume 6,* (Issue 6), *2011, Pages 378-380.*

[7] A. Usman, K. Olaore, and G. Ismaila, Estimating visibility using some Meteorological data at Sokoto, Nigeria, *Int. J. Basic Appli. Sci, Volume. 1,* (Issue 4), *April 2013, Pages 810-815.*

[8] D. Akpootu, M. Iliyasu, W. Mustapha, S. Aruna, and S. Yusuf, Developing Regression Models for Estimating Atmospheric Visibility over Ikeja, Nigeria, *Journal of Scientific Research and Reports,Volume 15,* (Issue 6), *September 2017, Pages 1-14.*

[9] S. Balamurugan and T. Alwarsamy, Boring Tool Chatter Suppression Using Magneto-Rheological Fluid Damper through Regression Models, *International Review of Mechanical Engineering (IREME), Volume 7,* (Issue 3), *2013, Pages 556-562.*

[10] T. Deb and S. Kumar Pal, Study on Uplift Behavior of Single Belled Anchor Piles in Sand Bed and Multiple Regression Analyses, *International Review of Civil Engineering (IRECE), Volume 8,* (Issue 3), *2017, Pages 97-112*.

[11] R. Idroes, T. R. Noviandy, A. Maulana, R. Suhendra, N. R. Sasmita, M. Muslem, *et al.*, Retention Index Prediction of Flavor and Fragrance by Multiple Linear Regression and the Genetic Algorithm, *International Review on Modelling And Simulations (IREMOS), Volume 12,* (Issue 6), *2019, Pages 373-380.*

[12] K. S. Jai Aultrin and M. D. Anand, Optimization of Machining Parameters in AWJM Process for Lead Tin Alloy Using RSM and Regression Analysis, *International Review Of Mechanical Engineering (IREME), Volume 9,* (Issue 2), *2015, Pages 136-144*.

[13] B. Thanga Parvathi and S. MercyShalinie, Differential Evolution (DE) based Multiple Regression Model for Classification, *International Review on Computers and Software (IRECOS), Volume 9,* (Issue 6), *2014, Pages 1117-1124.*

[14] E. Kinab, T. Salem, and G. Merhy, BIPV building integrated photovoltaic systems in mediterranean climate, *International Conference on Renewable Energies for Developing Countries 2014, pp. 180-185, Beirut, Lebanon, November 2014.*

[15] M. Sanz, A. Carrara, C. Gimeno, A. Bucher, and R. Lopez, Effects of a dry and warm summer conditions on CO2 and energy fluxes from three Mediterranean ecosystems, *Geophys. Res. Abstr, Volume 6, 2004, Page 3239.*

[16] T. Silva, R. Vicente, F. Rodrigues, A. Samagaio, and C. Cardoso, Performance of a window shutter with phase change material under summer Mediterranean climate conditions, *Applied Thermal Engineering, Volume 84, June 2015, Pages 246-256*.

[17] E. Xoplaki, J. F. González-Rouco, J. Luterbacher, and H. Wanner, Mediterranean summer air temperature variability and its connection to the large-scale atmospheric circulation and SSTs, *Climate dynamics, Volume 20,* (Issue 7-8), *March 2003, Pages 723-739.*

[18] G. James, D. Witten, T. Hastie, and R. Tibshirani, *An introduction to statistical learning* (Springer-Verlag New York, 2013).

[19] S. Sheather, *A modern approach to regression with R* (Springer-Verlag New York, 2009).

[20] M. H. Kutner, C. J. Nachtsheim, J. Neter, and W. Li, *Applied linear statistical models* (McGraw-Hill Irwin New York, 2005).

[21] M. Jarraud, Guide to meteorological instruments and methods of observation, *World Meteorological Organisation (WMO), Geneva, Switzerland, Volume 1,* (Issue 8), *2008, Page 29.*

[22] A. Prokes, Atmospheric effects on availability of free space optics systems, *Optical Engineering, Volume 48,* (Issue 6), *June 2009, Page 066001*.

Chapter 3

3 Journal Article 2

Terrestrial Free Space Optical Communication Systems Availability based on Meteorological Visibility Data for South Africa

Olabamidele O. Kolawole, Thomas J.O. Afullo, Modisa Mosalaosi

Published: *South African Institute of Electrical Engineers (SAIEE) Africa Research Journal*, 2022, vol. 113, no. 1, DOI: 10.23919/SAIEE.2022.9695423

3.1 Abstract

In spite of the numerous advantages of employing free space optical (FSO) communication systems as viable complementary platforms for next-generation networks, the presence of atmospheric disturbances such as fog and scintillations are major sources of signal impairment which degrade system performance. Consequently, it becomes imperative to investigate and contextualize the unique climatic conditions in those locations where FSO links are to be deployed. Statistical evaluation of meteorological visibility data collected for various cities in South Africa is thus hereby employed in estimating the availability performance of FSO links transmitting at both 850 nm and 1550 nm. It is determined that the cities of Mbombela and Cape Town have the lowest performance due to the high occurrence of fog events as compared to other regions in South Africa. During foggy periods, FSO links in Mbombela and Cape Town would have availabilities of ~99.6% for link distances of 500 and 600 metres, respectively. The bit error rate (BER) estimations of intensity modulation and direct detection (IM/DD) FSO links in the presence of weak atmospheric turbulence were also investigated for the identified locations during foggy weather; with the cities of Mafikeng and Kimberley showing the lowest BER performances because of their high wind velocities, altitudes and refractive index values. In order to obtain a BER of 10^{-6}, receive signal-to-noise ratio (SNR) values ranging from ~46 to ~51 dB are required for FSO links deployed for data transmission in the various cities investigated in this work.

3.2 Introduction

Rising urbanization, population growth, increase in housing costs, and demand for higher standards of living have generated an urgent need for smart cities to maximize resource use [1]. Based on the International Mobile Telecommunications 2020 (IMT-2020) vision of the International Telecommunication Union (ITU), the fifth generation (5G) technology is expected to support enhanced mobile broadband (eMBB) with throughputs up to 10 Gbits/s, massive machine type communication (mMTC) for up to 1 million connections per square km, and ultra-reliable low latency communication (uRLLC) as low as 1 ms. This is to ensure that intelligent traffic systems, internet of vehicles (IoV), and internet of things (IoT) connections in emerging smart cities function optimally. 5G technology is also needed to meet the high requirements on speed for virtual reality (VR), augmented reality (AR) and mixed reality (MR) applications [2]-[4].

FSO communication is a viable complementary solution platform for next-generation communication networks, whether as a standalone or hybrid technology. When employed in 5G cellular backhaul networks, its numerous advantages include: flexible network connectivity, secure transmission, high data throughput, ease of installation, relative low cost of deployment, immunity to electromagnetic interference, license-free spectrum, low latency communication, low bit error rate (BER), etc. [5]. Despite these numerous merits, the performance of FSO links is severely affected by weather constraints. Aerosol scattering attenuation due to fog and atmospheric turbulence due by scintillations are major sources of signal impairment, hence impacting on the received signal quality [1], [5], [6].

Hybrid FSO - Millimeter wave (FSO/MMW) links for FSO-based backhaul networks have been proposed in literature. These are aimed at obtaining reliable and uninterrupted network connectivity by switching between the main FSO link and the backup MMW link whenever the main FSO link is unavailable due to weather constraints. Dual FSO thresholds are incorporated in the system to prevent unnecessary switching between links [6]. In [7], the performance analysis of a FSO/MMW system incorporated with a flying network platform (FNP) which employs point to point FSO/MMW links to pass backhaul traffic between the access and core networks is carried out. While the results obtained in [6]-[7] indicate that the proposed hybrid FSO links outperform the single FSO link, it is important to state that thorough estimations of signal losses based on the climatic constraints of the various locations where the links are to be deployed was not done. This is imperative in determining the switching thresholds of the proposed links which may differ from one location to another.

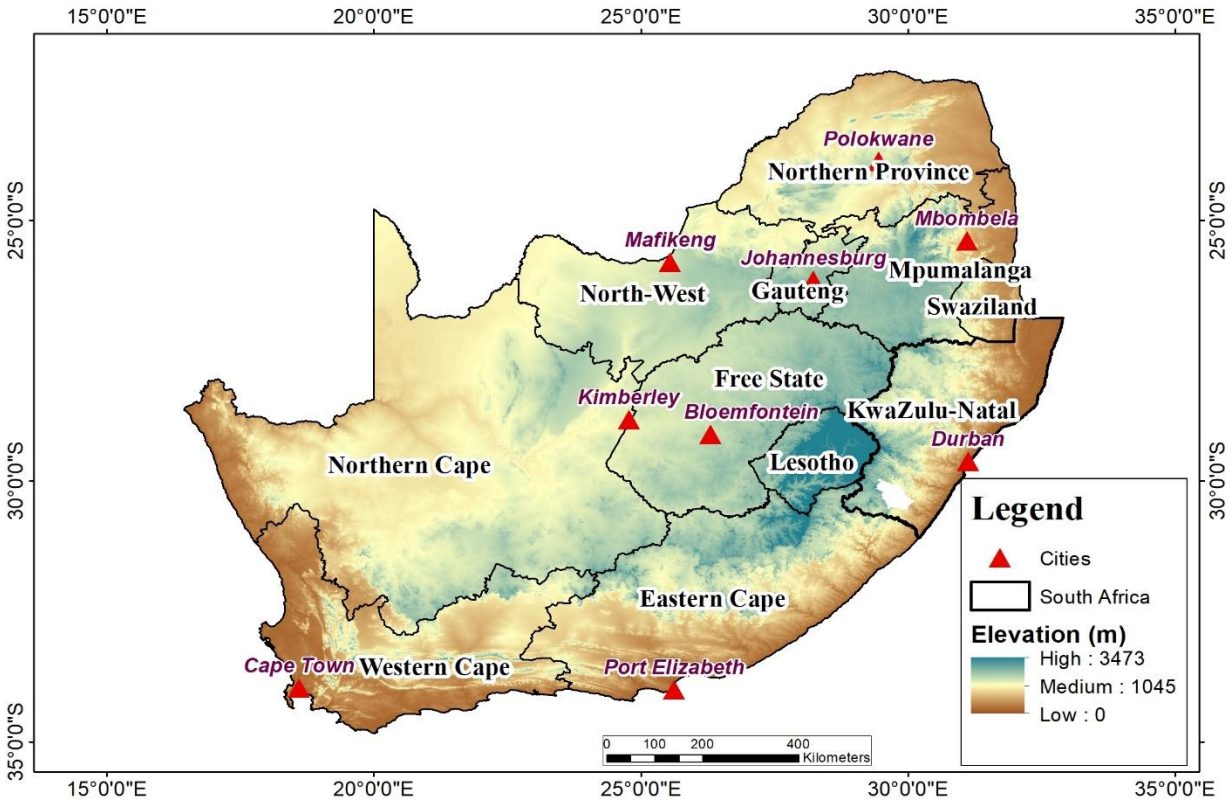

Figure 3.1: Map of South Africa showing elevation above sea level and locations of selected cities investigated in this work.

South Africa's climate is considered highly variable spatially and temporally. The spatial differences in elevation across the country play an important part in this variability (Figure 3.1). Locations of the various cities investigated in this work are highlighted in Figure 3.1 across the South African geographical space. According to the Köppen-Geiger climate classification for South Africa developed by the Council for Scientific and Industrial Research (CSIR), the country is classified predominantly as semi-arid, with influences from temperate and tropical zones [8]-[9]. Mafikeng, Kimberley and Bloemfontein have northern steppe climates; Bloemfontein has cold arid weather while Mafikeng and Kimberley are majorly arid and hot. Johannesburg and Mbombela have mild temperate climates with the former being high-veld while the latter is low-veld. Durban has a humid subtropical climate while Cape Town is classified as a Mediterranean climate with warm summers and wet winters. Polokwane has a Bush-veld climate that is arid, with hot summers and cold winters while Port Elizabeth has a southern coastal climate characterized by rain during all seasons [10]-[12].

Most of the proposed FSO and hybrid FSO systems in literature are constrained in their ability to estimate

the losses encountered by FSO links in every location they are to be deployed. The focus of this paper is in determining the attenuations based on the atmospheric conditions prevalent in all the climatic zones of South Africa. It is also important to state that the cities chosen are urban places with considerable population, hence great demand for high data rates and fast internet connectivity.

Table 3.1: Description of the climate of selected cities in South Africa [8]-[12].

City	Climate
Bloemfontein	Northern Steppe (Arid and cold)
Cape Town	Mediterranean
Durban	Subtropical
Johannesburg	High-veld (Warm Temperate)
Kimberley	Northern Steppe (Arid and Hot)
Mafikeng	Northern Steppe (Arid and Hot)
Mbombela	Low-veld (Temperate)
Polokwane	Bush-veld (Arid and Hot)
Port Elizabeth	Southern Coastal Belt

The following are the key contributions of this work:

1) Cumulative distribution of visibility and aerosol scattering attenuations based on the Ijaz and Kim models for transmission wavelengths of 850 and 1550 nm in nine cities of South Africa are presented.
2) Probabilities of exceedance, deceedance and encountering of different aerosol scattering attenuations for 850 and 1550 nm are calculated and their impact on FSO link performance investigated for all the various locations of interest.
3) Modeling of the minimum required visibility CDFs during foggy and clear weather conditions are presented. To the best of our knowledge, approximate polynomial expressions for determining the minimum required visibilities for FSO systems transmitting at 1550 nm in various locations have not been reported in open literature so far.
4) Determined link availability performances for two commercial FSO links are presented during foggy and clear weather conditions.
5) Numerical expressions for obtaining the BER for FSO systems employing IM/DD with non-return-to-zero on-off keying (NRZ-OOK) modulation under the influence of weak turbulence are presented. Achievable SNRs and data rates of the two FSO links are also investigated.

The rest of this paper is structured as follows: Section 3.3 presents the visibility distribution of nine cities

in South Africa; Section 3.4 presents and analyzes the cumulative distribution of aerosol scattering attenuation based on the Kim and Ijaz models for the two transmission wavelengths in the locations of interest, with the probabilities of exceedance, deceedance and encountering of various scattering attenuations calculated and discussed therein. The link budgets for two commercial FSO communication systems are provided in Section 3.5; while Section 3.6 presents the minimum required visibility CDFs with the corresponding polynomial coefficients. The approximate expressions for evaluating the link availability performance are determined in Section 3.7. In Section 3.8, the SNR, BER and data rate equations of received signals for FSO links in a weak turbulence regime are derived and their results analyzed; while the conclusions are presented in Section 3.9.

3.3 Visibility Distribution

The scattering and absorption of optical signals is strongly impacted by visibility. Meteorological visibility may be defined as the distance in the atmosphere at which a fraction of the luminous flux transmitted by a collimated beam emanating from a 550 nm light source is reduced to 5% of its value. In other words, it is the optical range determining how far away objects can be seen under certain weather conditions such as snow, rain, haze etc.[13]-[14]. The presence of suspended fine water droplets in the atmospheric layer closest to the surface of the earth results in the formation of fog. Fog is a weather condition where visibility drops below 1000 m and the atmospheric humidity approaches 100% [15]. Visibility data from January 2010 till June 2018 was obtained for major cities in each of the nine provinces of South Africa from the South Africa Weather Service (SAWS). These urban areas of interest are Bloemfontein, Cape Town, Durban, Johannesburg, Kimberley, Mafikeng, Mbombela, Polokwane and Port Elizabeth. The data was collected three times daily (8:00 a.m., 2:00 p.m. and 8:00 p.m.) for the 8½ year period.

Figure 3.2(a) shows the visibility under fog conditions (0 to 1 km) against the percentage of time the visibility events took place while Figure 3.2(b) shows the duration of visibility events up to 20 km over the time period investigated for all the selected locations in South Africa. In Figure 3.2(a), Mbombela and Cape Town have fog events that last up to 1% of the time considered, while Port Elizabeth, Polokwane, Johannesburg, and Bloemfontein experience foggy events less than 0.5% of the time. Foggy incidents occur less than 0.07% of the time for Durban, Kimberley, and Mafikeng, according to the processed data. Figure 3.2(b) best captures the visibility under haze and clear weather conditions. The cities of Mbombela, Cape Town, Port Elizabeth, Polokwane and Johannesburg all have more visibility events under haze conditions than Kimberley, Mafikeng and Durban. Cumulative distributions of visibility based on average worst month, year and hour measurements for the same cities are shown in [16].

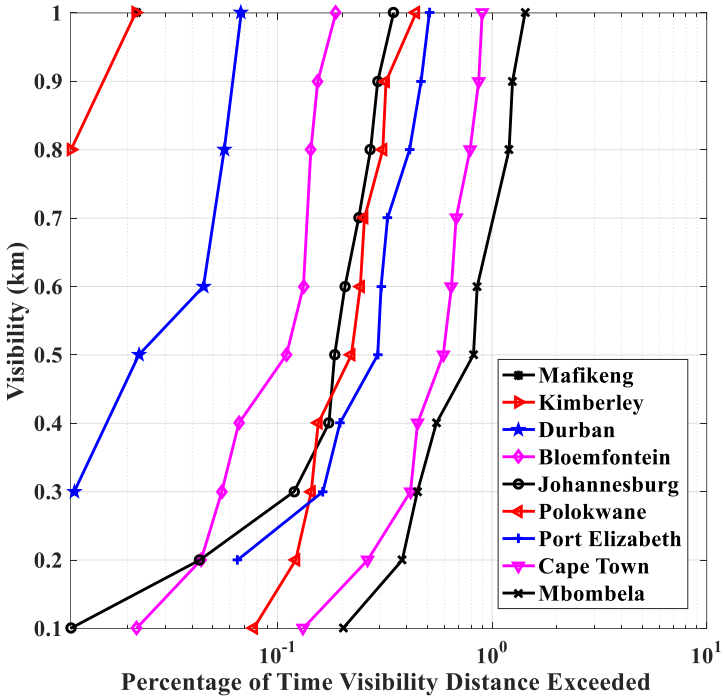

(a) Visibility under fog conditions

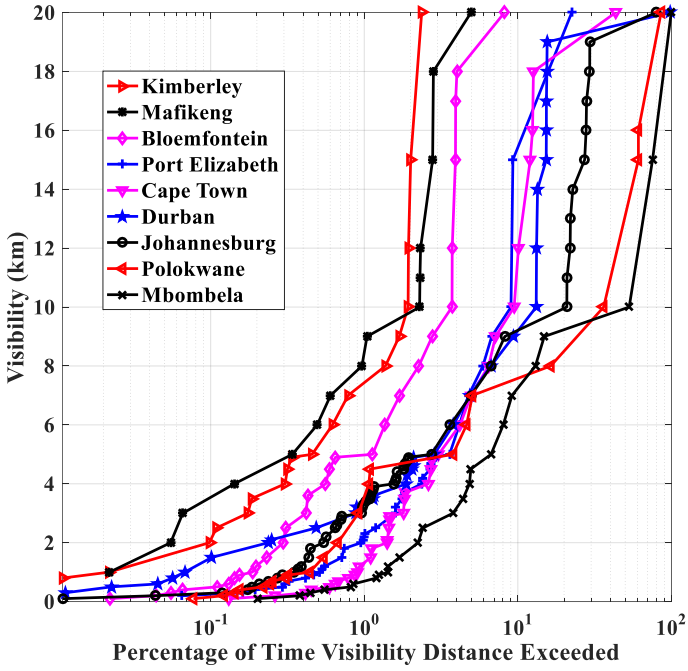

(b) Visibility up to 20 km

Figure 3.2: Visibility against percentage of time visibility distance exceeded for various cities in South Africa from January 1, 2010 to June 30, 2018 under (a) fog conditions and (b) haze and clear weather conditions.

3.4 Scattering Attenuation

The Beer-Lamberts law can be used to model the propagation of optical signals across the atmosphere. It is stated in [17] as:

$$\tau(\lambda, L) = e^{-(\alpha L)} \tag{3.1}$$

where $\tau(\lambda, L)$ is the transmittance of the atmosphere in (km^{-1}), α represents the atmospheric attenuation coefficient or total extinction coefficient, λ is the wavelength of the optical signal in nm and L is the distance of propagation in km. The Kruse model is used to calculate the coefficient of atmospheric attenuation from visible to near-infrared wavelengths. It is expressed as [17]-[18]:

$$\alpha = \frac{-\ln(T_{th})}{V}\left(\frac{\lambda}{\lambda_\circ}\right)^{-q_\circ} = \frac{3.912}{V}\left(\frac{\lambda}{\lambda_\circ}\right)^{-q_\circ} \tag{3.2}$$

where $T_{th} = 2\%$ is the optical threshold, $\lambda_\circ = 550nm$ is the solar band's maximum spectrum wavelength, λ is the wavelength of the optical signal in nm, V is the meteorological visual range in km and $q_\circ$ represents the particle size distribution parameter. The total extinction coefficient in decibel per unit length is given as:

$$\alpha_a(V) = \alpha 10\log_{10}(e) \approx 4.343\alpha \tag{3.3}$$

As optical signals traverse the free space media, discontinuities in the atmosphere, such as aerosols and gas molecules, act as sources of reduced signal power. Scattering losses, also known as atmospheric attenuation, are caused by these channel impediments and are calculated using [19]:

$$A_a(L,V) = \alpha_a(V) \times L \tag{3.4}$$

Since the aerosol scattering coefficient is the most influential atmospheric channel parameter for scattering losses in optical signals, the atmospheric attenuation is approximately equal to the aerosol scattering coefficient [19]-[20], that is:

$$\alpha_a(V) \cong \beta_{sa}(\lambda) \tag{3.5}$$

The aerosol scattering coefficient or specific atmospheric attenuation in dB/km, as given in [16]-[17] is:

$$\beta_{sa}(\lambda) = 10\log_{10}(e)\left(\frac{3.912}{V}\right)\left(\frac{\lambda}{\lambda_\circ}\right)^{-q_\circ} = \frac{17}{V}\left(\frac{\lambda}{\lambda_\circ}\right)^{-q_\circ} \tag{3.6}$$

Equation (3.6) describes the Kim and Ijaz fog models. In the Kim model, the particle size distribution parameter, $q_\circ$, is expressed in terms of all forms of visibility as [21]:

$$q_{\circ}(V)=\begin{cases}1.6 & for \quad V>50km\\ 1.3 & for \quad 6<V<50km\\ 0.16V+0.34 & for \quad 1<V<6km\\ V-0.5 & for \quad 0.5<V<1km\\ 0 & for \quad V<0.5km\end{cases} \tag{3.7}$$

For the Ijaz fog model, on the other hand, $q_{\circ}$, is given in terms of wavelength as [22]-[23]:

$$q_{\circ}(\lambda)=0.1428\lambda-0.0947 \tag{3.8}$$

Figures 3.3(a) and (b) show the cumulative distributions of scattering attenuation for major cities in South Africa. For visibility measurements less than 1 km, the Ijaz model was used to calculate scattering losses, while the Kim model was used to calculate the specific attenuation associated with visibility values greater than or equal to 1 km. The two models were used to estimate scattering losses encountered by transmission wavelengths of 850 and 1550 nm. In both figures, the cities of Johannesburg, Bloemfontein, Polokwane, Cape Town and Mbombela encounter scattering attenuation greater than 175 dB/km for periods ranging from 0.01 % to 0.2 % of the entire time considered. Specific attenuation below 100 dB/km was observed in Durban, Kimberley, and Mafikeng for periods less than 0.07 % of the time investigated.

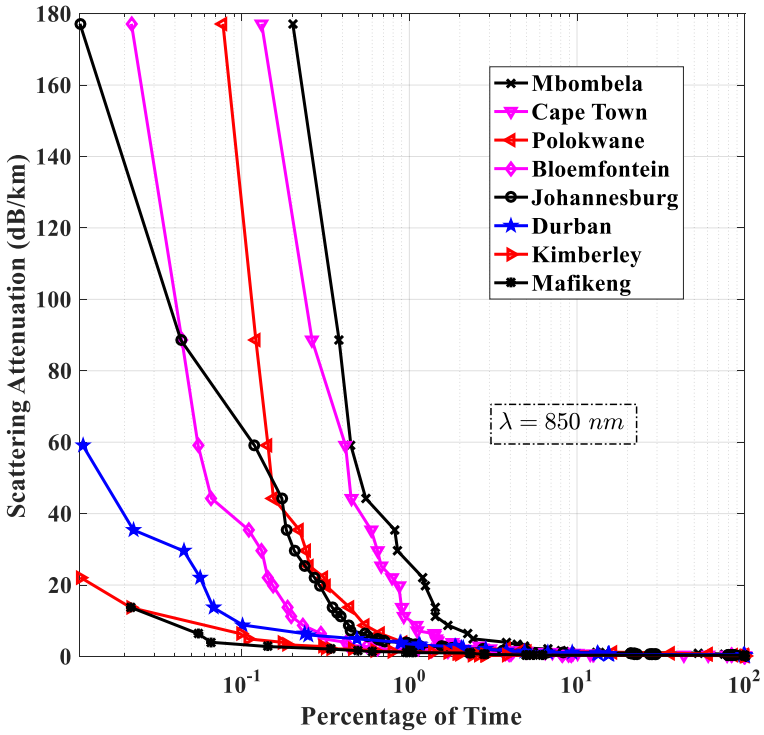

(a) 850 nm

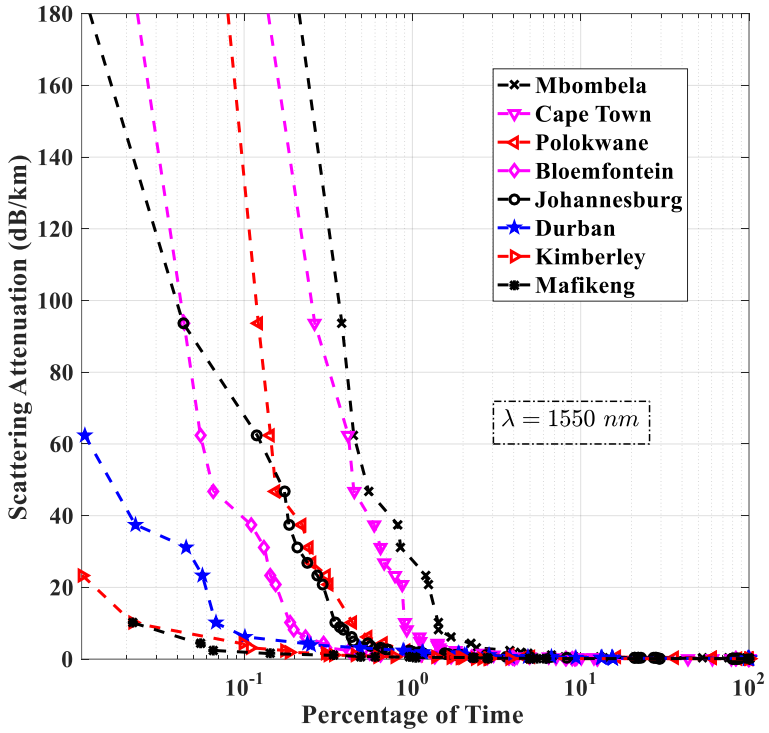

(b) 1550 nm

Figure 3.3: Cumulative distribution of Aerosol scattering attenuation for major cities in South Africa using Ijaz's and Kim's models from January 1, 2010 to June 30, 2018 for (a) 850 nm and (b) 1550 nm.

Before deploying an FSO system, it is critical to understand the weather constraints that will be faced in a given area and at a given time. Once the maximum attenuation the FSO system can tolerate is determined, the FSO system installer can predict the likelihood of system outage based on the probability of exceeding and encountering a specific atmospheric attenuation value. The probabilities of exceeding different scattering attenuation losses for 850 nm and 1550 nm wavelength systems are shown in Figures 3.4(a) and (b). In the cities of Mbombela, Cape Town and Polokwane, FSO systems transmitting at the two wavelengths have a likelihood of facing attenuation values greater than 80 dB/km with probabilities of 0.0038, 0.0026 and 0.0012, respectively. The probabilities of FSO links encountering different atmospheric attenuations when transmitting at 850 nm and 1550 nm are shown in Figures 3.5(a) and (b). The probability of FSO links encountering scattering losses of 177 dB/km and 187 dB/km at these wavelengths in Mbombela, Cape Town, Polokwane, Bloemfontein, and Johannesburg, are 0.0020, 0.0013, 0.0008, 0.0002 and 0.0001 respectively.

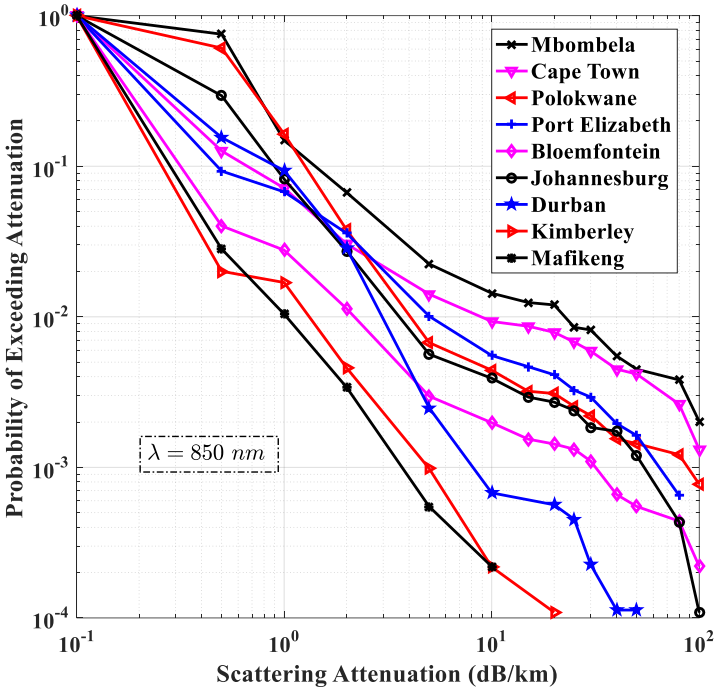

(a) 850 nm

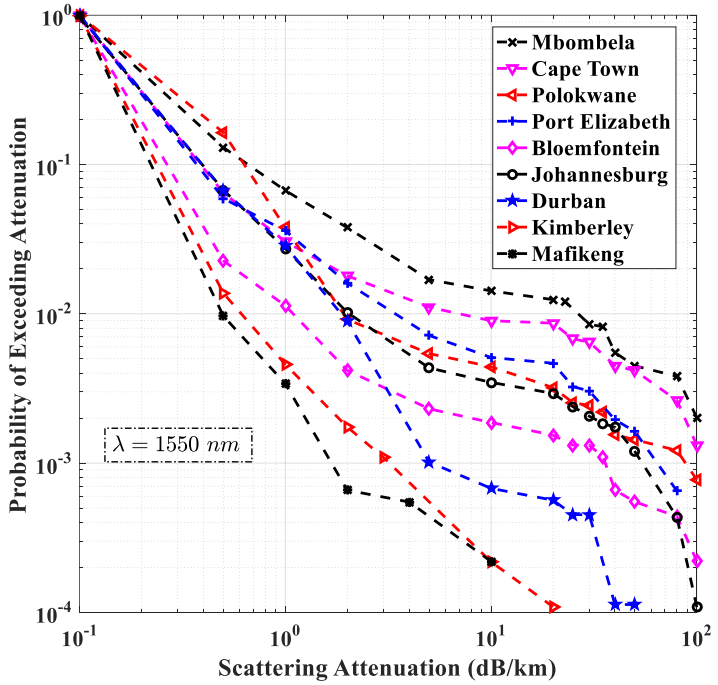

(b) 1550 nm

Figure 3.4: Probability of exceeding different atmospheric scattering attenuation conditions for major cities in South Africa for (a) 850 nm and (b) 1550 nm.

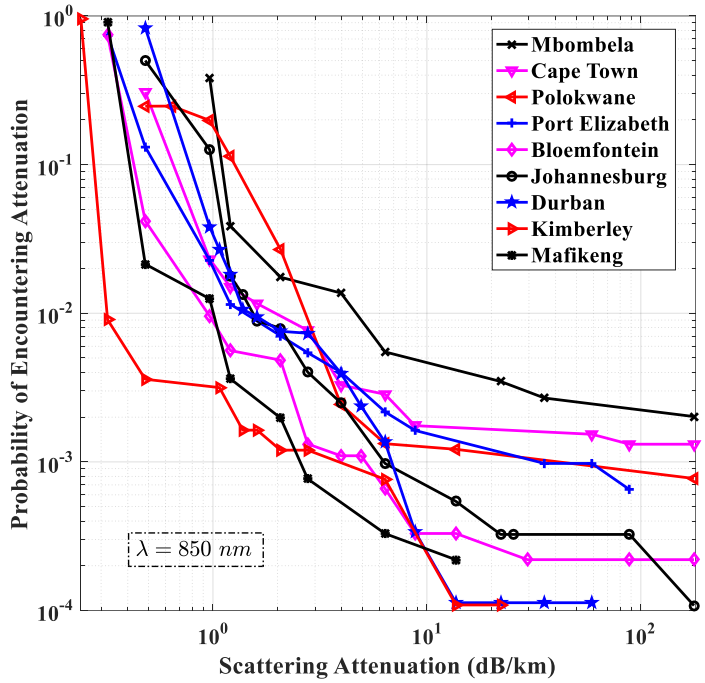

(a) 850 nm

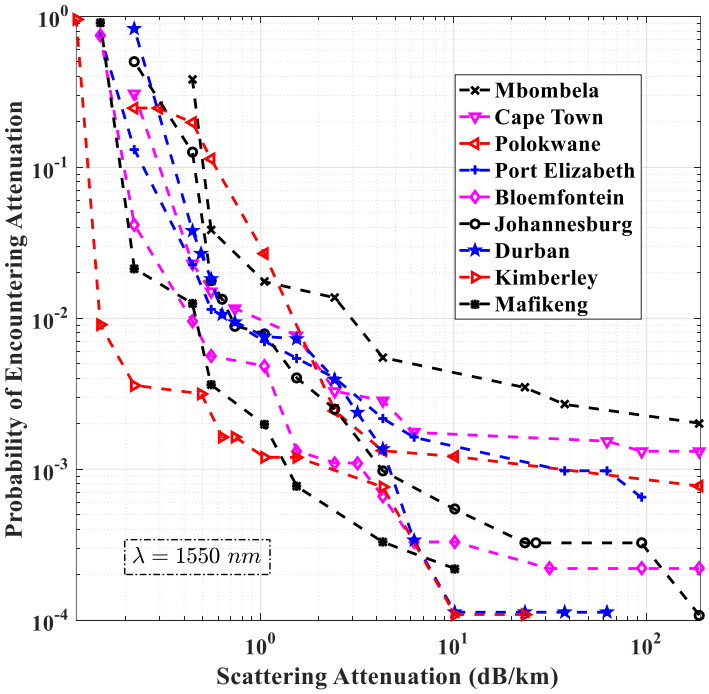

(b) 1550 nm

Figure 3.5: Probability of encountering different atmospheric scattering attenuation conditions for major cities in South Africa for (a) 850 nm and (b) 1550 nm.

Table 3.2: Most frequent fog measurements and their associated probabilities for major cities in South Africa.

Location	Most Frequent Fog Events (km)	Attenuation (dB/km) - 850 nm	Attenuation (dB/km) - 1550 nm	Probability of Encountering Scattering Attenuation (-)	Probability of Exceedance (-)
Cape Town	0.3	59.05	62.51	0.001534	0.004163
Port Elizabeth	0.5	35.43	37.51	0.000976	0.002929
Durban	0.6	29.53	31.25	0.000226	0.000451
Bloemfontein	0.5	35.43	37.51	0.000440	0.001100
Kimberley	0.8	22.14	23.44	0.000109	0.000109
Johannesburg	0.3	59.05	62.51	0.000759	0.001193
Mafikeng	1	13.67	10.13	0.000219	0.000219
Mbombela	0.8	22.14	23.44	0.003475	0.011993
Polokwane	0.5	35.43	37.51	0.000663	0.002209

Table 3.3: Most frequent visibility measurements and their associated probabilities for major cities in South Africa.

Location	Most Frequent Visibility (km)	Attenuation (dB/km) - 850 nm	Attenuation (dB/km) - 1550 nm	Probability of Encountering Scattering Attenuation (-)	Probability of Deceedance (-)
Cape Town	20	0.4827	0.2210	0.3075	0.8737
Port Elizabeth	30	0.3218	0.1474	0.7421	0.7437
Durban	20	0.4827	0.2210	0.8323	0.8448
Bloemfontein	30	0.3218	0.1474	0.7453	0.9079
Kimberley	40	0.2413	0.1105	0.9618	0.9623
Johannesburg	20	0.4827	0.2210	0.5010	0.7060
Mafikeng	30	0.3218	0.1474	0.9135	0.9379
Mbombela	10	0.9653	0.4421	0.3822	0.8514
Polokwane	15	0.6436	0.2947	0.2475	0.6381

Table 3.2 summarizes the scattering losses, probabilities of exceedance and the probabilities of encountering those losses associated with the most occurring fog events in the various cities in South Africa. The Ijaz model in (3.6) and (3.8) is used to compute the atmospheric attenuation values for the wavelengths of 850 and 1550 nm. The most frequent fog events in the cities of Cape Town and Johannesburg have a visibility of 300 m. The probability of encountering and exceeding the scattering attenuations associated with the most frequent fog event in Cape Town is 0.0015 and 0.0042, respectively; while in Johannesburg, the probabilities of encountering and exceedance of the specific attenuations are 0.0008 and 0.0012, respectively. The most frequent fog events in Kimberley and Mbombela have visibilities of 800 m. However, the probabilities of exceedance and encountering of the scattering losses associated with the fog event is higher in Mbombela than in Kimberley.

Table 3.3 summarizes the specific attenuations, as well as the likelihoods of deceedance and encountering of such losses, aligned with the most frequent visibility measurements in the different cities of South Africa. The probability of deceedance describes the possibility of encountering values lesser than or equal to certain atmospheric attenuations. It enables the FSO system installer to also predict the link availability, once the most frequent and maximum atmospheric attenuations to be encountered by the link is known. Cape Town, Mbombela and Polokwane have the lowest probabilities of encountering attenuations associated with their most frequent visibility measurements. However, Polokwane has the least probability of deceedance when comparing the three cities. This implies that the probability of exceedance or encountering of attenuations greater than those associated with the most common visibility in Polokwane is 0.3619 or 36.19 % of the time investigated.

3.5 Link budget

The level of signal power detected at the receiver is determined by the link budget of an FSO link [24]. The average optical power detected at the receiver is given below as:

$$P_{Rx} \cong P_{Tx} - \beta_{sa}(\lambda)L - F_{SL} + G_{Tx} + G_{Rx} - L_{Geo} - X_{Tx} - X_{Rx} \tag{3.9}$$

where P_{Tx} is the power of the transmitted optical signal in dBm, β_{sa} is the aerosol scattering loss in dB/km, L is the propagation distance in km, F_{SL} is the free space path loss in dB, G_{Tx} is the gain of the transmit lens in dB, G_{Rx} is the gain of the receive lens in dB, L_{Geo} is the optical geometric loss in dB, X_{Tx} is the aggregate loss at the transmitter in dB and X_{Rx} is the aggregate loss at the receiver in dB. X_{Tx} and X_{Rx} include all other system-dependent losses such as beam direction misalignment, random changes in the beam centroid position and decrease in sensitivity as a result of background solar radiation [20].

The free space path loss is expressed as [25]-[26]:

$$F_{SL} = 20\log\left(\frac{4\pi L}{\lambda}\right) \tag{3.10}$$

where λ is transmit wavelength of the signal in metres. The gain of the transmit lens is derived below as [26]-[27]:

$$G_{Tx} = 20\log\left(\frac{126.491}{\theta}\right) \tag{3.11}$$

where θ is the transmit beam divergence angle in radians. The gain of the receive lens is expressed as [27]-[28]:

$$G_{Rx} = 20\log\left(\frac{31.623\pi D}{\lambda}\right) \tag{3.12}$$

where D is the diameter of the receiver aperture in metres. The geometric loss is caused by the optical beam diverging from its path. It is given as [28]-[29]:

$$L_{Geo} = -20\log\left(\frac{D}{L\theta}\right) \tag{3.13}$$

The optical link power margin determines how well a system compensates for atmospheric attenuation losses over a given propagation distance. It is the benchmark for assessing the performance of the FSO link, and is presented as [30]:

$$L_m(L) = P_{Tx} - X_{Tx} - 20\log\left(\frac{\theta L\sqrt{2}}{D}\right) - X_{Rx} - R_s \tag{3.14}$$

where R_s is the sensitivity of the receiver in dBm.

Commercial FSO link parameters used in this paper are shown in Table 3.4. In calculating the optical link margin, the constant parameters of the FSO links in Table 3.4 are substituted into (3.14) which results in a simplified equation below:

$$L_m(L) = M_\circ - 20\log L \tag{3.15}$$

When the propagation distance, L, is in kilometres, the constant $M_\circ$ is equal to 24 dB when the parameters of the FSO link A are substituted into (3.14). This results in (3.16):

$$L_m(L)_{\text{Link A}} = 24 - 20\log L \tag{3.16}$$

When the parameters of FSO link B are substituted into (3.14), we have the simplified link margin equation for the FSO system transmitting at 1550 nm below:

$$L_m(L)_{\text{Link B}} = 28 - 20\log L \tag{3.17}$$

Some commercial FSO links currently manufactured, use 850 nm and 1550 nm wavelengths for signal transmission. In this work, the performance of two FSO links, labelled A and B are investigated. Typical FSO link parameters are shown in Table 3.4. Throughout this paper FSO link A transmits data signals on the 850 nm wavelength while FSO link B operates on the 1550 nm wavelength.

Table 3.4: Commercial FSO link parameters used in calculations

Parameter	FSO Link A	FSO Link B
Wavelength (λ)	850 nm	1550 nm
Transmit Power (P_{Tx})	16 dBm	20 dBm
Receiver Sensitivity (R_s)	-38 dBm	-40 dBm
Transmitter (X_{Tx}) and Receiver (X_{Rx}) System Losses	2 dB	4 dB
Receiver Aperture Diameter (D)	16 cm	10 cm
Eye Safety	Class 1 M	Class 1 M
Receiver Field of View	10 mrad	65 mrad
Transmit Beam Divergence Angle (θ)	2.8 mrad	1.75 mrad
Responsivity $(\Re)$	0.4 A/W	0.5 A/W
Bit Rate (R_b)	1.25 Gb/s	10 Gb/s

3.6 Minimum visibility

The minimum required visibility, $V_{\min}(L,V)$, must be determined for the FSO link to function optimally. It is a critical parameter for estimating the availability of an FSO link. It is presented in the form [16], [18]:

$$V \geq V_{\min}(L,V) \tag{3.18}$$

For a link to be available, the optical link margin must be greater than or equal to the atmospheric attenuation losses. That is [31]-[32]:

$$L_m(L) \geq A_\alpha(L,V) \tag{3.19}$$

The minimum required visibility, in kilometers, for the Ijaz and Kim models is given below as [16], [18]:

$$V_{\min}(L,V) = \frac{17L}{L_m(L)}\left(\frac{\lambda}{\lambda_\circ}\right)^{-q_\circ} \tag{3.20}$$

where the particle size distribution parameter, $q_\circ$, is presented for the Kim and Ijaz fog models in (3.7) and (3.8), respectively. Equation (3.18) therefore becomes:

$$V \geq \frac{17L}{L_m(L)}\left(\frac{\lambda}{\lambda_\circ}\right)^{-q_\circ} \tag{3.21}$$

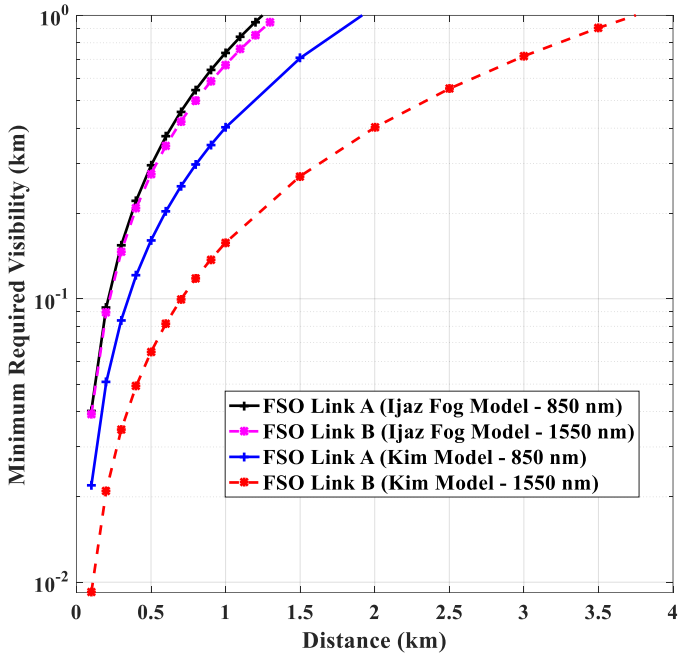

Figure 3.6: Minimum required visibility vs link distance based on Ijaz and Kim models for FSO links A and B.

Figure 3.6 is generated using the Ijaz model shown in (3.8), (3.16), (3.17) and (3.21) during foggy periods. The parameters of the commercial FSO links shown in Table 3.4 are used in the calculations as well. The minimum required visibility needed to achieve a link distance of 500 metres, is approximately 295 and 276 metres for the FSO links transmitting at a wavelength of 850 and 1550 nm, respectively.

The Kim model is used in computing the minimum required visibilities needed to achieve optimal link distances in Figure 3.6 as well. Equations (3.7), (3.16), (3.17) and (3.21) are used in the computations of the minimum required visibilities during haze and clear weather periods. In order to achieve path lengths of 1.5 kilometres, the minimum required visibilities for FSO links transmitting at 850 and 1550 nm are 0.70 and 0.27 kilometres, respectively. It can be deduced from Figure 3.6, that FSO links transmitting at 1550 nm achieve similar optimal link distances at lower minimum required visibilities than those transmitting at 850 nm.

A novel approach for estimating the availability of FSO links without the use of substantial visibility records is reported in [30], [32]. The cumulative distribution functions (CDF) of sample visibility data were fitted using the least squares third-order polynomial method. However, the approach used in [32] used only the Kim model for calculating the minimum required visibilities of FSO links transmitting at 850 nm from

visibility data obtained from different airports across Europe. Further research as reported in [17], [22], [23], propose that the Ijaz model is more accurate in computing aerosol scattering attenuation losses encountered by optical signals transmitting between wavelengths of 550 and 1600 nm for visibility measurements ranging from 15 to 1000 metres.

This necessitates the application of the Ijaz model in computing the CDFs of the minimum required visibilities and resultant link availabilities of FSO links during foggy weather. In this work, the same method implemented in [32] is also adopted, but only for estimating link availabilities of FSO links in clear weather, when visibility measurements are greater than 1 kilometer. The CDFs of minimum required visibilities during foggy weather are computed and the Ijaz model is used in estimating the availabilities of FSO links transmitting at 850 and 1550 nm in major cities of South Africa.

Similar to what was reported in [32], the third-order polynomial fitting method of the CDFs calculated, are a trade- off between simplicity and accuracy of the equations obtained. The higher-order (fourth to sixth) polynomials investigated did not necessarily improve the accuracy of the resultant availabilities calculated. This is due to repetitive CDF values traceable to the approximation of the visibility data measured to just one decimal place. Therefore, the CDFs of the minimum required visibilities used in our computations is presented as:

$$F\left[V_{\min}\right] = \sum_{j=0}^{3} p_j V_{\min}^{j} \tag{3.22}$$

where p_j are the coefficients of the polynomial.

Tables 3.5(a), 3.5(b), 3.6(a) and 3.6(b) show the polynomial coefficients, error sum of squares (SSE), coefficient of determination (R^2) and the root mean square errors (RMSE) of fitted minimum required visibility CDFs during foggy and clear weather for transmission wavelengths of 850 and 1550 nm. It is clear from all the four tables that the directly calculated and the fitted minimum required visibility CDFs have relatively high R^2, and low SSEs and RMSEs not exceeding 0.1 and 1 metres during foggy and clear weather, respectively. Figures 3.7(a), 3.7(b), 3.8(a) and 3.8(b) show plots of directly evaluated and approximated minimum required visibility CDFs during foggy and clear weather for transmission wavelengths of 850 and 1550 nm. Inserting the values of the coefficients in Tables 3.5(a), 3.5(b), 3.6(a) and 3.6(b) into (3.22) yield plots of the approximated minimum required visibility CDFs in Figures 3.7(a), 3.7(b), 3.8(a) and 3.8(b), respectively.

Table 3.5(a): Polynomial coefficients of fitted minimum required visibility CDFs calculated for major cities in South Africa during foggy weather and at transmission wavelengths of 850 nm

		Coefficients of p_j				Tests		
Location	Range (km)	p_3	p_2	p_1	p_0	SSE	R^2	RMSE
Mbombela	0.04<V<1	5.02×10^{-3}	-8.26×10^{-3}	1.71×10^{-2}	-4.55×10^{-4}	5.17×10^{-6}	0.979	6.86×10^{-4}
Cape Town		9.41×10^{-5}	-4.26×10^{-3}	1.34×10^{-2}	-4.88×10^{-4}	1.06×10^{-6}	0.990	3.10×10^{-4}
Port Elizabeth		-2.16×10^{-3}	4.15×10^{-3}	2.99×10^{-3}	-1.25×10^{-4}	6.23×10^{-7}	0.983	2.38×10^{-4}
Polokwane		6.14×10^{-3}	-9.61×10^{-3}	7.55×10^{-3}	-2.40×10^{-4}	4.04×10^{-7}	0.978	1.92×10^{-4}
Johannesburg		-3.09×10^{-3}	5.85×10^{-3}	5.00×10^{-4}	-2.47×10^{-5}	5.69×10^{-7}	0.967	2.27×10^{-4}
Bloemfontein		-5.70×10^{-4}	6.21×10^{-4}	1.73×10^{-3}	-6.47×10^{-5}	1.09×10^{-7}	0.975	9.96×10^{-5}
Durban		-1.28×10^{-4}	7.71×10^{-4}	-3.26×10^{-5}	1.95×10^{-6}	3.89×10^{-8}	0.937	5.94×10^{-5}
Kimberley		1.78×10^{-4}	8.96×10^{-6}	-3.70×10^{-6}	1.23×10^{-7}	7.01×10^{-9}	0.880	2.52×10^{-5}

Table 3.5(b): Polynomial coefficients of fitted minimum required visibility CDFs calculated for major cities in South Africa during foggy weather and at transmission wavelengths of 1550 nm.

		Coefficients of p_j				Test		
Location	Range (km)	p_3	p_2	p_1	p_0	SSE	R^2	RMSE
Mbombela	0.04<V<1	1.28×10^{-2}	-2.17×10^{-2}	2.31×10^{-2}	-8.42×10^{-4}	6.08×10^{-6}	0.975	7.12×10^{-4}
Cape Town		7.73×10^{-3}	-1.71×10^{-2}	1.89×10^{-2}	-7.04×10^{-4}	1.31×10^{-6}	0.988	3.31×10^{-4}
Port Elizabeth		2.60×10^{-3}	-3.65×10^{-3}	6.19×10^{-3}	-2.24×10^{-4}	1.07×10^{-6}	0.969	2.99×10^{-4}
Polokwane		7.95×10^{-3}	-1.26×10^{-2}	8.82×10^{-3}	-3.08×10^{-4}	4.11×10^{-7}	0.978	1.85×10^{-4}
Johannesburg		-1.93×10^{-3}	4.13×10^{-3}	1.09×10^{-3}	-4.12×10^{-5}	8.71×10^{-7}	0.949	2.69×10^{-4}
Bloemfontein		5.04×10^{-5}	-3.28×10^{-4}	2.07×10^{-3}	-7.29×10^{-5}	1.09×10^{-7}	0.975	9.53×10^{-5}
Durban		1.55×10^{-4}	3.05×10^{-4}	1.66×10^{-4}	-5.39×10^{-6}	3.29×10^{-8}	0.947	5.23×10^{-5}
Kimberley		1.51×10^{-4}	-2.30×10^{-5}	9.91×10^{-7}	-1.26×10^{-8}	3.85×10^{-9}	0.867	1.79×10^{-5}

Table 3.6(a): Polynomial coefficients of fitted minimum required visibility CDFs calculated for major cities in South Africa during clear weather and at transmission wavelengths of 850 nm.

		Coefficients of p_j				Tests		
Location	Range (km)	p_3	p_2	p_1	p_0	SSE	R^2	RMSE
Mbombela		1.82×10^{-4}	-1.53×10^{-3}	1.38×10^{-2}	-1.16×10^{-4}	4.17×10^{-5}	0.995	1.57×10^{-3}
Polokwane		4.49×10^{-4}	-3.32×10^{-3}	8.44×10^{-3}	-7.49×10^{-4}	1.33×10^{-5}	0.993	8.85×10^{-4}
Johannesburg		9.50×10^{-5}	-3.17×10^{-4}	3.02×10^{-3}	-7.48×10^{-5}	6.02×10^{-6}	0.996	5.95×10^{-4}
Durban		9.42×10^{-5}	4.07×10^{-4}	1.21×10^{-4}	-1.26×10^{-5}	5.05×10^{-5}	0.981	1.72×10^{-3}
Cape Town	$0.1<V<7$	2.16×10^{-4}	-2.00×10^{-3}	9.74×10^{-3}	1.69×10^{-4}	1.84×10^{-5}	0.992	1.04×10^{-3}
Port Elizabeth		2.60×10^{-5}	4.73×10^{-5}	4.60×10^{-3}	-2.94×10^{-4}	9.52×10^{-6}	0.996	7.48×10^{-4}
Bloemfontein		3.76×10^{-5}	-2.07×10^{-4}	1.49×10^{-3}	8.86×10^{-5}	2.33×10^{-6}	0.987	3.70×10^{-4}
Mafikeng		3.73×10^{-5}	-2.28×10^{-4}	5.37×10^{-4}	-4.62×10^{-5}	1.61×10^{-7}	0.993	9.73×10^{-5}
Kimberley		1.21×10^{-5}	-1.90×10^{-6}	3.55×10^{-4}	-3.10×10^{-5}	3.55×10^{-7}	0.992	1.44×10^{-4}

Table 3.6(b): Polynomial coefficients of fitted minimum required visibility CDFs calculated for major cities in South Africa during clear weather and at transmission wavelengths of 1550 nm.

		Coefficients of p_j				Tests		
Location	Range (km)	p_3	p_2	p_1	p_0	SSE	R^2	RMSE
Mbombela		2.54×10^{-4}	-1.57×10^{-3}	1.31×10^{-2}	-1.26×10^{-4}	8.15×10^{-5}	0.988	1.97×10^{-3}
Polokwane		5.76×10^{-4}	-3.20×10^{-3}	6.96×10^{-3}	-3.41×10^{-4}	5.64×10^{-5}	0.963	1.64×10^{-3}
Johannesburg		2.55×10^{-4}	-1.29×10^{-3}	4.35×10^{-3}	-2.71×10^{-4}	1.67×10^{-6}	0.998	2.82×10^{-4}
Durban		2.75×10^{-4}	-3.57×10^{-4}	6.18×10^{-4}	-1.42×10^{-5}	4.08×10^{-5}	0.977	1.39×10^{-3}
Cape Town	$0.1<V<6$	2.75×10^{-4}	-2.35×10^{-3}	1.03×10^{-2}	-8.51×10^{-5}	1.76×10^{-5}	0.989	9.17×10^{-4}
Port Elizabeth		1.97×10^{-4}	-9.32×10^{-4}	5.76×10^{-3}	-3.34×10^{-4}	2.61×10^{-6}	0.999	3.53×10^{-4}
Bloemfontein		1.71×10^{-4}	-1.09×10^{-3}	2.88×10^{-3}	-1.78×10^{-4}	5.50×10^{-7}	0.996	1.62×10^{-4}
Mafikeng		5.30×10^{-5}	-2.77×10^{-4}	5.28×10^{-4}	-3.09×10^{-5}	2.15×10^{-7}	0.982	1.01×10^{-4}
Kimberley		2.52×10^{-6}	1.24×10^{-4}	6.99×10^{-5}	-8.08×10^{-6}	1.43×10^{-7}	0.995	8.26×10^{-5}

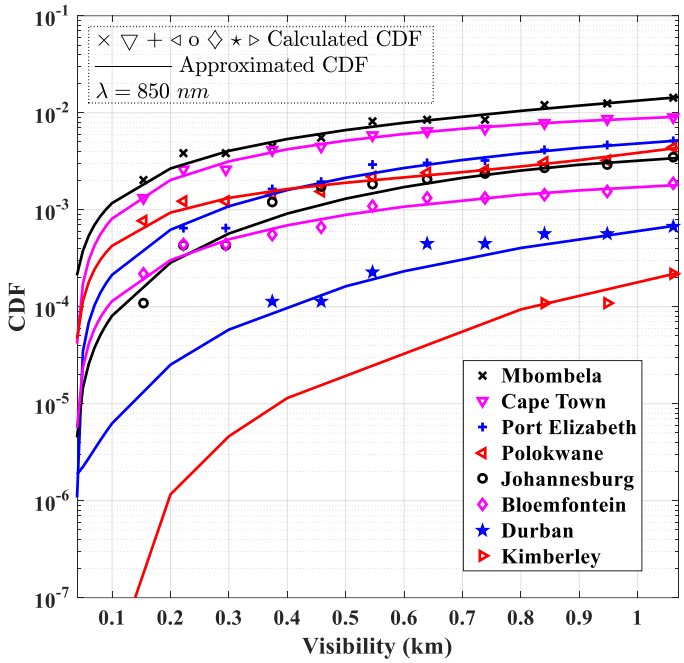

(a) 850 nm

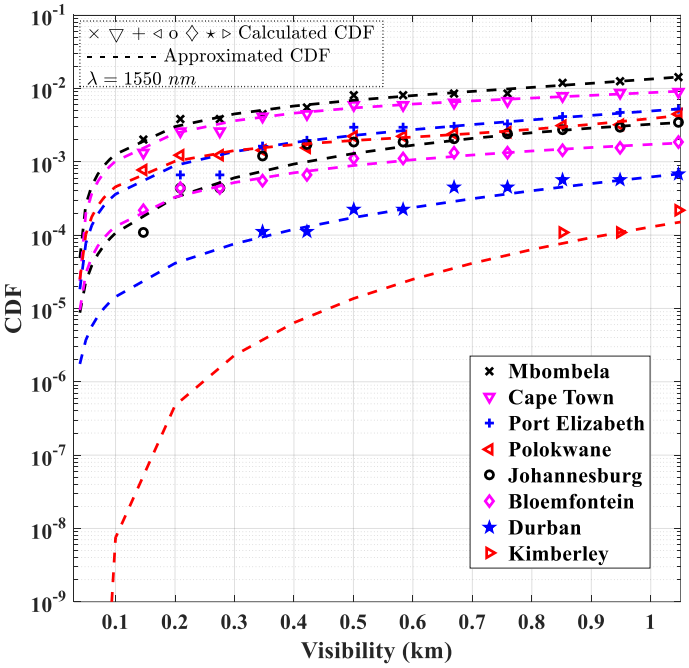

(b) 1550 nm

Figure 3.7: Directly evaluated CDF and approximated CDF of fog for major cities in South Africa using Ijaz model for (a) 850 nm and (b) 1550 nm.

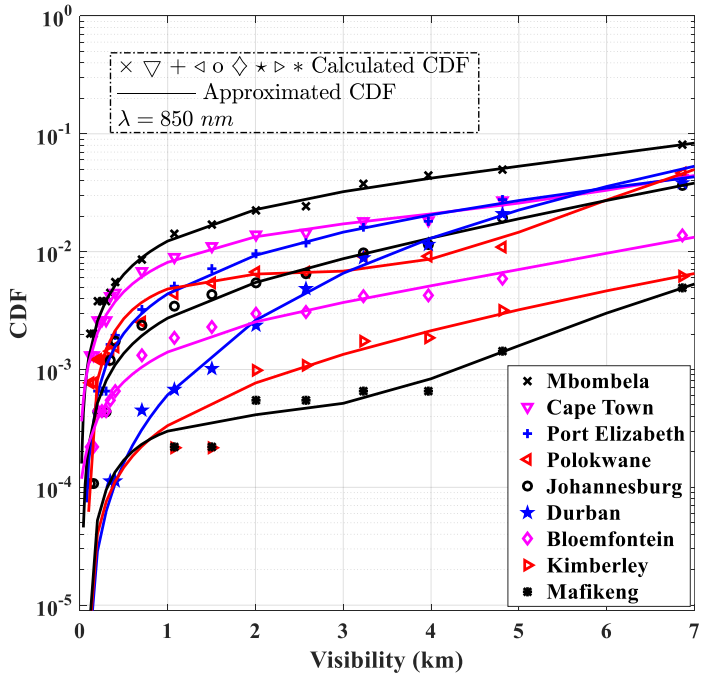

(a) 850 nm

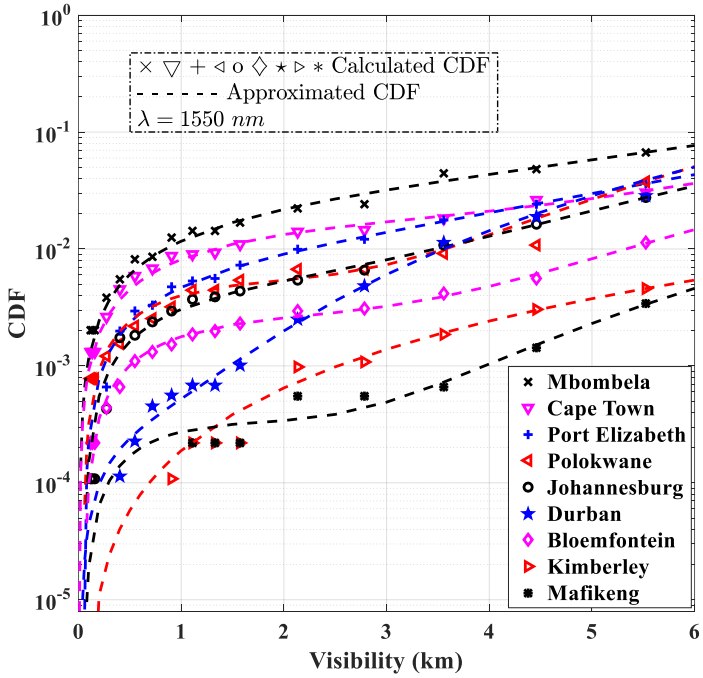

(b) 1550 nm

Figure 3.8: Directly evaluated CDF and approximated CDF of minimum visibility for major cities in South Africa using Kim model for (a) 850 nm and (b) 1550 nm.

Figures 3.7(a) and (b) are based on the Ijaz fog model while Figures 3.8(a) and (b) are calculated using the Kim model for both transmission wavelengths considered in this work. In Figures 3.7(a) and 3.7(b), minimum visibility CDFs under fog conditions are presented. The plot for the city of Mafikeng is not shown because there were no fog events recorded in the data received from the SAWS over the time period investigated. In Figures 3.8(a) and 3.8(b), minimum required visibility CDFs under fog and haze conditions are shown. All the four Figures 3.7(a), 3.7(b), 3.8(a) and 3.8(b) show a high occurrence of minimum visibility under fog/haze conditions in the cities of Mbombela, Cape Town and Port Elizabeth for both transmission wavelengths considered. This clearly indicates that the FSO links in those cities will experience more scattering attenuation during data transmission and ultimately lower link availabilities as compared with the FSO links in the cities of Mafikeng and Kimberley which have very low occurrence of poor visibility events.

3.7 Link Availability

The FSO link availability is majorly dependent on the atmospheric attenuation conditions. The availability of the two commercial FSO links based on the Ijaz and Kim models in this work is defined as ([16], [18], [19], [30], 32]):

$$L_{Av} = \Pr obability\left[V \geq V_{\min}(L)\right] = 1 - F\left[V_{\min}(L)\right] \tag{3.23}$$

Figures 3.9(a), 3.9(b), 3.10(a) and 3.10(b) show the directly evaluated link availabilities alongside the availabilities based on the calculations of approximated minimum required visibility CDFs during foggy and clear weather conditions in different cities of South Africa. It is quite evident from the four figures that Mafikeng, Kimberley and Durban have link availabilities of almost 100% over all the propagation distances considered. This is because of the relatively high visibility measurements as well as the rare occurrence of fog events in those places as shown in Table 3.3. Relatively low availability performance is seen in Port Elizabeth, Cape Town and Mbombela due to unstable weather conditions and relatively high occurrence of fog events in those locations. The link availability reduces with increase in the propagation distance between the two FSO transceivers. In comparison with the 850 nm wavelength, optical signals transmitted at 1550 nm have better availability performance over specific propagation distance in all the cities investigated.

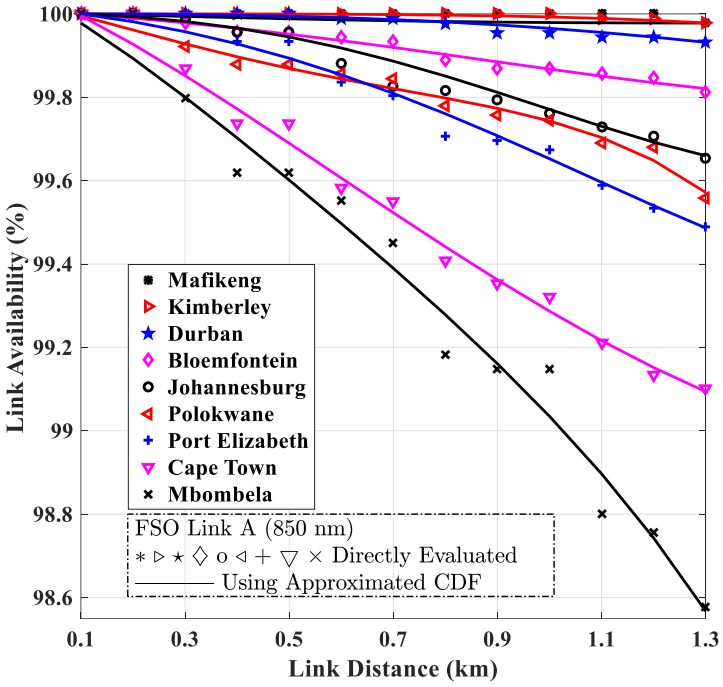

(a) 850 nm

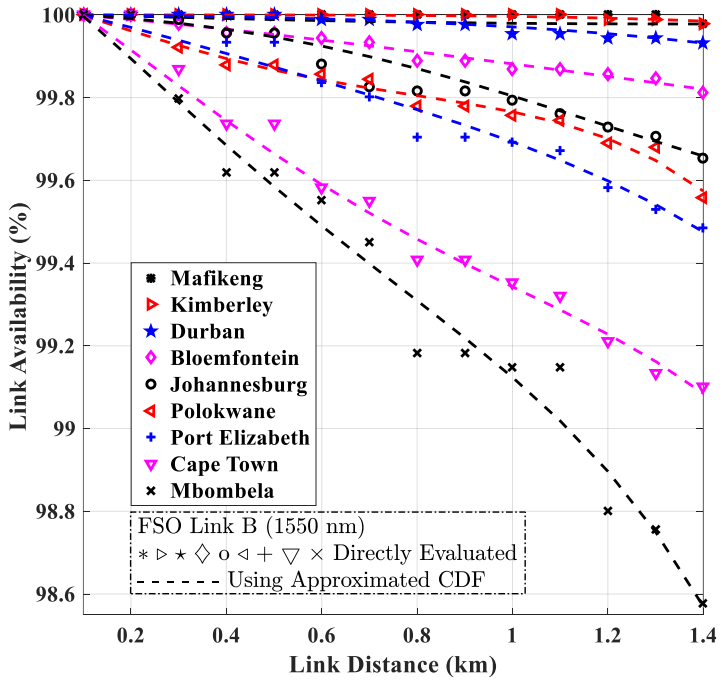

(b) 1550 nm

Figure 3.9: Link availability for commercial FSO links for various cities in South Africa during foggy periods using Ijaz's model for (a) 850 nm and (b) 1550 nm.

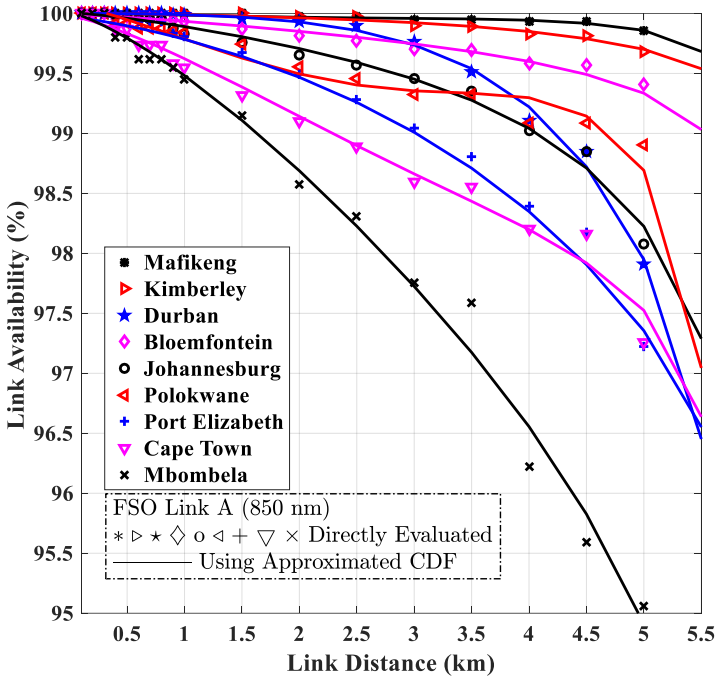

(a) 850 nm

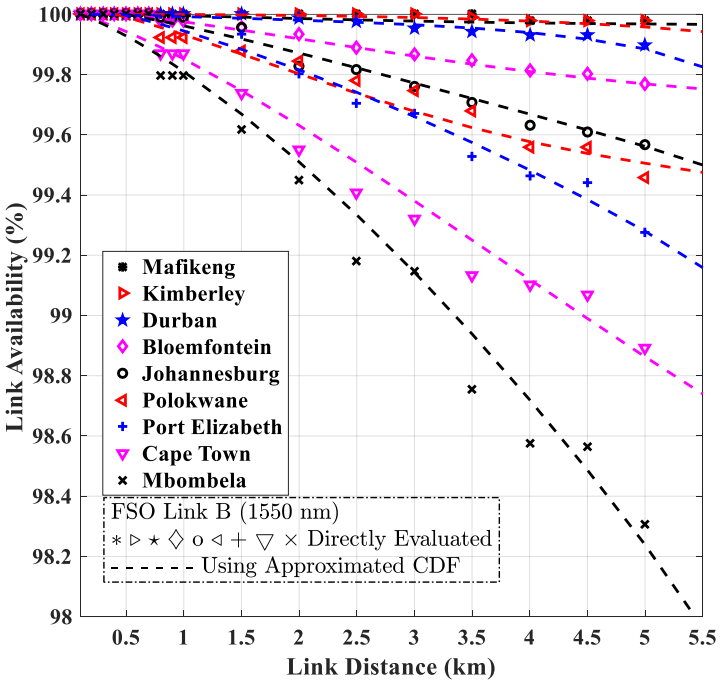

(b) 1550 nm

Figure 3.10: Link availability based on the Kim model for commercial FSO links during clear weather conditions for various cities in South Africa for (a) 850 nm and (b) 1550 nm.

3.8 Signal to noise ratio (SNR), Bit Error Rate (BER) and Data Rate Estimation

Regardless of the length of propagation distance, the optical signal still suffers from random amplitude fluctuations, or scintillation effect, when it passes through the free-space channel. This is due to atmospheric turbulence which is mostly caused by small-scale temperature changes in the atmosphere, which induce variations in the refractive index. As a result of the amplitude fluctuations in the received signal, the BER increases, thus degrading the performance of the system [34]. The lognormal distribution is generally preferred in characterizing the received intensity, *I*, in a weak turbulence regime. Foggy weather is usually accompanied with weak turbulence as fog does not occur under direct sunshine [35]. The probability distribution function (PDF) of a lognormal variable *I* with small variance is given in [36] as:

$$p(I) = \frac{1}{I\sqrt{2\pi\sigma_{SI}^2}} \exp\left\{ -\left(\frac{In(I) + \frac{\sigma_{SI}^2}{2}}{\sqrt{2\sigma_{SI}^2}} \right)^2 \right\} \tag{3.24}$$

where σ_{SI}^2 is the scintillation index parameter that indicates the amount of scintillation in the atmosphere. Based on the zero inner scale model, the scintillation index is expressed in [37]-[38] as:

$$\sigma_{SI}^2 = \exp\left[\frac{0.49\sigma_{sw}^2}{\left(1 + 0.18d_s^2 + 0.56\sigma_{sw}^{12/5}\right)^{7/6}} + \frac{0.51\sigma_{sw}^2\left(1 + 0.69\sigma_{sw}^{12/5}\right)^{-5/6}}{1 + 0.90d_s^2 + 0.62d_s^2\sigma_{sw}^{12/5}} \right] - 1 \tag{3.25}$$

where $\sigma_{sw}^2 = 0.50C_n^2\left(\sqrt[6]{k^7L^{11}}\right)$ is the Rytov variance for the spherical wave, $d_s = \sqrt{\frac{kD^2}{4L}}$, C_n^2 is the refractive index structure parameter in $m^{-2/3}$, and $k = \frac{2\pi}{\lambda}$ is the wave number in m^{-1}. In weak turbulence conditions, σ_{SI}^2 is less than unity [37]. For optical spherical waves, the scintillation indices of all the locations considered in South Africa based on the average parameters shown in Table 3.7 were also less than unity [33].

Most commercial FSO links on the market are still using intensity modulation/direct detection (IM/DD) schemes for operation. The performance of non-return-to-zero on-off keying (NRZ-OOK) modulation scheme and avalanche photodiode (APD) FSO systems are investigated in this section. The total APD receiver noise mainly consists of the shot noise σ_{Sh}^2, and thermal noise σ_{Th}^2. It is expressed in [39] as:

$$\sigma_N^2 = \sigma_{Th}^2 + \sigma_{Sh}^2 \tag{3.26}$$

Thermal noise arises as a result of current fluctuation caused by the thermal motion of electrons at some finite temperature, even when there is no signal transmission. It is given in [40] as:

$$\sigma_{Th}^2 = \frac{2TK_BR_bF_n}{R} \tag{3.27}$$

where T is the receiver temperature, K_B is the Boltzmann constant, R_b is the bit rate, F_n is the amplifier noise figure and R is the APD load resistance. The shot noise is also denoted in [40] as:

$$\sigma_{Sh}^2 = 2qg^2\Re F_A R_b P_{Rx} I + \sigma_{Th}^2 \tag{3.28}$$

where q is the charge of an electron, g is the APD gain, $\Re$ is the responsivity, P_{Rx} is the power of the received signal and F_A is the excess noise factor. F_A is expressed as:

$$F_A = k_A g + (1 - k_A)\left(2 - g^{-1}\right) \tag{3.29}$$

where k_A is the ionization factor.

The instantaneous SNR (γ_o) at the receiver is given as:

$$\gamma_o = \frac{\left(2g\Re P_{Rx} I\right)^2}{\sigma_N^2} \tag{3.30}$$

The conditional BER of the FSO communication system employing IM/DD and based on the NRZ-OOK modulation scheme is given by [41]:

$$BER = \frac{1}{2} erfc\left(\frac{\sqrt{\gamma_o}}{2\sqrt{2}}\right) = Q\left(\frac{\sqrt{\gamma_o}}{2}\right) \tag{3.31}$$

Substituting (3.30) into (3.31), yields:

$$BER = \frac{1}{2} erfc\left(\frac{2g\Re P_{Rx} I}{2\sqrt{2}\left(\sqrt{\sigma_N^2}\right)}\right) \tag{3.32}$$

Equation (3.32) represents the conditional BER in a turbulence-free channel. Taking into account the effect of weak atmospheric turbulence on (3.32), the average BER over the lognormal fading channel is obtained by averaging (3.31) over (3.24):

$$BER = \int_0^\infty Q\left(\frac{\sqrt{\gamma_o}}{2}\right).p(I)\,dI \tag{3.33}$$

Employing the change of variable, z, we have:

$$z = \frac{In(I) + \frac{\sigma_{SI}^2}{2}}{\sqrt{2\sigma_{SI}^2}} \tag{3.34}$$

Making I the subject of (3.34), we obtain:

$$I = \exp\left(z\sqrt{2\sigma_{SI}^2} - \frac{\sigma_{SI}^2}{2}\right) \tag{3.35}$$

Differentiating I with respect to z, we have:

$$dI = \sqrt{2\sigma_{SI}^2}\exp\left(z\sqrt{2\sigma_{SI}^2} - \frac{\sigma_{SI}^2}{2}\right)dz \tag{3.36}$$

Substituting (3.24), (3.34), (3.35) and (3.36) into (3.33), we obtain:

$$BER = \frac{1}{\sqrt{\pi}}\int_0^{\infty} Q\left(\frac{\sqrt{\gamma_o}}{2}\right)\exp\left(-z^2\right)dz \tag{3.37}$$

Further substitution of (3.27), (3.28), (3.30), (3.32) and (3.35) into (3.37) yields:

$$BER = \frac{1}{2\sqrt{\pi}} \bullet \int_0^{\infty} erfc\left(\frac{2g\Re P_{Rx}.\exp\left(z\sqrt{2\sigma_{SI}^2} - \frac{\sigma_{SI}^2}{2}\right)}{2\sqrt{2}} \bullet \frac{1}{\left(\sqrt{\sigma_{Th}^2} + \sqrt{2qg^2\Re F_A R_b P_{Rx}.\exp\left(z\sqrt{2\sigma_{SI}^2} - \frac{\sigma_{SI}^2}{2}\right) + \sigma_{Th}^2}\right)}\right) \tag{3.38}$$

$$\bullet \exp\left(-z^2\right)dz$$

Equation (3.38) can be evaluated using the Gauss-Hermite approximation as presented in [42]-[43] as:

$$\int_{-\infty}^{\infty}\exp\left(-x^2\right)f\left(x\right)dx \cong \sum_{i=1}^{n} w_i f\left(z_i\right) \tag{3.39}$$

where

$$f\left(z\right) = erfc\left(\frac{g\Re P_{Rx}.\exp\left(z\sqrt{2\sigma_{SI}^2} - \frac{\sigma_{SI}^2}{2}\right)}{\sqrt{2}} \bullet \frac{1}{\left(\sqrt{\sigma_{Th}^2} + \sqrt{2qg^2\Re F_A R_b P_{Rx}.\exp\left(z\sqrt{2\sigma_{SI}^2} - \frac{\sigma_{SI}^2}{2}\right) + \sigma_{Th}^2}\right)}\right) \tag{3.40}$$

Equation (3.39) thus becomes:

$$BER \cong \frac{1}{2\sqrt{\pi}}\sum_{i=1}^{n} w_i \bullet \left(erfc\left(\frac{g\Re P_{Rx}.\exp\left(z\sqrt{2\sigma_{SI}^2} - \frac{\sigma_{SI}^2}{2}\right)}{\sqrt{2}} \bullet \frac{1}{\left(\sqrt{\sigma_{Th}^2} + \sqrt{2qg^2\Re F_A R_b P_{Rx}.\exp\left(z\sqrt{2\sigma_{SI}^2} - \frac{\sigma_{SI}^2}{2}\right) + \sigma_{Th}^2}\right)}\right)\right) \tag{3.41}$$

where the values of the weights, w_i and zeros of the Hermite polynomial, z_i, are given in [42]-[43].

The achievable data rate, R_D, of an FSO link is given in [44] as:

$$R_D = \frac{P_{Tx}\tau_{Tx}\tau_{Rx}A_{Rx}}{\pi(0.5\theta)^2 L^2 E_p N_b A_\alpha F_{SL} L_{Geo}} \tag{3.42}$$

where τ_{Tx} is the transmitter efficiency, τ_{Rx} is the receiver efficiency, A_{Rx} is the area of the receiver lens, N_b is the receiver sensitivity, $E_p = \frac{hc}{\lambda}$ is the energy of the photon, h is Planck's constant and c is the speed of light.

Table 3.7: Wind velocities (ws), altitudes and refractive indexes [33].

City	Average W_s (m/s)	Altitude (m)	Refractive Index Structure Parameter ($m^{-2/3}$)
Kimberley	4.10	1196	2.4629×10^{-13}
Mafikeng	3.96	1281	2.0566×10^{-13}
Johannesburg	4.18	1695	1.9574×10^{-13}
Mbombela	2.82	865	5.5406×10^{-14}
Polokwane	2.82	1226	5.4351×10^{-14}
Bloemfontein	2.45	1354	2.9039×10^{-14}
Port Elizabeth	5.41	69	2.3653×10^{-14}
Durban	3.47	106	8.7979×10^{-15}
Cape Town	5.14	42	7.5257×10^{-15}

The receive SNR for commercial FSO links A and B over link distances for the most frequent fog conditions peculiar to each of the various cities of South Africa are presented in Figures 3.11(a) and (b), respectively. The numerical results are derived from parameters in Tables 3.2, 3.4 and 3.8 as well as (3.26) to (3.30). It is evident from Figures 3.11(a) and (b) that the FSO links in the cities of Cape Town and Johannesburg will have the lowest link performance due to the occurrence of thick fog events. For a receive SNR of 20 dB, both links have the least propagation distance of about 600 – 680 metres with FSO link B slightly out-performing the FSO link A due to their transmission wavelength. FSO links in the city of Mafikeng have improved performance due to the occurrence of only very light fog weather as compared with other cities in South Africa. Figures 3.12(a) and (b) show the SNRs needed to achieve certain BERs for single-input single-output (SISO) FSO links A and B in various cities of South Africa. The numerical results are calculated from parameters in (3.41) and Tables 3.2, 3.4, 3.7, and 3.8. The FSO links in the cities of Mafikeng and Kimberley require more power to achieve lower BERs than other cities in South Africa. In Figure 3.12(a), to achieve a BER of 10^{-4}, the FSO links in Mafikeng and Kimberley require an SNR of ~48.5 dB while the links in other cities require less than 48 dB to achieve the same BER. A similar performance is seen in Figure 3.12(b).

Table 3.8: FSO link parameters for SNR, BER and data rate

Parameter	Values
Light Source	Laser
Boltzmann's constant (K_B)	1.381×10^{-23} J/K
Temperature (T)	298 K
Transmitter efficiency (τ_{Tx})	80 %
Receiver efficiency (τ_{Rx})	80 %
Planck's constant (h)	6.626×10^{-34} Js
Speed of light (c)	3×10^{8} m/s
Detector	Avalanche Photodiode (APD)
APD Load Resistance (R)	1000 Ω
APD gain (g)	50
Amplifier noise figure (F_n)	2
Charge of an electron (q)	1.6022×10^{-19} C
Ionization factor for (InGaAs APD) (k_A)	0.7

The poorer BER performances of FSO links in Mafikeng and Kimberley are caused by high wind speeds, refractive indexes and altitudes as compared with other cities of South Africa. This is highlighted in Table 3.7 as shown in [33]. Figures 3.13(a) and (b) show the BER performance of FSO links over propagation distances in the various cities of South Africa. Of all the propagation path lengths considered, the FSO links in Mafikeng and Mbombela have better performances than those in the other cities considered. In Figure 3.13(a), a BER of 10^{-4} is achieved over a link distance of 760 metres in Mafikeng, while the same BER can only be achieved over a path length of 415 metres in Cape Town. Similarly, to obtain a BER of 10^{-6} in Figure 3.13(b), link distances of not more than 580 metres and 370 metres will attain the BER performance in Mafikeng and Cape Town, respectively.

The highest data rates over link distances that can be achieved by FSO systems under foggy weather conditions in various cities of South Africa are shown in Figures 3.14(a) and (b). These numerical results are calculated from (3.42) and parameters in Tables 3.2, 3.4 and 3.8. FSO links transmitting at 1550 nm achieve higher data rates than the 850 nm links. It is evident from both figures that the aerosol scattering attenuation due to fog greatly impacts data transmission rates. The FSO links in Johannesburg and Cape Town have the lowest data rates performance over the link distances considered during their most occurring dense fog event. The cities of Mafikeng, Kimberley and Mbombela have better data transmission rates due to very light fog events that occur in those locations.

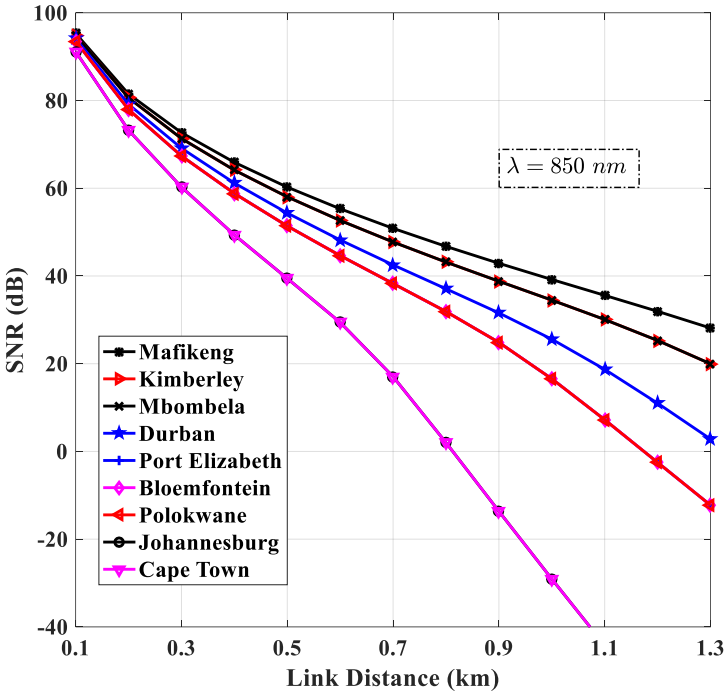

(a) 850 nm

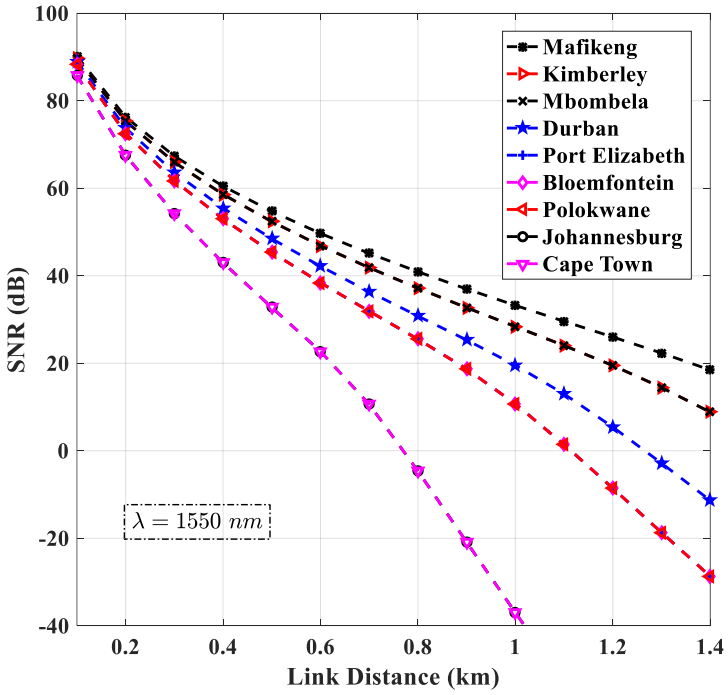

(b) 1550 nm

Figure 3.11: Receive SNR for commercial FSO link for various cities in South Africa during foggy periods for (a) 850 nm and (b) 1550 nm.

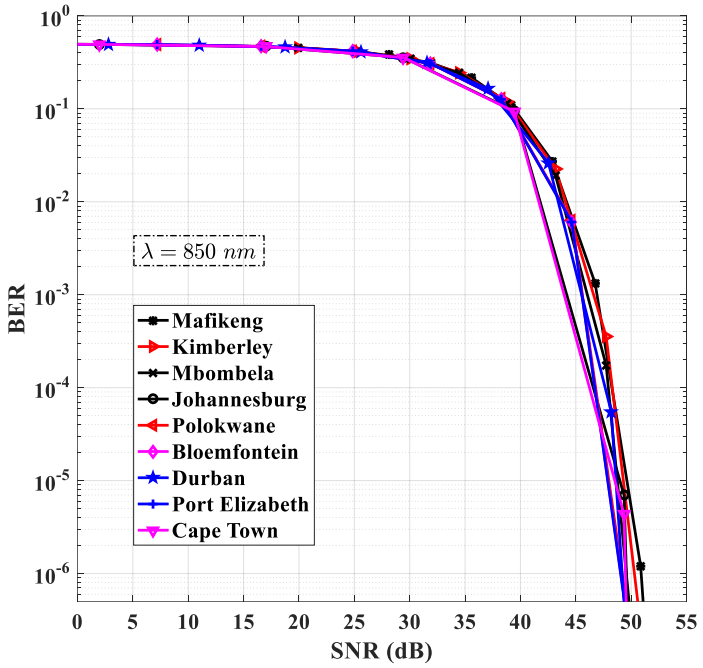

(a) 850 nm

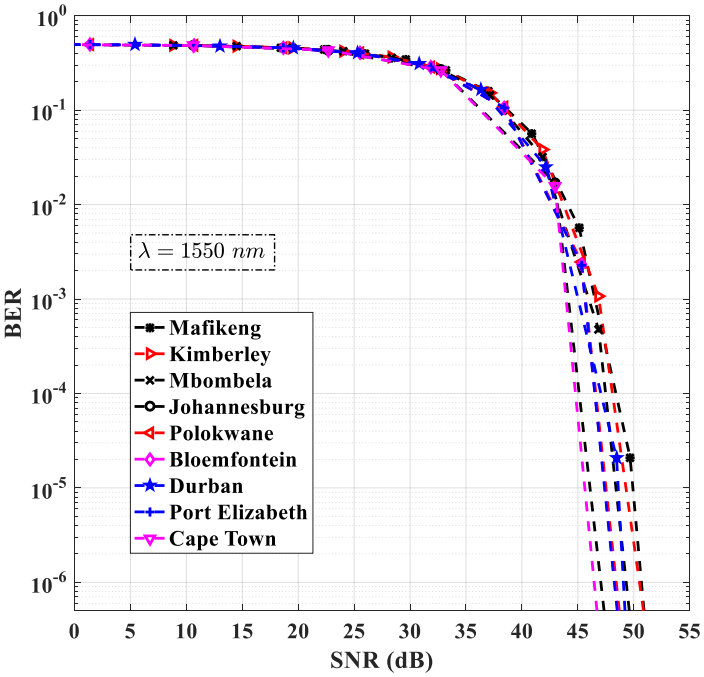

(b) 1550 nm

Figure 3.12: BER of SISO FSO links employing OOK modulation during foggy weather and weak atmospheric turbulence for (a) 850 nm and (b) 1550 nm.

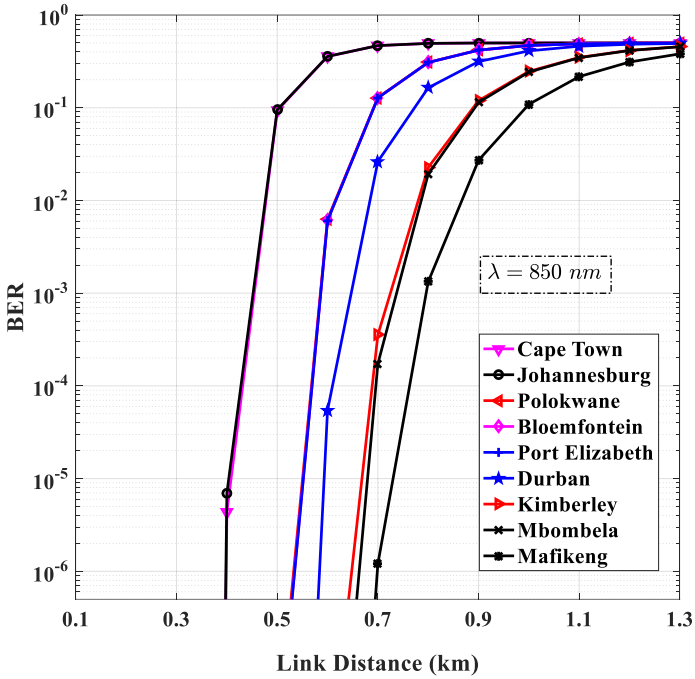

(a) 850 nm

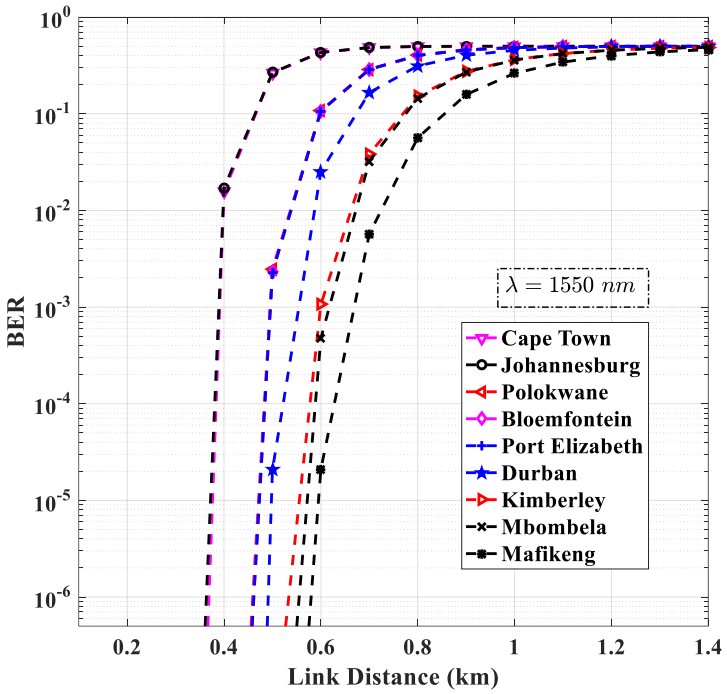

(b) 1550 nm

Figure 3.13: BER performance of SISO FSO links employing OOK modulation over link distances in a foggy and weak turbulence regime for (a) 850 nm and (b) 1550 nm.

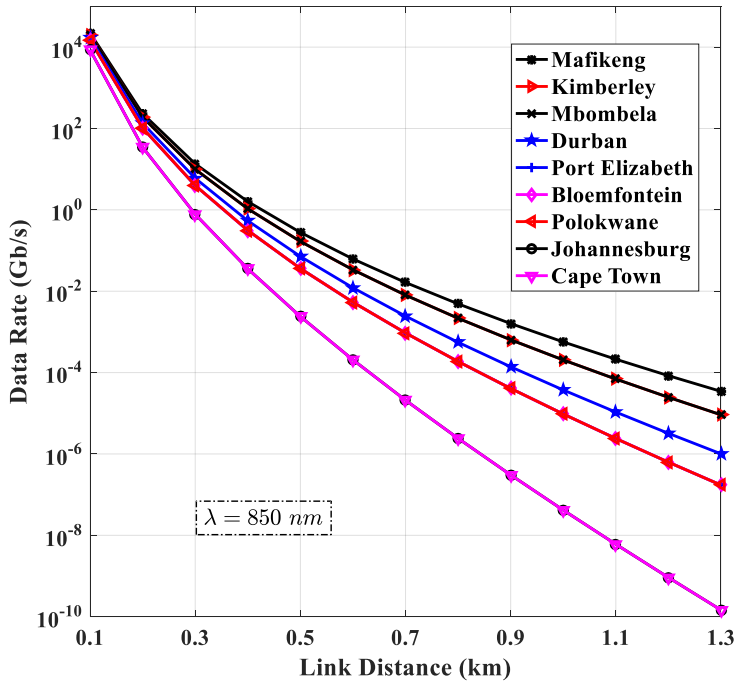

(a) 850 nm

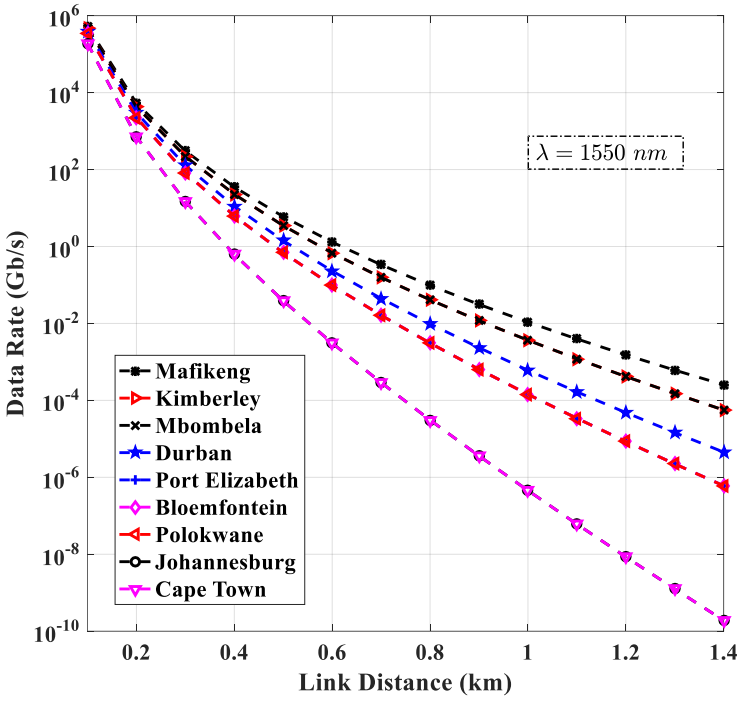

(b) 1550 nm

Figure 3.14: Attainable data rates of horizontal FSO links over link distances under foggy weather conditions for (a) 850 nm and (b) 1550 nm.

3.9 Conclusion

In this paper, availability analysis of terrestrial FSO communication links based on the climatic peculiarities of various cities in South Africa are presented. Cumulative distributions of aerosol scattering attenuation based on Kim and Ijaz models were carried out using visibility data for the locations of interest. Probabilities of exceedance, deceedance and encountering of scattering attenuation is shown. Link budget analysis for two FSO links transmitting at two wavelengths were carried out. The resultant link margin equations derived were implemented in evaluating minimum required visibilities for two links in foggy and clear weather conditions. Approximate polynomial equations for calculating the minimum required visibilities for all the cities considered are derived, and then applied in estimating link availabilities of two commercial FSO links. Plots of the receive SNR and data rate performance in foggy weather conditions are presented. BER and link performance plots are presented for two links in the presence of weak atmospheric turbulence based on average weather parameters of several cities of South Africa. The FSO system transmitting at 1550 nm is seen to outperform the one transmitting at 850 nm based on all the performance metrics used. This work may be extended in future by investigating different localized climatic constraints on the various types of optical signals such as plane, spherical and Gaussian beam waves. This would aid in the modeling of different types of attenuations for locations of interest where FSO or hybrid FSO systems are to be deployed.

References

[1] S. Chauhan, R. Miglani, L. Kansal, G. S. Gaba, and M. Masud, "Performance Analysis and Enhancement of Free Space Optical Links for Developing State-of-the-Art Smart City Framework," *Photonics*, vol. 7, no. 4, p. 132, Dec. 2020, DOI: 10.3390/photonics7040132.

[2] M. Fuentes, J. L. Carcel, C. Dietrich, L. Yu, E. Garro, V. Pauli, *et al.*, "5G new radio evaluation against IMT-2020 key performance indicators," *IEEE Access*, vol. 8, pp. 110880-110896, 2020, DOI: 10.1109/ACCESS.2020.3001641.

[3] J. Kim, J. Song, W. Seo, I. Ihm, S.-H. Yoon, and S. Park, "XR Framework for Collaborating Remote Heterogeneous Devices," *2020 IEEE Conference on Virtual Reality and 3D User Interfaces Abstracts and Workshops (VRW)*, 2020, pp. 587-588, DOI: 10.1109/VRW50115.2020.00144.

[4] S. Böcker, C. Arendt, P. Jörke, and C. Wietfeld, "LPWAN in the Context of 5G: Capability of LoRaWAN to Contribute to mMTC," *2019 IEEE 5th World Forum on Internet of Things (WF-IoT)*, 2019, pp. 737-742, DOI: 10.1109/WF-IoT.2019.8767333.

[5] M. Garlinska, A. Pregowska, K. Masztalerz, and M. Osial, "From Mirrors to Free-Space Optical Communication—Historical Aspects in Data Transmission," *Future Internet*, vol. 12, no. 11, p. 179, Oct. 2020, DOI: 10.3390/fi12110179.

[6] B. Bag, A. Das, I. S. Ansari, A. Prokeš, C. Bose, and A. Chandra, "Performance analysis of hybrid FSO systems using FSO/RF-FSO link adaptation," *IEEE Photonics Journal*, vol. 10, no. 3, pp. 1-17, June 2018, DOI: 10.1109/JPHOT.2018.2837356.

[7] S. Malik and P. K. Sahu, "Free space optics/millimeter-wave based vertical and horizontal terrestrial backhaul network for 5G," *Optics Communications*, vol. 459, p. 125010, Mar. 2020, DOI: 10.1016/j.optcom.2019.125010.

[8] C. J. Engelbrecht and F. A. Engelbrecht, "Shifts in Köppen-Geiger climate zones over southern Africa in relation to key global temperature goals," *Theoretical and applied climatology*, vol. 123, pp. 247-261, 2016, DOI: 10.1007/s00704-014-1354-1.

[9] P. D. Tyson and R. A. Preston-Whyte, "Atmospheric circulation and weather over southern africa," in *Weather and climate of southern Africa*, 2nd ed. Cape Town, South Africa: Oxford University Press Southern Africa, 2000, ch. 12, pp. 176-217.

[10] M. O. Odedina, "A semi-empirical formulation for determination of rain attenuation on terrestrial radio links," Ph.D. dissertation, Sch. Elect. Electron. Comp. Eng., Univ. KwaZulu-Natal, Durban, South Africa, 2010.

[11] P. A. Owolawi, "Characteristics of rain at microwave and millimetric bands for terrestrial and satellite links attenuation in South Africa and surrounding islands," Ph.D. dissertation, Sch. Elect. Electron. Comp. Eng., Univ. KwaZulu-Natal, Durban, South Africa, 2010.

[12] M. Tadross and P. Johnston, , "Climate systems regional report: Southern Africa," ICLEI–Local Governments for Sustainability–Africa, Cape Town, South Africa, 105868-001, Aug. 2012, [Online]. Available: https://idl-bnc-idrc.dspacedirect.org/bitstream/handle/10625/50398/IDL-50398.pdf?sequence=1&isAllowed=y.

[13] O. O. Kolawole, M. Mosalaosi, and T. J. Afullo, "Visibility modeling and prediction for free space optical communication systems for South Africa," *International Journal on Communications Antenna and Propagation*, vol. 10, no. 3, pp. 161-174, 2020, DOI: 10.15866/irecap.v10i3.18008.

[14] K. Dev, R. Nebuloni, and C. Capsoni, "Optical attenuation measurements in low visibility conditions," *2016 10th European Conference on Antennas and Propagation (EuCAP)*, 2016, pp. 1-5, DOI: 10.1109/EuCAP.2016.7481270.

[15] V. Kvicera, M. Grabner, and J. Vasicek, "Assessing availability performances of free space optical links from airport visibility data," *2010 7th International Symposium on Communication Systems, Networks & Digital Signal Processing (CSNDSP 2010)*, 2010, pp. 562-565, DOI: 10.1109/CSNDSP16145.2010.5580372.

[16] O. Kolawole, T. Afullo, and M. Mosalaosi, "Estimation of Optical Wireless Communication Link Availability Using Meteorological Visibility Data for Major Locations in South Africa," *2019 PhotonIcs & Electromagnetics Research Symposium-Spring (PIERS-Spring)*, 2019, pp. 319-325, DOI: 10.1109/PIERS-Spring46901.2019.9017842.

[17] M. M. Shumani, M. Abdullah, and A. Basahel, "Availability analysis of terrestrial free space optical (FSO) link using visibility data measured in tropical region," *Optik*, vol. 158, pp. 105-111, April 2018, DOI: 10.1016/j.ijleo.2017.11.203.

[18] O. O. Kolawole, "Performance analysis of optical wireless communication systems in a warm-summer Mediterranean climatic region," M.S. thesis, Sch. Elect. Electron. Comp. Eng., Univ. KwaZulu-Natal, Durban, South Africa, 2017.

[19] J. Mohale, M. R. Handura, T. O. Olwal, and C. N. Nyirenda, "Feasibility study of free-space optical communication for South Africa," *Optical Engineering*, vol. 55, no. 5, p. 056108, May 2016, DOI: 10.1117/1.OE.55.5.056108.

[20] P. Anokye, "Free space optical communication over the Ghanaian Turbulent Atmospheric Channel," M.S. thesis, Dept. Elect. Electron. Eng., Kwame Nkrumah Univ. Sci. Tech., Kumasi, Ghana, 2014.

[21] I. I. Kim, B. McArthur, and E. J. Korevaar, "Comparison of laser beam propagation at 785 nm and 1550 nm in fog and haze for optical wireless communications," in *Proc. SPIE 4214, Optical Wireless Communications III*, Feb. 2001, pp. 26-37, DOI: 10.1117/12.417512.

[22] M. Ijaz, "Experimental characterisation and modelling of atmospheric fog and turbulence in FSO," Ph.D. dissertation, Faculty Eng. Env., Northumbria University, Newcastle upon Tyne, UK, 2013.

[23] M. Ijaz, Z. Ghassemlooy, J. Pesek, O. Fiser, H. Le Minh, and E. Bentley, "Modeling of fog and smoke attenuation in free space optical communications link under controlled laboratory conditions," *Journal of Lightwave Technology,* vol. 31, no. 11, pp. 1720-1726, June 2013, DOI: 10.1109/JLT.2013.2257683.

[24] M. S. Awan, L. Csurgai-Horváth, S. S. Muhammad, E. Leitgeb, F. Nadeem, and M. S. Khan, "Characterization of Fog and Snow Attenuations for Free-Space Optical Propagation," *Journal of Communications,* vol. 4, no. 8, pp. 533-545, Sept. 2009, DOI: 10.4304/jcm.4.8.533-545.

[25] International Telecommunication Union, "Calculation of free-space attenuation," Recommendation ITU-R P.525-4, Aug. 22, 2019. [Online] Available: https://www.itu.int/dms_pubrec/itu-r/rec/p/R-REC-P.525-4-201908-I!!PDF-E.pdf

[26] Z. Ghassemlooy, W. Popoola, and S. Rajbhandari, "Channel Modelling," in *Optical wireless communications: system and channel modelling with Matlab®*, 2nd ed. Boca Raton, FL, USA: CRC press, 2019, ch. 3, pp. 115-119.

[27] H. Henniger and O. Wilfert, "An Introduction to Free-space Optical Communications," *Radioengineering,* vol. 19, no. 2, pp. 203-212, June 2010. [Online] Available: https://www.radioeng.cz/fulltexts/2010/10_02_203_212.pdf

[28] W. O. Popoola, "Subcarrier intensity modulated free-space optical communication systems," Ph.D. dissertation, Faculty Eng. Env., Northumbria University, Newcastle upon Tyne, UK, 2009.

[29] A. Basahel, M. R. Islam, M. H. Habaebi, and S. Ahmad, "Availability prediction methods for terrestrial free-space-optical link under tropical climate," *Indonesian Journal of Electrical Engineering and Computer Science (IJEECS)*, vol. 10, no. 1, pp. 224-229, April 2018, DOI: 10.11591/ijeecs.v10.i1.

[30] A. Prokes, "Atmospheric effects on availability of free space optics systems," *Optical Engineering,* vol. 48, no. 6, p. 066001, June 2009. DOI: 10.1117/1.3155431

[31] M. Handura, K. Ndjavera, C. Nyirenda, and T. Olwal, "Determining the feasibility of free space optical communication in Namibia," *Optics Communications,* vol. 366, pp. 425-430, May 2016, DOI: 10.1016/j.optcom.2015.12.057.

[32] A. Prokes and V. Skorpil, "Estimation of free space optics systems availability based on meteorological visibility," in *2009 IEEE Latin-American Conference on Communications*, 2009, pp. 1-4, DOI: 10.1109/LATINCOM.2009.5305266.

[33] O. O. Kolawole, T. J. Afullo, and M. Mosalaosi, "Initial Estimation of Scintillation Effect on Free Space Optical Links in South Africa," in *2019 IEEE AFRICON*, 2019, pp. 1-6, DOI: 10.1109/AFRICON46755.2019.9134032.

[34] D. A. Luong, T. C. Thang, and A. T. Pham, "Effect of avalanche photodiode and thermal noises on the performance of binary phase-shift keying-subcarrier-intensity modulation/free-space optical systems over turbulence channels," *IET Communications*, vol. 7, no. 8, pp. 738-744, May 2013, DOI: 10.1049/iet-com.2012.0600.

[35] M. Abaza, R. Mesleh, and A. Mansour, "Performance analysis of MISO multi-hop FSO links over log-normal channels with fog and beam divergence attenuations," *Optics Communications*, vol. 334, pp. 247-252, Jan. 2015, DOI: 10.1016/j.optcom.2014.08.050.

[36] A. Prokeš, "Modeling of atmospheric turbulence effect on terrestrial FSO link," *Radioengineering*, vol. 18, no. 1, pp. 42-47, April 2009. [Online] Available: https://www.radioeng.cz/fulltexts/2009/09_01_042_047.pdf

[37] L. C. Andrews, R. L. Phillips, and C. Y. Hopen, *Laser beam scintillation with applications*, vol. 99, SPIE press, Bellingham, Washington, USA, 2001.

[38] A. Prokes and L. Brancik, "Degradation of free space optical communication performance caused by atmospheric turbulence," in *2012 2nd International Conference on Advances in Computational Tools for Engineering Applications (ACTEA)*, 2012, pp. 338-341, DOI: 10.1109/ICTEA.2012.6462896.

[39] H. Akbar and Iskandar, "BER performance analysis of APD-based FSO system for optical inter-HAPS link," in *2015 1st International Conference on Wireless and Telematics (ICWT)*, 2015, pp. 1-5, DOI: 10.1109/ICWT.2015.7449232.

[40] M. I. Petković, G. T. Đorđević, and D. N. Milić, "BER performance of IM/DD FSO system with OOK using APD receiver," *Radioengineering*, vol. 23, no. 1, pp. 480-487, April 2014. [Online] Available: https://www.radioeng.cz/fulltexts/2014/14_01_0480_0487.pdf

[41] M. Bouhadda, F. M. Abbou, M. Serhani, F. Chaatit, and A. Boutoulout, "Analysis of dispersion effect on a NRZ-OOK terrestrial free-space optical transmission system," *Journal of the European Optical Society-Rapid Publications*, vol. 12, no. 18, pp. 1-6, Oct. 2016, DOI: 10.1186/s41476-016-0020-x.

[42] M. Abramowitz and I. A. Stegun, *Handbook of mathematical functions with formulas, graphs, and mathematical tables* vol. 55: US Government printing office, 1964.

[43] F. Scheid, *Schaum's outline of theory and problems of numerical analysis*: McGraw-Hill, 1988.

[44] A. K. Majumdar, "Free-space laser communication performance in the atmospheric channel," *Journal of Optical and Fiber Communications Reports*, vol. 2, pp. 345-396, 2005, DOI: 10.1007/s10297-005-0054-0.

Chapter 4

4 Journal Article 3

Analysis of Scintillation Effects on Free Space Optical Communication Links in South Africa

Olabamidele O. Kolawole, Thomas J.O. Afullo, Modisa Mosalaosi

Published: *Photonics (MDPI) Journal*, 2022, vol. 9, no. 7, DOI: 10.3390/photonics9070446

4.1 Abstract

The performance of free space optical communication (FSOC) systems is severely degraded by certain atmospheric conditions prevalent in places where they are deployed, in spite of their numerous advantages. In clear weather conditions, the random fluctuation in the atmosphere's refractive index causes substantial scintillation losses to transmitted optical signals. It is therefore imperative to estimate the potential losses due to atmospheric turbulence in locations where FSOC links are to be deployed. This will provide the necessary fade margin for FSOC systems so that designed links withstand such atmospheric disturbances. In this paper, statistical analysis of wind speed data collected for various cities of South Africa is used for calculating the corresponding refractive index structure parameter (C_n^2). These C_n^2 values, as well as the zero inner scale and infinite outer scale model and finite inner and finite outer scale model, are used in computing the scintillation indices not exceeding 50%, 99%, 99.9%, and 99.99% of the time for the investigated locations. The Lognormal and Gamma–gamma distribution models are then employed for the computational analysis of the irradiance fluctuations and channel characteristics while considering the effect of pointing errors for weak and moderate to strong turbulence regimes. Finally, derived mathematical expressions for outage probabilities and bit error rate (BER) performances for FSOC links, employing various intensity modulation and direct detection (IM/DD) schemes, are presented.

4.2 Introduction

The International Mobile Telecommunications 2020 (IMT-2020) specifications, developed by the third generation partnership project (3GPP) for new radio (NR) operations in the fifth generation (5G) spectrum, is expected to accomplish the following performance requirements: ultra-reliable and low latency communications (URLLC) in the user plane as low as 1 ms; massive machine type communications (mMTC) that supports up to 1 million devices per square km; and enhanced mobile broadband (eMBB) with uplink and downlink speeds of up to 10 and 20 Gbits/s [1], [2]. These technical requirements are needed for the high bandwidth demands of augmented reality (AR), virtual reality (VR), and mixed reality (MR) applications, as well as the seamless and optimal functionality of Massive Internet of Things (MIoT) and Vehicle-to-Everything (V2X) connections for the smooth running of emerging smart cities [3]-[5].

Free space optical communication (FSOC), whether as a standalone or hybrid technology, is a promising complementary solution platform for 5G backhaul networks [6]. FSOC systems convey bidirectional information at high data rates through the atmosphere between line-of-sight (LOS) optical transceivers. Their numerous advantages include: very high throughput, highly secure transmission, relatively low cost, and ease of deployment when compared to the rigours encountered in the installation of fibre-optic infrastructures, high resistance to signal eavesdropping, and low latency communication since the velocity of light in the atmosphere is about 40% faster than in the fibre-optic cable [7], [8]. In spite of these advantages, the performance of FSOC systems is severely affected by atmospheric impairments.

Dense fog, haze, and snow storms are known to cause the aerosol scattering of optical signals and consequently degrade the availability of FSOC links [9]. In clear weather, atmospheric turbulence or scintillation is the most significant cause of impairment in received signal quality [10]. Atmospheric turbulence causes fluctuations in air temperature, pressure, density, and humidity, which results in rapid variations in the atmosphere's refractive index. The impact of these changes leads to irradiance fluctuations of received information signals [11]. Other turbulence effects on FSOC link performance are disruptions in the coherence of the laser beam and distortions in the optical wave front. Optical wave front distortions result in laser beam broadening, uneven beam energy redistribution within a cross-section of the laser, and beam wander [12]. Improving the bit error rate (BER) performance of FSOC systems during these adverse weather situations is the major challenge in the design of FSOC links [13].

In addition, the misalignment between FSOC transceivers cause pointing errors, which increase the performance degradation of FSOC links. These misalignments arise from either mechanical vibrations in

the system as a result of wind or building movement or errors in the tracking system. The displacement of the laser beam along vertical (elevation) and horizontal (azimuth) directions, which are generally expected to be independent Gaussian random variables, result in pointing errors [14]-[19]. Beam width, boresight, and jitter are the three fundamental components of a pointing error. The beam width is the beam waist (radius computed at e^{-2}), while the jitter is the random offset of the beam centre at the detector plane produced by building motion, minor earthquakes, and dynamic wind loads. The boresight denotes the fixed displacement between the beam centre and the alignment point. It should be noted, however, that boresight displacements are of two kinds: inherent boresight displacement and additional boresight error. The first is related to the spacing between the detector's receive apertures. This inherent boresight displacement corresponds to a fixed distance, namely the distance between each received aperture and its associated alignment point. The second is related to the boresight error caused by the building's thermal expansion [14]-[19].

Conventionally, FSOC systems employ intensity modulation/direct detection (IM/DD) schemes. Most commercial FSOC links are based on the on-off keying (OOK) modulation schemes due to their low cost and simple implementation. However, FSOC systems employing OOK require adaptive thresholding, which is difficult to implement when combating irradiance fading, hence their sub-optimal performance over atmospheric turbulence channels [11], [13], [20]. Binary phase-shift keying subcarrier intensity modulation (BPSK-SIM) FSOC systems have also been investigated extensively. In spite of their superior BER performance when compared with other coherent and non-coherent modulation schemes, BPSK-SIM FSOC links have poor power efficiency when compared to pulse position modulation (PPM) FSOC links [20], [21]. FSOC systems employing sub-carrier intensity quadrature amplitude modulation (SIM-QAM) have also been investigated. SIM-QAM FSOC links are found to have better spectral efficiency compared to PPM FSOC links which exhibit poor bandwidth performance. SIM-QAM FSOC systems have great potential for future FSOC systems since they deliver a higher data rate without an increase in the required bandwidth due to their inherent attribute of transmitting more bits per symbol [11], [22]-[24].

Between April 2015 and February 2016, the First European South African Transmission ExpeRiment (FESTER) was conducted in False Bay, South Africa, to study the influence of atmospheric turbulence on wave propagation [25], [26]. The experiment focused on measuring and modelling optical turbulence, electro-optical system performance, and imaging. Despite the fact that wind direction, wind speed, and the kinematic vertical sensible heat flux all have an effect on optical turbulence, thermal forces were found to have the greatest impact on it, with both exhibiting a direct relationship regardless of the seasons. Additionally, it was discovered that as friction velocity increases, optical turbulence increases. Onshore and

offshore wind directions produced differences in the turbulence strength. With onshore conditions during the winter, the turbulence strength is extremely low. Spring brings an increase in the variability of turbulence strength. The highest refractive index structure parameter (C_n^2) values above 10^{-14} $m^{-2/3}$ may be reached during the summer [25], [26].

The C_n^2, which is also dependent on the root-mean-square (RMS) wind speed and altitude of a location, is used to characterize atmospheric turbulence as weak, moderate or strong at any point in time [27]-[30]. Most of the results obtained in literature ([6], [10]-[13], [20], [23], [31]-[33]) assume arbitrary C_n^2 values or estimate them based on average wind speed measurements for a particular location. In some cases, worst case scenarios of atmospheric turbulence based on the maximum values of wind speed are investigated [29], [33]. However, these measurements are based on data spanning less than 4 years. As a result, they cannot be accurately used to estimate the maximum attenuation due to turbulence-induced irradiance fading. In this paper, the focus is placed on the wind distributions based on data spanning over 8 years for the various locations of interest where FSOC links are to be deployed. This will allow for accurate estimation of the C_n^2, and consequently, correct calculations of the maximum attenuation due to turbulence, and the performance of various FSOC links during such periods.

Therefore, the key contributions of this work are as follows:

1) Computation of the scintillation profile for Gaussian beam FSOC signals in the nine cities under investigation based on the zero inner scale and infinite outer scale model and finite inner and finite outer scale model. To the best of our knowledge, the computation of the scintillation profile for Gaussian beam FSOC links transmitting at 1550 nm in the cities of interest, while considering periods not exceeded 50%, 99%, 99.9%, and 99.99% of the time, have not been reported in open literature.
2) Aerosol scattering losses over various distances for FSOC links transmitting at 1550 nm with respect to events not exceeded 50%, 99%, 99.9%, and 99.99% of the time, for nine major locations in South Africa, are investigated.
3) Outage probabilities of Gaussian beam FSOC links based on the aforementioned scintillation models, while taking into account the effect of pointing errors for events not exceeding the previously mentioned time intervals, are presented for various locations of interest.
4) Analysis of the bit error rate (BER) performance for intensity modulation and direct detection (IM/DD) avalanche photodiode (APD) FSOC systems transmitting at 1550 nm and based on OOK, BPSK, square, and rectangular SIM-QAM schemes during weak, moderate, and strong atmospheric

turbulence, with regards to average weather measurements and events not exceeding 99%, 99.9%, and 99.99% of the time are presented.

The rest of this paper is organized as follows: Section 4.3 presents the ground wind speed distributions for nine cities in South Africa; Section 4.4 presents and analyses the modified Rytov theory based on zero inner scale and infinite outer scale model and finite inner and finite outer scale model for Gaussian beam waves. Section 4.5 presents aerosol scattering losses over various link distances for the nine cities under investigation. Weak, moderate, and strong atmospheric turbulence parameters during clear weather for the locations of interest based on the Lognormal and Gamma-gamma turbulence models are provided in Section 4.6, while outage probability analysis of FSOC links with respect to the effect of pointing errors is presented in Section 4.7. In Section 4.8, the average BER analysis, taking in account pointing error effects for various FSOC systems in weak, moderate, and strong turbulence regimes is derived and the results are analysed, while conclusions are provided in Section 4.9.

4.3 Wind Speed Distribution

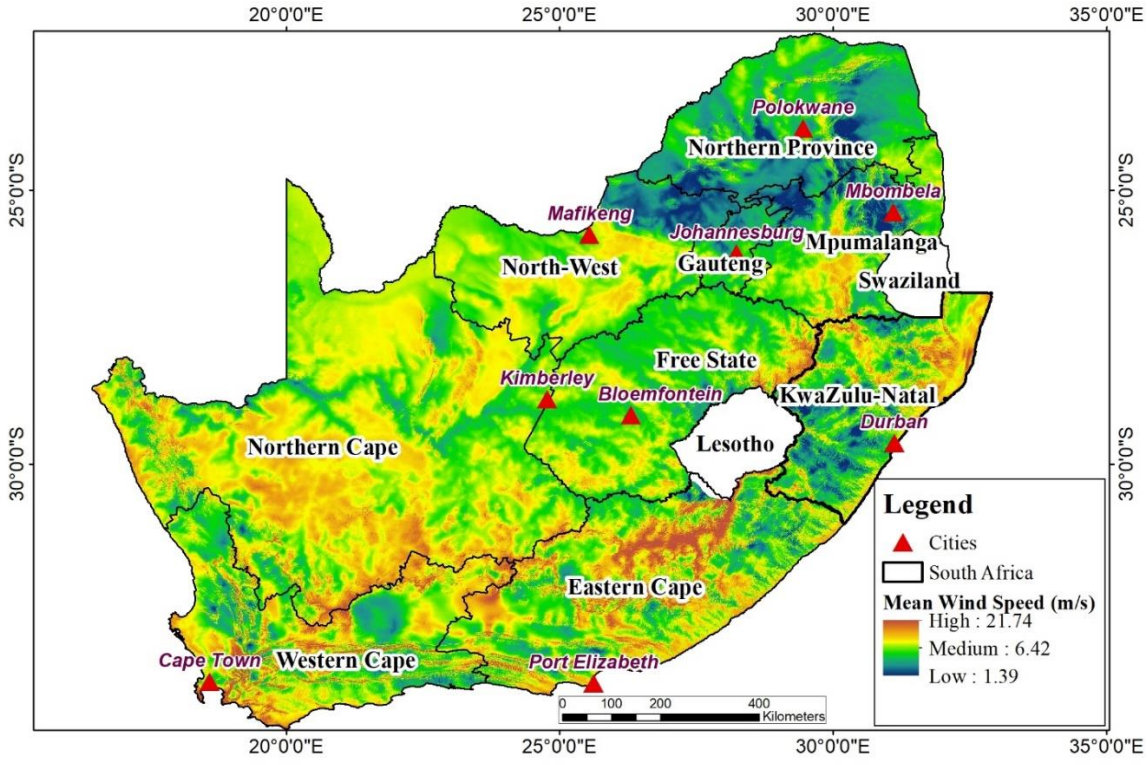

Figure 4.1: Map of South Africa showing the mean wind speed 100 m above ground level for selected cities investigated in this work.

Figure 4.1 shows the map of South Africa depicting the average wind speed (m/s) at 100 metres above ground level for selected cities investigated in this work. The average wind speed data used in plotting Figure 4.1 spans January 2008 until December 2017 and was sourced from [34]. The data in Figure 1 is very similar to the average measurement values presented in Table I of [10], [32]. Wind speed data from January 2010 until June 2018 was also acquired from the South Africa Weather Service (SAWS) for major locations in each of the nine provinces of South Africa. The data was collected hourly for the 8½ year period. The locations of interest investigated in this work are: Bloemfontein, Cape Town, Durban, Johannesburg, Kimberley, Mafikeng, Mbombela, Polokwane, and Port Elizabeth. The data provided by the SAWS, which was collected from various weather stations placed a few meters above the ground, was statistically processed and used for all our computations in this work.

Figures 4.2(a)-(c) alongside all other analysis done in this work, are based on the measurement data obtained from the SAWS. Figure 4.2(a) shows the CDF of wind speed for various cities in South Africa, while Figure 4.2(b) presents the PDF of wind speed for the same locations. In Figure 4.2(a), the coastal cities of Port Elizabeth and Cape Town have the highest probabilities of occurrence of high wind velocities compared to other cities in South Africa. The cities of Bloemfontein, Mbombela, and Polokwane have the highest likelihood of occurrence of low wind speeds.

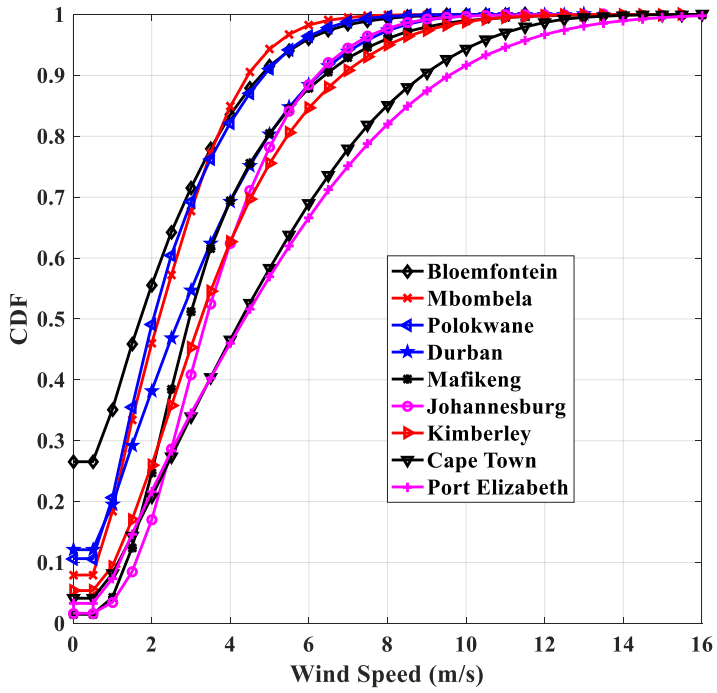

(a)

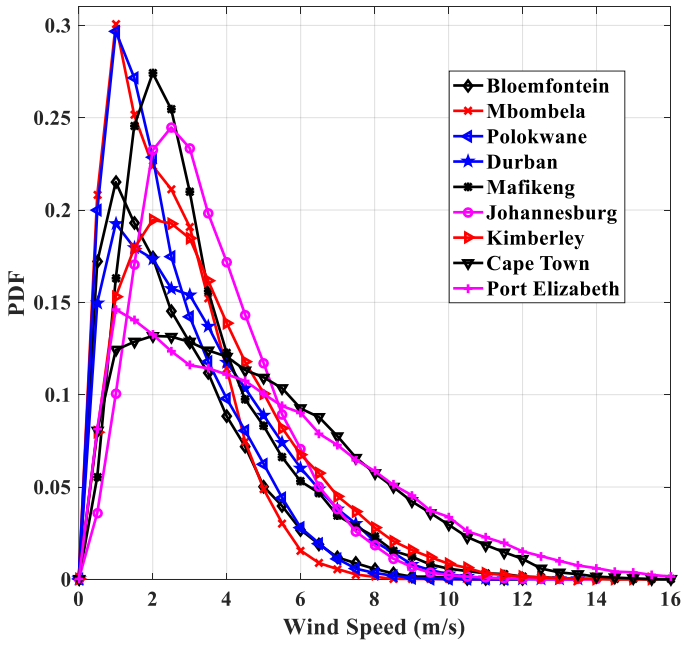

(b)

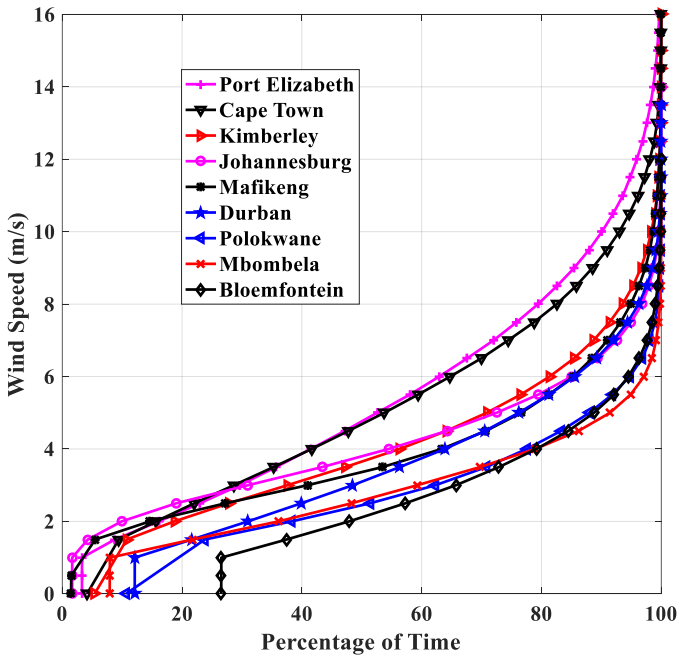

(c)

Figure 4.2: (a) Ground wind speed CDF during clear weather for various cities in South Africa. (b) Ground wind speed PDF during clear weather for different cities in South Africa. (c) Ground wind speed exceedance against percentage of time for various cities of South Africa during clear weather periods.

In Figure 4.2(b), the probability of occurrence of wind speeds of 1 m/s in the cities of Mbombela and Polokwane is ~0.3, while the cities of Cape Town and Port Elizabeth have the lowest likelihood of occurrence (less than 0.15) of low wind velocities when compared with other cities in South Africa. Figure 4.2(c) shows the wind speed exceedance against the percentage of time for the various locations of interest. Figure 4.2(c) validates the results in Figures 4.2(a) and (b). Wind velocities greater than 4 m/s occur ~ 60% of the time in the cities of Port Elizabeth and Cape Town, while in Polokwane, Mbombela, and Bloemfontein, wind speeds higher than 4 m/s occur less than 25% of the time.

The C_n^2 in $m^{-2/3}$ based on the Hufnagel-Andrews-Phillips (HAP) model is presented in [35]-[37] as:

$$C_n^2(a) = M\left[\frac{297}{5\times10^4}\left(\frac{W_{rms}}{27}\right)^2\left(\frac{a+a_s}{10^5}\right)^{10}\exp\left(-\frac{(a+a_s)}{10^3}\right)+\left(2.7\times10^{-16}\right)\exp\left(-\frac{(a+a_s)}{1.5\times10^3}\right)+\left(1.7\times10^{-14}\right)\left(\frac{a_o}{a}\right)^{-4/3}\right], \quad a > a_o \tag{4.1}$$

where M is the scaling factor, a_s is the reference height of the ground above sea level in metres, a_o is the height of the first FSOC transceiver above the ground in metres, a is the altitude from the reference height a_o to the height of the other (second) FSOC transceiver above the ground in metres, and W_{rms} is the root-mean-square (RMS) wind speed in m/s. The RMS wind speed in (4.1) is calculated using the Bufton wind model, which is given in ([35], [36], [38], [39]) as:

$$W_{rms} = \sqrt{\frac{1}{15000}\int_{5000}^{20000}\left[b_s a + W_g + 30\exp\left(-\left(\frac{a-9400}{4800}\right)^2\right)\right]^2 da} \tag{4.2}$$

where b_s is the beam slew rate associated with a satellite moving with respect to an observer on the ground in rad/s and W_g is the ground wind speed in m/s.

The climate of South Africa is considered to be highly variable, both spatially and temporally. Spatial variations in elevation across the country contribute significantly to this variability. According to the Council for Scientific and Industrial Research's (CSIR) Köppen-Geiger climate classification for South Africa, the country is predominantly semi-arid, with influences from temperate and tropical zones [40]-[42]. A large part of the geographical space of South Africa and Namibia is characterized by arid and hot climates, with clear skies and low annual rainfall [28], [29]. Due to the similarities in the two countries' climatic patterns, the C_n^2 based on the HAP model are expected to adequately estimate the atmospheric turbulence losses encountered by FSOC links deployed in various cities of South Africa considered in this work.

Table 4.1: Reference altitude of the ground above sea level for various cities in South Africa.

City	a_s (m)
Cape Town	42
Port Elizabeth	69
Durban	106
Mbombela	865
Polokwane	1226
Kimberley	1196
Mafikeng	1281
Bloemfontein	1354
Johannesburg	1695

Other values where $M = 1$, $b_s = 0.1$ mrad/s, $a_o = 10$ metres, and $a = 15$ metres were used in computing the C_n^2 throughout this work. The altitude measurements above sea level are given in Table 4.1, and the ground wind speed data from SAWS when inserted into (4.1) and (4.2) are used for determining the C_n^2 of the various locations shown in Figure 4.3.

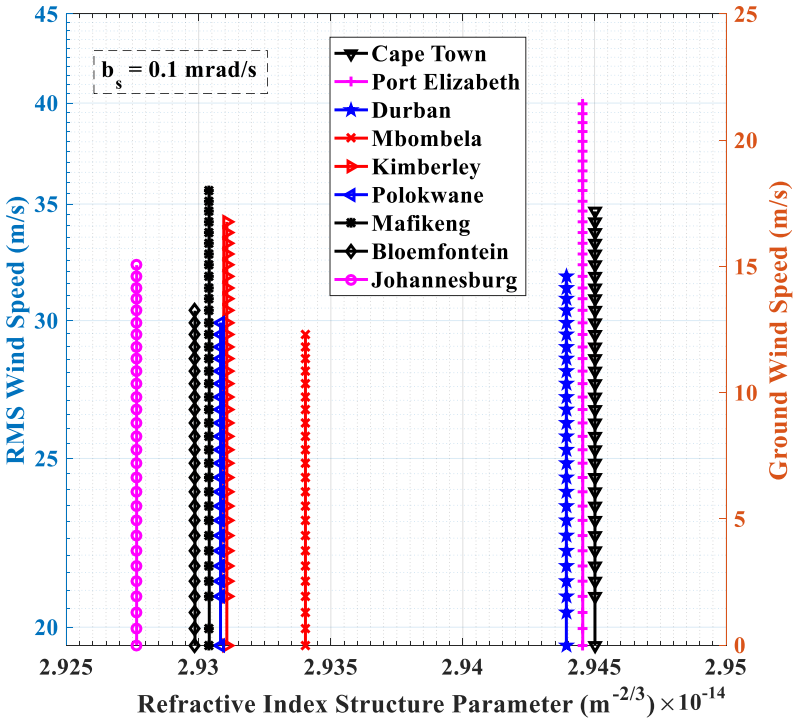

Figure 4.3: RMS and ground wind speed against refractive index structure parameter during clear weather periods for various locations in South Africa.

4.4 Modified Rytov Theory for Gaussian Beam Waves

Fluctuations in the wind speed and atmospheric temperature generate unstable air masses that eventually break up into turbulent eddies or cells of varying scale sizes with constant C_n^2. These inhomogeneities vary in size from macroscale to microscale, and are of different densities [12]. As the Gaussian beams transverse the free space channel, these zones of turbulent air motion act as lenses that scatter the beams off their intended paths. The microscale eddies l_o, also known as the inner scale of turbulence, are approximately 3 to 10 mm near the ground. The macroscale eddies L_o, also referred to as the outer scale of turbulence, are in the range of several metres above the ground level. Optical turbulence is primarily defined by C_n^2, l_o, and L_o [43].

4.4.1 Zero Inner Scale and Infinite Outer Scale model (Infinite Kolmogorov Inertial Range)

The microscale and macroscale effects are neglected in this model. That is, $l_o \simeq 0$ and $L_o \simeq \infty$. The scintillation index or normalized irradiance variance for the zero inner scale and infinite outer scale model is expressed as [44]:

$$\sigma_{SI}^2(0,L) = \exp\left(\sigma_{Inx}^2 + \sigma_{Iny}^2\right) - 1 \tag{4.3}$$

where σ_{Inx}^2 is the large-scale log–irradiance variance and σ_{Iny}^2 is the small-scale log-irradiance variance. The large-scale log-irradiance variance is given as [44]:

$$\sigma_{Inx}^2 = \frac{0.49\sigma_B^2}{\left(1+0.56\sigma_B^{2.4}\right)^{1.167}} \tag{4.4}$$

and the small-scale log-irradiance variance is expressed as [44]:

$$\sigma_{Iny}^2 = \frac{0.51\sigma_B^2}{\left(1+0.69\sigma_B^{2.4}\right)^{0.833}} \tag{4.5}$$

where σ_B^2 is the Rytov variance for a Gaussian-beam wave, and is expressed in [38] as:

$$\sigma_B^2 \cong 3.86\sigma_1^2 \times \left\{0.40\left(\left(1+2\Theta_1\right)^2 + 4\Lambda_1^2\right)^{0.417} \times \cos\left(0.833\tan^{-1}\left(\frac{1+2\Theta_1}{2\Lambda_1}\right)\right) - 0.688\Lambda_1^{0.833}\right\} \tag{4.6}$$

where σ_1^2 is the Rytov variance for a plane wave, Θ_1 is the curvature parameter of the beam at the receiver, and Λ_1 is the Fresnel ratio of the beam at the receiver. σ_1^2 is given as [45]:

$$\sigma_1^2 = 1.23C_n^2 k^{1.167} L^{1.833} \tag{4.7}$$

where k is the wave number of the plane wave. k is calculated in m^{-1} as [45]:

$$k = \frac{2\pi}{\lambda} \tag{4.8}$$

where λ is the wavelength in metres. Θ_1 is expressed as [46]:

$$\Theta_1 = \frac{\Theta_o}{\Theta_o^2 + \Lambda_o^2} = 1 + \frac{L}{F} \tag{4.9}$$

where Θ_o is the Beam curvature parameter at the transmitter, Λ_o is the Fresnel ratio of the beam at the transmitter, L is the propagation distance in metres, and F is the phase front radius of curvature of the beam at the receiver. Λ_1 is given as [46]:

$$\Lambda_1 = \frac{\Lambda_o}{\Theta_o^2 + \Lambda_o^2} = \frac{2L}{kW_1^2} \tag{4.10}$$

where W_1 is the beam radius in free space at the receiver. W_1 can be calculated using [43], [47]:

$$W_1 = W_o\left(\Theta_o^2 + \Lambda_o^2\right)^{0.5} \tag{4.11}$$

where W_o is the beam radius at the transmitter. The beam curvature parameter at the transmitter can be expressed as [46], [47]:

$$\Theta_o = 1 - \frac{L}{F} \tag{4.12}$$

while the Fresnel ratio of the beam at the transmitter is given as [46], [47]:

$$\Lambda_o = \frac{2L}{kW_o^2} \tag{4.13}$$

The phase front radius of curvature of the beam at the receiver can be calculated using [38]:

$$F = \frac{F_o\left(\Theta_o^2 + \Lambda_o^2\right)\left(\Theta_o - 1\right)}{\Theta_o^2 + \Lambda_o^2 - \Theta_o} \tag{4.14}$$

where F_o is the phase front radius of curvature of the beam at the transmitter.

4.4.2 Finite Inner and Finite Outer Scale Model (Modified Atmospheric Spectrum)

In this model, $l_o > 0$ and $L_o < \infty$. The finite inner and finite outer scale effects model is actually the modified atmospheric spectrum. The scintillation index for this model can be expressed as [44]:

$$\sigma_{SI}^2\left(0, L\right) = \exp\left(\sigma_{Inx}^2\left(l_o, L_o\right) + \sigma_{Iny}^2\left(l_o\right)\right) - 1 \tag{4.15}$$

where

$$\sigma_{Inx}^2\left(l_o, L_o\right) = \sigma_{Inx}^2\left(l_o\right) - \sigma_{Inx}^2\left(L_o\right) \tag{4.16}$$

The large-scale log-irradiance variance component due to the inner scale of optical turbulence is given as [44]:

$$\sigma_{Inx}^2\left(l_o\right) = 0.49\sigma_1^2\left(0.333 - 0.5\bar{\Theta}_1 + 0.2\bar{\Theta}_1^{\,2}\right)\left(\frac{\eta_x Q_l}{\eta_x + Q_l}\right)^{1.167} \times \left(1 + 1.75\left(\frac{\eta_x}{\eta_x + Q_l}\right)^{0.5} - 0.25\left(\frac{\eta_x}{\eta_x + Q_l}\right)^{0.583}\right) \tag{4.17}$$

while the large-scale log-irradiance variance component due to outer scale of turbulence is expressed as [44]:

$$\sigma_{Inx}^2(L_o) = 0.49\sigma_1^2\left(0.333 - 0.5\bar{\Theta}_1 + 0.2\bar{\Theta}_1^{\,2}\right)\left(\frac{\eta_{xo}Q_l}{\eta_{xo}+Q_l}\right)^{1.167} \times \left(1 + 1.75\left(\frac{\eta_{xo}}{\eta_{xo}+Q_l}\right)^{0.5} - 0.25\left(\frac{\eta_{xo}}{\eta_{xo}+Q_l}\right)^{0.583}\right) \tag{4.18}$$

where

$$\bar{\Theta}_1 = 1 - \Theta_1 = -\frac{L}{F} \tag{4.19}$$

The nondimensional inner-scale parameter, Q_l, is calculated as [44]:

$$Q_l = \frac{10.89L}{kl_o^2} \tag{4.20}$$

while the nondimensional low-pass cutoff frequency is expressed as [44]:

$$\eta_x = \left(\frac{0.38}{1 - 3.21\bar{\Theta}_1 + 5.29\bar{\Theta}_1^{\,2}} + \left(0.47\sigma_1^2 Q_l^{0.167}\left(\frac{0.333 - 0.5\bar{\Theta}_1 + 0.2\bar{\Theta}_1^{\,2}}{1 + 2.20\bar{\Theta}_1}\right)^{0.857}\right)\right)^{-1} \tag{4.21}$$

The artificial quantity η_{xo}, is defined as [44]:

$$\eta_{xo} = \frac{\eta_{xo}Q_o}{\eta_{xo}+Q_o} \tag{4.22}$$

and the nondimensional outer-scale parameter, Q_o, is given as [44]:

$$Q_o = \frac{64\pi^2 L}{kL_o^2} \tag{4.23}$$

The small-scale log-irradiance variance component due to the inner scale of optical turbulence is defined as [44]:

$$\sigma_{Iny}^2(l_o) = \frac{0.51\sigma_G^2}{\left(1 + 0.69\sigma_G^{2.4}\right)^{0.833}} \tag{4.24}$$

where σ_G^2 is the Rytov variance for a Gaussian-beam wave with inner scale and is derived in [38], [44].

Tables 4.2-4.5 show the RMS and ground wind speeds, C_n^2, and scintillation indices for Gaussian beam waves based on the zero inner scale and infinite outer scale model and finite inner and finite outer scale model for various cities in South Africa while taking into account periods not exceeding 50%, 99%, 99.9%, and 99.99% of the time, respectively. The values in these tables are generated based on RMS wind velocities during clear weather periods for each city and their corresponding C_n^2 calculated using the HAP model in (4.1) and (4.2). It is important to reiterate that data spanning many years are necessary in order to accurately estimate the atmospheric turbulence losses that may be encountered by FSOC systems before their deployment to the desired locations. The scintillation index values based on the zero inner scale and infinite outer scale model in Tables 4.2-4.5 are calculated using (4.3)-(4.14).

Table 4.2: Average atmospheric turbulence parameters during clear weather.

City	Ground Wind Speed (m/s)	RMS Wind Speed (m/s)	C_n^2 ($m^{-2/3}$)	Propagation Length of 2 km					
				Zero Inner Scale and Infinite Outer Scale Model			Finite Inner and Finite Outer Scale Model		
				$\sigma_{SI}^2(0,L)$	α	β	$\sigma_{SI}^2(0,L)$	α	β
Johannesburg	3.8	22.85	2.9277×10^{-14}	0.7488	3.3001	2.9230	0.9311	2.6207	2.5143
Bloemfontein	2.2	21.43	2.9299×10^{-14}	0.7492	3.2985	2.9214	0.9317	2.6192	2.5130
Mafikeng	3.4	22.49	2.9304×10^{-14}	0.7494	3.2981	2.9210	0.9318	2.6188	2.5127
Polokwane	2.5	21.70	2.9308×10^{-14}	0.7494	3.2978	2.9207	0.9319	2.6185	2.5124
Kimberley	3.7	22.76	2.9311×10^{-14}	0.7495	3.2976	2.9205	0.9320	2.6184	2.5123
Mbombela	2.6	21.78	2.9340×10^{-14}	0.7501	3.2955	2.9183	0.9328	2.6163	2.5105
Durban	3.1	22.23	2.9439×10^{-14}	0.7521	3.2884	2.9110	0.9354	2.6096	2.5047
Port Elizabeth	4.8	23.75	2.9446×10^{-14}	0.7522	3.2879	2.9106	0.9356	2.6092	2.5044
Cape Town	4.7	23.66	2.9450×10^{-14}	0.7523	3.2876	2.9102	0.9357	2.6089	2.5041

Table 4.3: Atmospheric turbulence parameters not exceeded 99% of the time during clear weather.

City	Ground Wind Speed (m/s)	RMS Wind Speed (m/s)	C_n^2 ($m^{-2/3}$)	Propagation Length of 1.5 km					
				Zero Inner Scale and Infinite Outer Scale Model			Finite Inner and Finite Outer Scale Model		
				$\sigma_{SI}^2(0,L)$	α	β	$\sigma_{SI}^2(0,L)$	α	β
Johannesburg	9.3	27.87	2.9277×10^{-14}	0.4775	4.8389	4.4556	0.5947	3.8983	3.7156
Bloemfontein	8.0	26.67	2.9299×10^{-14}	0.4778	4.8360	4.4527	0.5951	3.8957	3.7133
Mafikeng	10.5	28.99	2.9304×10^{-14}	0.4779	4.8353	4.4520	0.5952	3.8951	3.7128
Polokwane	7.6	26.30	2.9308×10^{-14}	0.4779	4.8347	4.4515	0.5953	3.8946	3.7123
Kimberley	10.6	29.08	2.9311×10^{-14}	0.4780	4.8344	4.4511	0.5953	3.8943	3.7121
Mbombela	6.9	25.65	2.9340×10^{-14}	0.4784	4.8305	4.4473	0.5959	3.8909	3.7090
Durban	9.4	27.96	2.9439×10^{-14}	0.4799	4.8175	4.4346	0.5978	3.8795	3.6989
Port Elizabeth	14.5	32.76	2.9446×10^{-14}	0.4800	4.8167	4.4338	0.5979	3.8788	3.6983
Cape Town	12.7	31.05	2.9450×10^{-14}	0.4800	4.8161	4.4332	0.5980	3.8783	3.6978

These values range from ~0.067 to ~0.752. In the finite inner and finite outer scale model, the microscale and macroscale eddies are assigned to have the values of 0.005 m and 10 m, respectively. That is, l_o = 0.005 m and L_o = 10 m are used for all the computations of the scintillation indices based on the finite inner and finite outer scale model in Tables 4.2-4.5.

Table 4.4: Atmospheric turbulence parameters not exceeded 99.9% of the time during clear weather.

City	Ground Wind Speed (m/s)	RMS Wind Speed (m/s)	C_n^2 ($m^{-2/3}$)	Propagation Length of 1 km					
				Zero Inner Scale and Infinite Outer Scale Model			Finite Inner and Finite Outer Scale Model		
				$\sigma_{SI}^2(0,L)$	α	β	$\sigma_{SI}^2(0,L)$	α	β
Johannesburg	11.4	29.83	2.9277×10^{-14}	0.2362	9.2025	8.6921	0.2956	7.4062	7.0664
Bloemfontein	10.1	28.61	2.9299×10^{-14}	0.2364	9.1962	8.6859	0.2959	7.4009	7.0615
Mafikeng	13.2	31.53	2.9304×10^{-14}	0.2364	9.1946	8.6844	0.2959	7.3996	7.0603
Polokwane	9.3	27.87	2.9308×10^{-14}	0.2365	9.1934	8.6832	0.2960	7.3986	7.0593
Kimberley	13.0	31.34	2.9311×10^{-14}	0.2365	9.1927	8.6826	0.2960	7.3980	7.0588
Mbombela	8.5	27.13	2.9340×10^{-14}	0.2367	9.1841	8.6743	0.2963	7.3909	7.0522
Durban	11.0	29.46	2.9439×10^{-14}	0.2375	9.1557	8.6469	0.2973	7.3673	7.0304
Port Elizabeth	17.2	35.33	2.9446×10^{-14}	0.2376	9.1539	8.6451	0.2973	7.3658	7.0290
Cape Town	14.7	32.95	2.9450×10^{-14}	0.2376	9.1526	8.6439	0.2974	7.3647	7.0280

Table 4.5: Atmospheric turbulence parameters not exceeded 99.99% of the time during clear weather.

City	Ground Wind Speed (m/s)	RMS Wind Speed (m/s)	C_n^2 ($m^{-2/3}$)	Propagation Length of 500 m					
				Zero Inner Scale and Infinite Outer Scale Model			Finite Inner and Finite Outer Scale Model		
				$\sigma_{SI}^2(0,L)$	α	β	$\sigma_{SI}^2(0,L)$	α	β
Johannesburg	12.7	31.05	2.9277×10^{-14}	0.0672	30.927	29.602	0.0834	24.755	24.182
Bloemfontein	11.2	29.64	2.9299×10^{-14}	0.0673	30.904	29.580	0.0835	24.736	24.164
Mafikeng	16.3	34.47	2.9304×10^{-14}	0.0673	30.898	29.575	0.0835	24.732	24.160
Polokwane	10.4	28.89	2.9308×10^{-14}	0.0673	30.894	29.571	0.0835	24.728	24.156
Kimberley	14.6	32.85	2.9311×10^{-14}	0.0673	30.891	29.568	0.0835	24.726	24.154
Mbombela	10.2	28.71	2.9340×10^{-14}	0.0674	30.860	29.539	0.0836	24.701	24.130
Durban	12.1	30.49	2.9439×10^{-14}	0.0676	30.758	29.440	0.0839	24.619	24.050
Port Elizabeth	19.7	37.73	2.9446×10^{-14}	0.0676	30.752	29.434	0.0839	24.614	24.045
Cape Town	15.9	34.09	2.9450×10^{-14}	0.0676	30.747	29.430	0.0839	24.610	24.041

Equations (4.7)-(4.24) are employed in the calculation of the scintillation index values in the presence of small scale sized and large scale sized eddies. These values range from ~0.083 to ~0.936 based on the periods not exceeded 50%, 99%, 99.9%, and 99.99% of the time. It should be noted that the outer scale of turbulence has little effect on scintillation; it is the inner scale of turbulence that controls scintillation levels.

4.5 Aerosol Scattering Losses

The aerosol scattering coefficient in dB/km, as defined by the Kim and Ijaz models, is given in [42] as:

$$L_{Sca} = \frac{17}{V}\left(\frac{\lambda}{\lambda_\circ}\right)^{-q_\circ} \tag{4.25}$$

where V is the meteorological visibility in km, $\lambda_o = 550nm$ is the maximum spectrum wavelength of the solar band, and $q_\circ$ is the particle size distribution parameter. In the Kim model, $q_\circ$ is expressed in terms of visibility as [48]:

$$q_\circ(V) = \begin{cases} 1.6 & for \quad V > 50km \\ 1.3 & for \quad 6 < V < 50km \\ 0.16V + 0.34 & for \quad 1 < V < 6km \end{cases} \tag{4.26}$$

while $q_\circ$ is expressed in terms of wavelength in the Ijaz model as [49], [50]:

$$q_\circ(\lambda) = 0.1428\lambda - 0.0947 \tag{4.27}$$

For visibility measurements less than 1 km, the Ijaz model is used to calculate scattering losses, while the Kim model is used to calculate the specific attenuation associated with visibility values greater than or equal to 1 km. The two models are used in estimating scattering losses encountered by the transmission wavelength of 1550 nm.

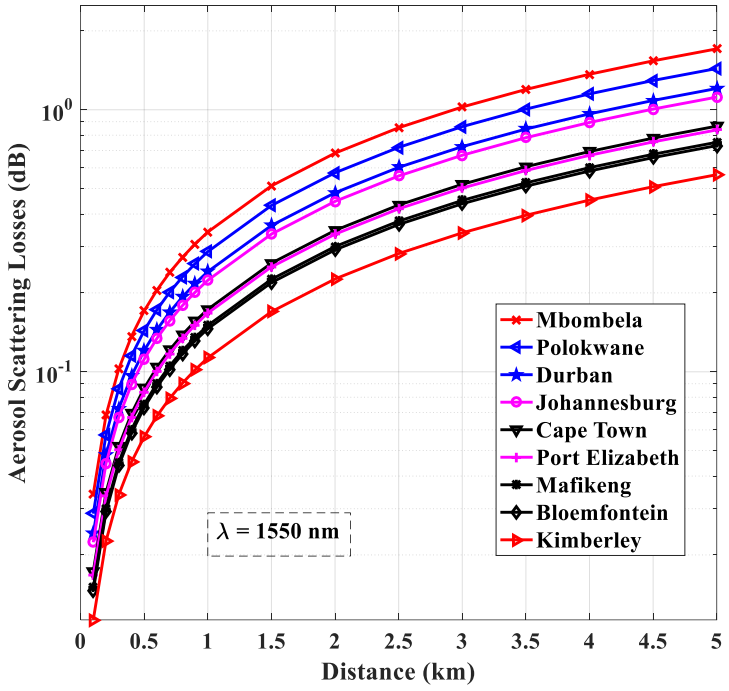

(a)

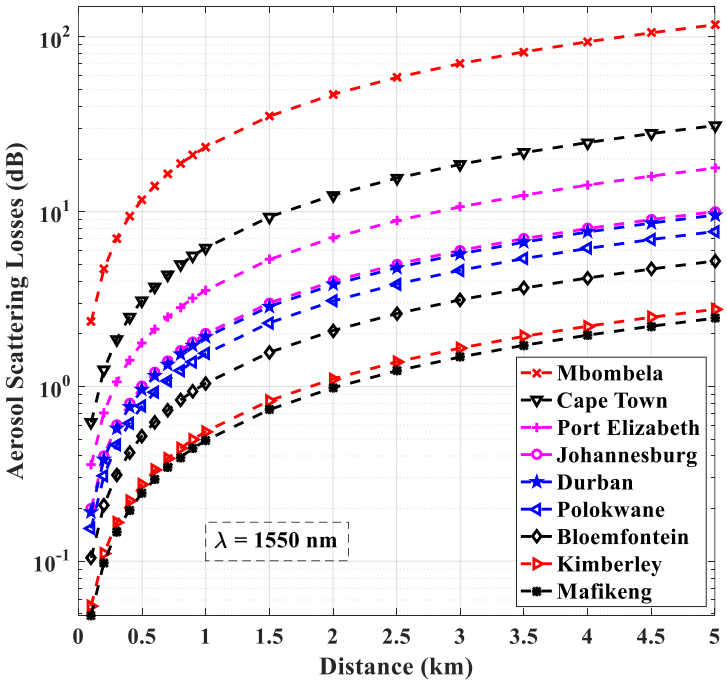
Aerosol Scattering Losses (dB)
Distance (km)
λ = 1550 nm
Mbombela
Cape Town
Port Elizabeth
Johannesburg
Durban
Polokwane
Bloemfontein
Kimberley
Mafikeng

(b)

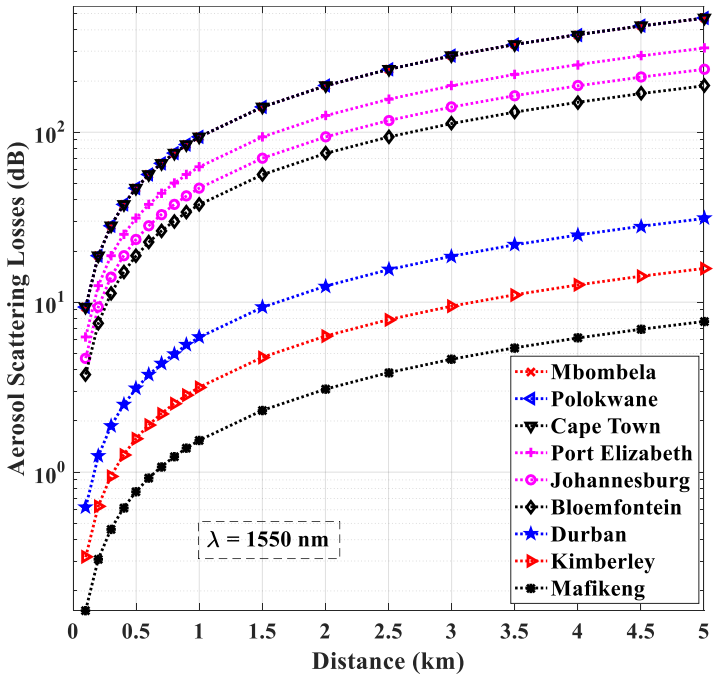
Aerosol Scattering Losses (dB)
Distance (km)
λ = 1550 nm
Mbombela
Polokwane
Cape Town
Port Elizabeth
Johannesburg
Bloemfontein
Durban
Kimberley
Mafikeng

(c)

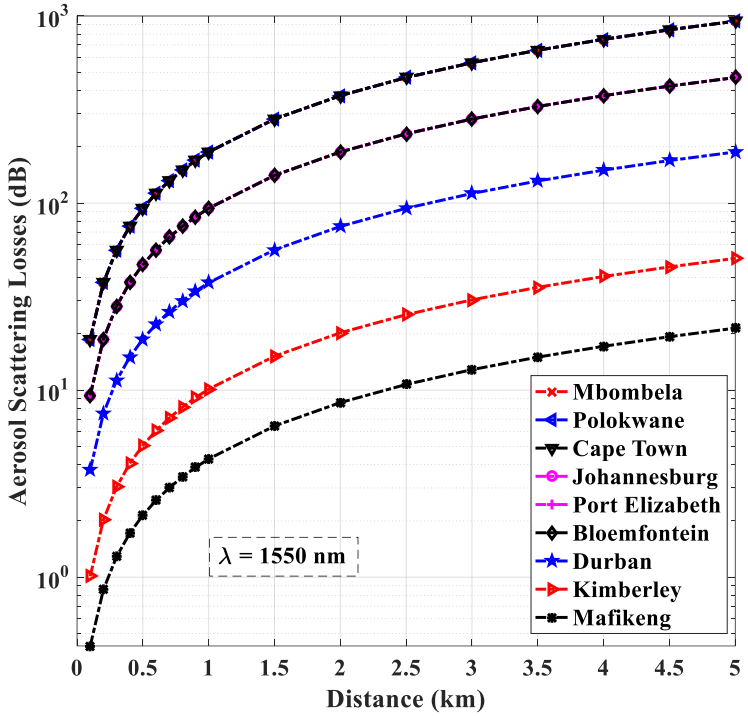

(d)

Figure 4.4: (a) Average Aerosol scattering losses versus link distances under clear atmospheric conditions at 1550 nm for various cities. (b) Aerosol scattering losses versus link distances under clear atmospheric conditions at 1550 nm for various cities not exceeded 99% of the time. **(c):** Aerosol scattering losses versus link distances under clear atmospheric conditions at 1550 nm for various cities not exceeded 99.9% of the time. (d) Aerosol scattering losses versus link distances under clear atmospheric conditions at 1550 nm for various cities not exceeded 99.99% of the time.

The visibility data used in computing the aerosol scattering losses over different distances in Figures 4.4(a)-(d) was obtained from the SAWS for the nine major South African cities of interest investigated in this work. The data was collected three times daily (8:00 a.m., 2:00 p.m., and 8:00 p.m.) over an 8½ year period (January 2010 until June 2018). Over a link distance of 1 km, FSOC links transmitting at 1550 nm in Mbombela would encounter scattering losses of ~0.34, 23, 94, and 188 dB based on the periods not exceeded 50%, 99%, 99.9%, and 99.99% of the time, respectively. Similarly, scattering losses of ~0.15, 0.50, 1.54, and 4.29 dB would be encountered by the same FSOC links over a distance of 1km in the city of Mafikeng as shown in Figures 4.4(a), (b), (c), and (d), respectively.

4.6 Intensity Distribution

In this section, the statistical analysis of the irradiance fluctuations and the channel characteristics for the weak and moderate to strong turbulence regimes are carried out using the Lognormal and Gamma-gamma turbulence distributions, respectively. The PDF of the lognormal distribution is given in ([14], [15], [17], [18]) as:

$$f_I(I) = \frac{I^{-1}}{\sigma_{SI}\sqrt{2\pi}} \exp\left\{-\left(\frac{In(I) + \left(0.5\sigma_{SI}^2\right)}{\sigma_{SI}\sqrt{2}}\right)^2\right\} \tag{4.28}$$

While the PDF of the Gamma-gamma turbulence distribution can be expressed as ([17], [39], [51], [52]):

$$f_I(I) = \frac{2I^{-1}(\alpha\beta I)^{0.5(\alpha+\beta)}}{\Gamma(\alpha)\Gamma(\beta)} K_{\alpha-\beta}\left(2\sqrt{\alpha\beta I}\right) \tag{4.29}$$

where I is the normalized irradiance, $\Gamma(\bullet)$ represents the Gamma function, and $K_{\alpha-\beta}(\bullet)$ is the modified Bessel function of the second kind and of order $\alpha-\beta$. α is the effective number of large-scale turbulence eddies. It is defined as [43]:

$$\alpha = \left(\sigma_x^2\right)^{-1} = \left(\exp\left(\sigma_{\ln x}^2\right) - 1\right)^{-1} \tag{4.30}$$

where σ_x^2 is the normalized large-scale (refractive) variance. β is the effective number of small-scale turbulence eddies. It is given as [43]:

$$\beta = \left(\sigma_y^2\right)^{-1} = \left(\exp\left(\sigma_{\ln y}^2\right) - 1\right)^{-1} \tag{4.31}$$

where σ_y^2 is the normalized small-scale (diffractive) variance. Using equation (07.34.03.0605.01) in [53], where:

$$G_{0,2}^{2,0}\left[\alpha\beta I \middle| \alpha, \beta\right] = 2(\alpha\beta I)^{0.5(\alpha+\beta)} K_{\alpha-\beta}\left(2\sqrt{\alpha\beta I}\right) \tag{4.32}$$

Equation (4.29) can be rewritten as:

$$f_I(I) = \frac{I^{-1}}{\Gamma(\alpha)\Gamma(\beta)} G_{0,2}^{2,0}\left[\alpha\beta I \middle| \begin{matrix} - \\ \alpha, \beta \end{matrix}\right], I > 0 \tag{4.33}$$

Where $G_{u,v}^{s,t}\left(z \middle| \begin{matrix} a_1, \ldots, a_p \\ c_1, \ldots, c_p \end{matrix}\right)$ is the Meijer G function, which is well defined in [54]. Integrating $f_I(I)$ in (4.33) gives the CDF of I. This is derived by using equation (07.34.21.0003.01) in [53]. Thus we have:

$$F_I(I) = \frac{1}{\Gamma(\alpha)\Gamma(\beta)} G_{1,3}^{2,1}\left[\alpha\beta I \middle| \begin{matrix} 1 \\ \alpha, \beta, 0 \end{matrix}\right], I > 0 \tag{4.34}$$

In this work, pointing errors represent the misalignment between the transmitter and receiver caused by the laser beam being displaced horizontally or vertically, i.e., a two-dimensional configuration is being considered. The transmitter and receiver planes are assumed to be parallel, and the laser beam is

perpendicular to the receiver area. The pointing error parameter, ξ, is defined as the ratio between the equivalent beam waist or radius at the receiver (W_{Leq}) and the standard deviation of the jitter or pointing error at the receiver (σ_s). It can be expressed as ([6], [16], [55], [56]):

$$\xi = \frac{W_{Leq}}{2\sigma_s} \tag{4.35}$$

The beam waist W_L of a Gaussian beam which is the radius calculated at e^2, determines the value of the parameter, W_{Leq} at distance, L. W_{Leq} is given as ([6], [16], [18], [55]-[57]):

$$W_{Leq} = \left(\frac{W_L^2 \sqrt{\pi} erf(v)}{2v \exp(-v^2)} \right)^{0.5} \tag{4.36}$$

where $W_L = W_o \sqrt{(\Theta_o + \Lambda_o)\left(1+\left(1.63\Lambda_1 \sigma_1^{2.4}\right)\right)}$, $erf(.)$ is the error function and parameter v is expressed as ([6], [16], [55], [56]):

$$v = \frac{r\sqrt{\pi}}{W_L\sqrt{2}} \tag{4.37}$$

where r represents the radius of a circular detector aperture. At distance $L = 0$, the fraction of the collected power is represented by parameter A_o. It is expressed as ([6], [16], [55], [56]):

$$A_o = \left[erf(v)\right]^2 = \left[1 - erfc(v)\right]^2 \tag{4.38}$$

where $erfc(.)$ is the complementary error function.

Therefore, the PDF of the Lognormal distribution, considering the effect of pointing errors, is derived in [17], [18], [58] as:

$$f_I(I) = \frac{\xi^2}{(A_o)^{\xi^2}} I^{\xi^2 - 1} \frac{1}{2} \exp(q) erfc\left(\frac{In\left(I/A_o\right) + p}{\sigma_{SI}\sqrt{2}} \right) \tag{4.39}$$

where

$$p = 0.5\sigma_{SI}^2 + \xi^2 \sigma_{SI}^2 \tag{4.40}$$

and

$$q = \frac{\xi^2 \sigma_{SI}^2 \left(1 + \xi^2\right)}{2} \tag{4.41}$$

Additionally, the PDF of the Gamma-gamma distribution model, taking into account the effects of misalignment, is derived in [6], [16], [56] as:

$$f_I(I) = \frac{\alpha\beta\xi^2}{A_o \Gamma(\alpha)\Gamma(\beta)} G_{1,3}^{3,0}\left[\frac{\alpha\beta}{A_o} I \middle| \begin{matrix} \xi^2 \\ \xi^2 - 1, \alpha - 1, \beta - 1 \end{matrix} \right], I > 0 \tag{4.42}$$

After some mathematical manipulations, the PDF can be further simplified as [6], [56]:

$$f_I(I)=\frac{I^{-1}\xi^2}{\Gamma(\alpha)\Gamma(\beta)}G_{1,3}^{3,0}\left[\frac{\alpha\beta\xi^2}{\xi^2+1}I\middle|\begin{matrix}\xi^2+1\\ \xi^2,\alpha,\beta\end{matrix}\right],I\geq 0 \tag{4.43}$$

The expression for the CDF of the Gamma-gamma distribution model, considering pointing error effects, is derived in [6], [56] as:

$$F_I(I)=\frac{\xi^2}{\Gamma(\alpha)\Gamma(\beta)}G_{2,4}^{3,1}\left[\frac{\alpha\beta\xi^2}{\xi^2+1}I\middle|\begin{matrix}1,\xi^2+1\\ \xi^2,\alpha,\beta,0\end{matrix}\right] \tag{4.44}$$

For commercial FSOC links employing the use of intensity modulation/direct detection (IM/DD) schemes and avalanche photodiode (APD) detectors, the instantaneous signal-to-noise ratio (SNR) at the receiver is defined as ([42], [56], [59], [60]):

$$\gamma=\frac{\left(2\Re g_a P_x I\right)^2}{\sigma_n^2}=\bar{\gamma}I^2 \tag{4.45}$$

where $\Re$ is the responsivity, g_a is the APD gain, σ_n^2 is the total noise at the APD receiver, and P_x is the average optical power detected at the receiver. P_x is well defined in equation (9) of [42].

The average SNR at the receiver is defined as [42, 56]:

$$\bar{\gamma}=\frac{\left(2\Re g_a P_x\right)^2}{\sigma_n^2} \tag{4.46}$$

The total noise at the APD receiver comprises the thermal and shot noise. It is given as ([42], [51], [59], [60]):

$$\sigma_n^2=\frac{4TK_bR_bF_n}{R}I+2q\Re g_a^2F_aR_bP_xI \tag{4.47}$$

where T is the temperature of the receiver, K_b is the Boltzmann constant, R_b is the bit rate, F_n is the noise figure of the amplifier, R is the APD load resistance, q is the electron charge, and F_a is excess noise factor. The excess noise factor is expressed as ([42], [51], [59], [60]):

$$F_a=2-g_a^{-1}-2k_a+k_ag_a^{-1}+k_ag_a \tag{4.48}$$

where k_a is the ionization factor.

The PDF of SNRs for weak atmospheric turbulence using the Lognormal distribution model with pointing errors is derived by substituting (4.45) into (4.39), and is given below as [18]:

$$f_\gamma(\gamma)=\frac{0.5\xi^2}{(A_o)^{\xi^2}}\frac{\gamma^{\left(0.5\xi^2\right)-1}}{\bar{\gamma}^{0.5\xi^2}}\frac{1}{\sqrt{\pi}}\exp(q)erfc\left(\frac{0.5In\left(\frac{\gamma}{\bar{\gamma}A_o^2}\right)+p}{\sigma_{SI}\sqrt{2}}\right) \tag{4.49}$$

Applying the relation in [18], [31] where:

$$Q(\gamma)=0.5erfc\left(\frac{\gamma}{\sqrt{2}}\right)\approx\frac{1}{12}\exp\left(-\frac{\gamma^2}{2}\right)+\frac{1}{4}\exp\left(-\frac{2\gamma^2}{3}\right) \tag{4.50}$$

Equation (4.49) becomes:

$$f_\gamma(\gamma)=\frac{\xi^2}{(A_o)^{\xi^2}}\frac{\gamma^{\left(0.5\xi^2\right)-1}}{\bar{\gamma}^{0.5\xi^2}}\frac{1}{\sqrt{\pi}}\exp(q)\left[\frac{1}{12}\exp\left(-\frac{1}{2}\left(\frac{0.5In\left(\frac{\gamma}{\bar{\gamma}A_o^2}\right)+p}{\sigma_{SI}}\right)^2\right)+\frac{1}{4}\exp\left(-\frac{2}{3}\left(\frac{0.5In\left(\frac{\gamma}{\bar{\gamma}A_o^2}\right)+p}{\sigma_{SI}}\right)^2\right)\right] \tag{4.51}$$

Table 4.6: Commercial FSOC link parameters used in computations

FSOC Link Parameters	
Light Source	Laser
Wavelength (λ)	1550 nm
Transmit Power (P_T)	20 dBm
Receiver Sensitivity (R_S)	-40 dBm
Receiver Aperture Diameter (D)	10 cm
Eye Safety	Class 1M
Transmit Beam Divergence Angle (ϕ)	1.75 mrad
Responsivity $(\Re)$	0.5 A/W
Bit Rate (R_b)	10 Gb/s
Detector	Avalanche Photodiode (APD)
Boltzmann's Constant (K_b)	1.381×10^{-23} J/K
Temperature (T)	298 K
Planck's Constant (h)	6.626×10^{-34} Js
Speed of Light (c)	3×10^{8} m/s
APD Load Resistance (R)	1000 Ω
APD Gain (g_a)	50
Amplifier Noise Figure (F_n)	2
Charge of an Electron	1.602×10^{-19} C
Ionization factor for InGaAs APD (k_a)	0.7

The PDF of SNRs for moderate to strong atmospheric turbulence using the Gamma-gamma model with pointing errors, as derived in [55], [56], is given as:

$$f_\gamma(\gamma)=\frac{\gamma^{-1}\xi^2}{2\Gamma(\alpha)\Gamma(\beta)}G_{1,3}^{3,0}\left[\frac{\alpha\beta\xi^2}{\xi^2+1}\left(\frac{\gamma}{\bar{\gamma}}\right)^{0.5}\middle|\begin{matrix}\xi^2+1\\ \xi^2,\alpha,\beta\end{matrix}\right] \tag{4.52}$$

The $\sigma_{SI}^2(0,L)$ is used in characterizing the atmospheric turbulence strength due to the effect of scintillation. In a weak turbulence regime, $\sigma_{SI}^2(0,L)<1$, and the Lognormal distribution model is employed. For moderate to strong fluctuations, $\sigma_{SI}^2(0,L)\geq 1$, and the Gamma-gamma turbulence distribution is used [38], [44]. In certain instances where $\sigma_{SI}^2(0,L)<1$ but $\alpha\beta\leq 10$ or $\Gamma(\alpha)\Gamma(\beta)\leq 50$, then the Gamma-gamma distribution is employed. In other situations, where $\sigma_{SI}^2(0,L)<1$ and $\Gamma(\alpha)\Gamma(\beta)\geq 100$ or $\alpha\beta\geq 20$, some computations involving the Gamma-gamma distribution would produce undefined results [43]. Thus, in this work, when $\sigma_{SI}^2(0,L)<1$ and $\alpha\beta>10$ or $\Gamma(\alpha)\Gamma(\beta)>50$, the Lognormal distribution is used.

4.7 Outage Probability Analysis

Outage probability is a critical performance indicator that defines the likelihood of the instantaneous SNR going below the threshold SNR. Once this occurs, the link's communication will fail. It is expressed below as [45], [61]:

$$\Pr_{out} = \Pr obability\left[\gamma \leq \gamma_{th}\right] = F_{\gamma}\left[\gamma_{th}\right] \tag{4.53}$$

where γ_{th} is the threshold SNR and $F_{\gamma}\left[\gamma_{th}\right]$ is the CDF of the instantaneous SNR.

From (4.45), the normalized irradiance at the receiver can be expressed as [6], [57]:

$$I = \left(\frac{\gamma}{\bar{\gamma}}\right)^{0.5} = \left(\frac{\gamma_{th}}{\bar{\gamma}}\right)^{0.5} \tag{4.54}$$

Therefore, substituting for I in (4.44) presents the expression for estimating the outage probability of the FSO link over the turbulent atmospheric channel while considering the effect of pointing errors [6], [56]:

$$\Pr_{out} = \frac{\xi^2}{\Gamma(\alpha)\Gamma(\beta)} G_{2,4}^{3,1}\left[\frac{\alpha\beta\xi^2}{\xi^2+1}\left(\frac{\gamma_{th}}{\bar{\gamma}}\right)^{0.5}\middle| \begin{matrix} 1, \xi^2+1 \\ \xi^2, \alpha, \beta, 0 \end{matrix}\right] \tag{4.55}$$

Figures 4.5(a), (b), (c) and (d) are based on the numerical values in Tables 4.2, 4.3, 4.4, and 4.5, respectively. These figures are generated using the parameters in Table 4.6, while computing with (4.1)-(4.3), (4.15), (4.30), (4.31), (4.35), (4.46), and (4.55). The average receiver SNRs needed to achieve various outage probabilities over different link distances while considering the effect of pointing errors in the presence of turbulent eddies are presented in Figures 4.5(a)-(d) for the locations of interest. In these figures, the average receiver SNRs required to attain different outage probabilities are quite similar. It is also evident from these figures that the impact of the normalized jitter standard deviation on the outage probability is significant (when comparing Figures 4.5(c) and (d) where $\frac{\sigma_s}{r}=1$ to Figures 4.5(a) and (b) where $\frac{\sigma_s}{r}=2$).

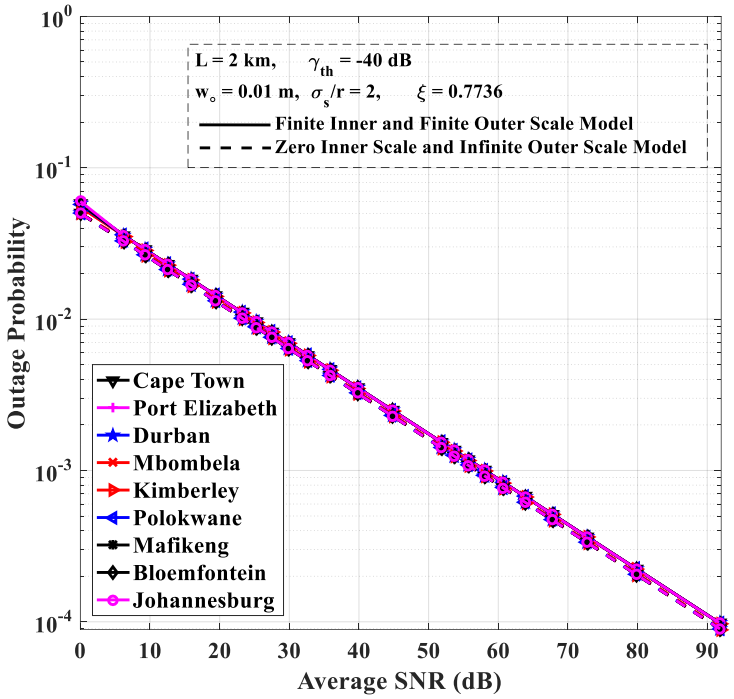

(a) Average values

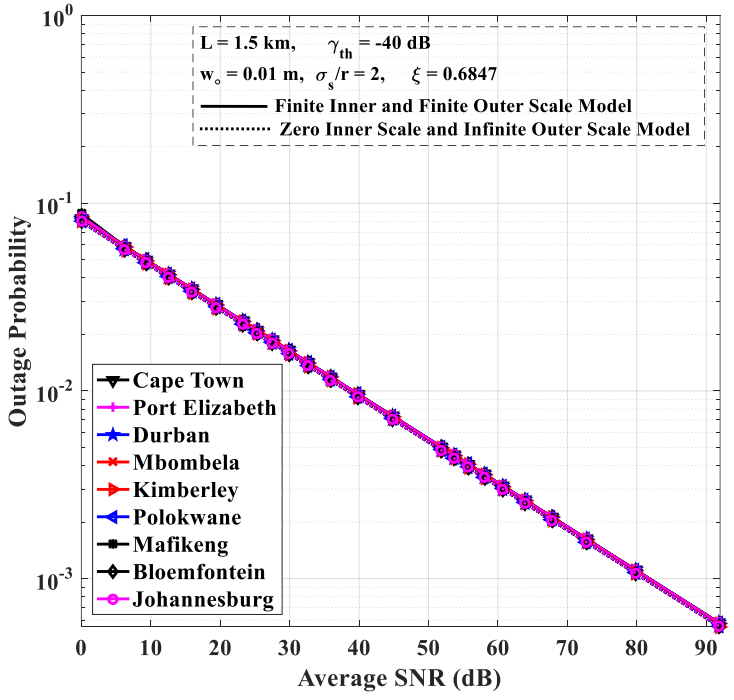

(b) Values not exceeded 99% of the time

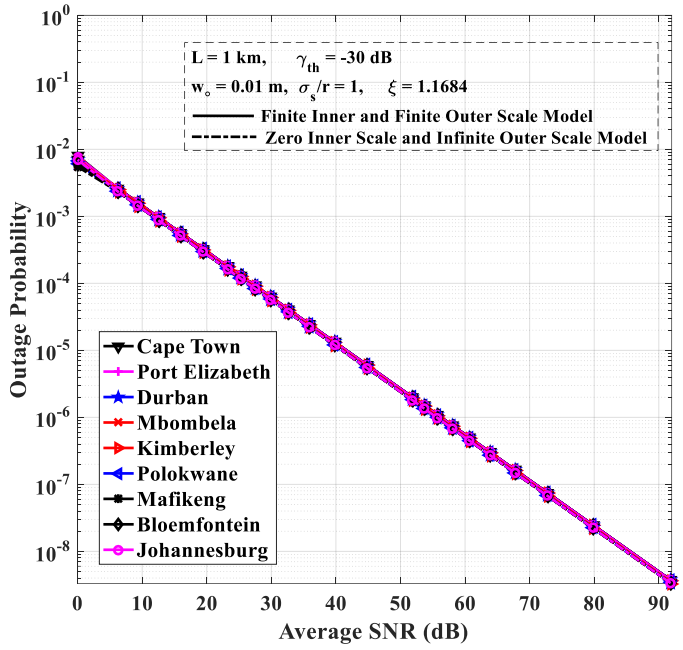

(c) Values not exceeded 99.9% of the time

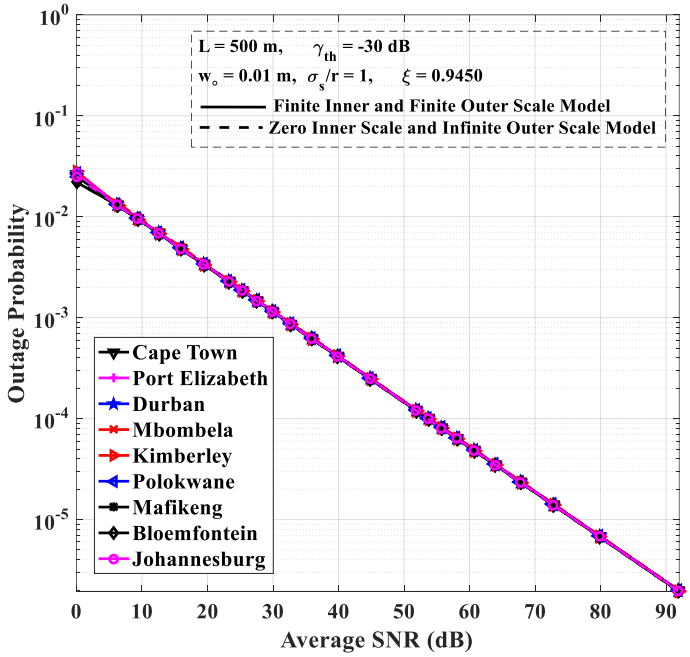

(d) Values not exceeded 99.99% of the time

Figure 4.5: Outage probability vs Average SNR (dB) based on zero inner scale and infinite outer scale model and finite inner and finite outer scale model for weak and moderate to strong atmospheric turbulence periods in different locations of South Africa

This implies that the lower the value of $\frac{\sigma_s}{r}$, the better the overall system performance. Additionally, the higher the value of ξ, the better the outage probability performance of the FSOC links. In the presence of finite inner and outer scales of turbulence, that is, where l_o = 0.005 m and L_o = 10 m, the outage probabilities of the FSOC links are quite similar to when these turbulent eddies have sizes of zero and infinity in the Kolmogorov model with an infinitely large inertial range.

4.8 Average Bit Error Rate (BER) Analysis

The average BER of an IM/DD single-input single-output (SISO) FSOC link based on a specific modulation scheme during periods of atmospheric turbulence is defined as [31], [56], [58]:

$$P_{BER} = \int_0^\infty P(e|\gamma) f_\gamma(\gamma) d\gamma \tag{4.56}$$

where $P(e|\gamma)$ is the conditional BER of the FSO link based on a specific modulation scheme and $f_\gamma(\gamma)$ represent the PDFs of the Lognormal and Gamma-gamma turbulence models while considering the effects of pointing errors in (4.51) and (4.52), respectively.

4.8.1 Return-to-zero On-off Keying (RZ-OOK) FSO Links

The conditional BER for RZ-OOK SISO FSOC links in the absence of atmospheric turbulence is given as [56]:

$$P_{RZ-OOK}(e/\gamma) = Q\left(\frac{\sqrt{2\gamma}}{2}\right) = 0.5erfc\left(0.5\gamma^{0.5}\right) \tag{4.57}$$

1) Weak Atmospheric Turbulence

In order to derive the expression for the BER of RZ-OOK SISO FSOC links in the presence of weak atmospheric turbulence, inserting (4.51) and (4.57) into (4.56) yields:

$$P_{RZ-OOK} = \int_0^\infty \left(0.5erfc\left(0.5\gamma^{0.5}\right) \bullet \frac{\xi^2}{\left(A_o\right)^{\xi^2}} \frac{\gamma^{\left(0.5\xi^2\right)-1}}{\bar{\gamma}^{0.5\xi^2}} \frac{\exp(q)}{\sqrt{\pi}} \bullet \left[\frac{1}{12}\exp\left(-\left(\frac{0.5In\left(\frac{\gamma}{\bar{\gamma}A_o^2}\right)+p}{4\sigma_{SI}} \right)^2 \right) + \frac{1}{4}\exp\left(-\left(\frac{2In\left(\frac{\gamma}{\bar{\gamma}A_o^2}\right)+4p}{9\sigma_{SI}} \right)^2 \right) \right] \right) d\gamma \tag{4.58}$$

Variable substitutions where:

$$z_1 = \frac{0.5In\left(\frac{\gamma}{\bar{\gamma}A_o^2}\right)+p}{4\sigma_{SI}} \tag{4.59}$$

and

$$z_2 = \frac{2In\left(\frac{\gamma}{\bar{\gamma} A_o^2}\right) + 4p}{9\sigma_{SI}} \tag{4.60}$$

are employed. Making γ the subject of (4.59) and (4.60) yield:

$$\gamma = \bar{\gamma} A_o^2 \exp\left(8 z_1 \sigma_{SI} - 2p\right) \tag{4.61}$$

and

$$\gamma = \bar{\gamma} A_o^2 \exp\left(4.5 z_2 \sigma_{SI} - 2p\right) \tag{4.62}$$

Differentiating γ with respect to z_1 and z_2 in (4.61) and (4.62), respectively, gives:

$$d\gamma = 8\bar{\gamma} A_o^2 \sigma_{SI} \exp\left(8 z_1 \sigma_{SI} - 2p\right) d z_1 \tag{4.63}$$

and

$$d\gamma = 4.5\bar{\gamma} A_o^2 \sigma_{SI} \exp\left(4.5 z_2 \sigma_{SI} - 2p\right) d z_2 \tag{4.64}$$

Therefore, substituting (4.59)-(4.64) in (4.58) generates:

$$P_{RZ-OOK} = \int_0^{\infty} \left(\frac{\xi^2 \sigma_{SI} \exp(q)}{3\sqrt{\pi}} \left(\left(\exp\left(8 z_1 \sigma_{SI} - 2p\right)\right)^{\left(0.5\xi^2\right)} \bullet erfc\left(\frac{\sqrt{\bar{\gamma} A_o^2 \exp\left(8 z_1 \sigma_{SI} - 2p\right)}}{2} \right) \right) \bullet \exp\left(-z_1^2\right) \right) d z_1 + \int_0^{\infty} \left(\frac{9\xi^2 \sigma_{SI} \exp(q)}{16\sqrt{\pi}} \left(\left(\exp\left(4.5 z_2 \sigma_{SI} - 2p\right)\right)^{\left(0.5\xi^2\right)} \bullet erfc\left(\frac{\sqrt{\bar{\gamma} A_o^2 \exp\left(4.5 z_2 \sigma_{SI} - 2p\right)}}{2} \right) \right) \bullet \exp\left(-z_2^2\right) \right) d z_2 \tag{4.65}$$

Since a closed form solution does not exist for the above integration, the Gauss-Hermite quadrature approximation, as presented in [62], [63], is used to evaluate the integration, where:

$$\int_{-\infty}^{\infty} \exp\left(-x^2\right) f(x) dx \cong \sum_{i=1}^{N} W_i f\left(z_i\right) \tag{4.66}$$

Therefore, the BER of RZ-OOK SISO FSOC links in the presence of weak atmospheric turbulence and pointing errors is:

$$P_{RZ-OOK} = \frac{\xi^2 \sigma_{SI} \exp(q)}{2\sqrt{\pi}} \bullet \left(\left(\frac{1}{3} \sum_{i=1}^{N} W_i \left(\left(\exp\left(8 z_1 \sigma_{SI} - 2p\right)\right)^{\left(0.5\xi^2\right)} \bullet erfc\left(\frac{\sqrt{\bar{\gamma} A_o^2 \exp\left(8 z_1 \sigma_{SI} - 2p\right)}}{2} \right) \right) \right) + \left(\frac{9}{16} \sum_{i=1}^{N} W_i \left(\left(\exp\left(4.5 z_2 \sigma_{SI} - 2p\right)\right)^{\left(0.5\xi^2\right)} \bullet erfc\left(\frac{\sqrt{\bar{\gamma} A_o^2 \exp\left(4.5 z_2 \sigma_{SI} - 2p\right)}}{2} \right) \right) \right) \right) \tag{4.67}$$

where the values of the weights, W_i, and zeros of the Hermite polynomial, z_i, are given in [62], [63].

2) Moderate to Strong Atmospheric Turbulence

Applying equation (07.34.03.0619.01) in [53] to (4.57), we obtain:

$$G_{1,2}^{2,0}\left[0.25\gamma\middle|\begin{matrix}1\\0,0.5\end{matrix}\right]=\pi^{0.5}erfc\left(0.5\gamma^{0.5}\right) \tag{4.68}$$

Therefore, combining (4.57) and (4.68) yields:

$$P_{RZ-OOK}(e\,|\,\gamma)=\frac{0.5}{\pi^{0.5}}G_{1,2}^{2,0}\left[0.25\gamma\middle|\begin{matrix}1\\0,0.5\end{matrix}\right] \tag{4.69}$$

Inserting (4.52) and (4.69) into (4.56) gives:

$$P_{RZ-OOK}=\frac{\xi^2}{4\Gamma(\alpha)\Gamma(\beta)\pi^{0.5}}\bullet\int_0^{\infty}\gamma^{-1}\bullet G_{1,2}^{2,0}\left[0.25\gamma\middle|\begin{matrix}1\\0,0.5\end{matrix}\right]\bullet G_{1,3}^{3,0}\left[\frac{\alpha\beta\xi^2}{\xi^2+1}\left(\frac{\gamma}{\bar{\gamma}}\right)^{0.5}\middle|\begin{matrix}\xi^2+1\\\xi^2,\alpha,\beta\end{matrix}\right]d\gamma \tag{4.70}$$

Applying equation (07.34.21.0013.01) in [53] to evaluate (4.70) yields:

$$P_{RZ-OOK}=\frac{\xi^2 2^{\alpha+\beta-4}}{\pi^{1.5}\Gamma(\alpha)\Gamma(\beta)}G_{4,7}^{6,2}\left[\left(\frac{\alpha\beta\xi^2}{\xi^2+1}\right)^2\frac{1}{4\bar{\gamma}}\middle|\begin{matrix}1,0.5,\frac{\xi^2+1}{2},\frac{\xi^2+2}{2}\\\frac{\xi^2}{2},\frac{\xi^2+1}{2},\frac{\alpha}{2},\frac{\alpha+1}{2},\frac{\beta}{2},\frac{\beta+1}{2},0\end{matrix}\right] \tag{4.71}$$

Further simplification of (4.71) gives:

$$P_{RZ-OOK}=\frac{\xi^2 2^{\alpha+\beta-4}}{\pi^{1.5}\Gamma(\alpha)\Gamma(\beta)}G_{3,6}^{5,2}\left[\left(\frac{\alpha\beta\xi^2}{\xi^2+1}\right)^2\frac{1}{4\bar{\gamma}}\middle|\begin{matrix}1,0.5,\frac{\xi^2+2}{2}\\\frac{\xi^2}{2},\frac{\alpha}{2},\frac{\alpha+1}{2},\frac{\beta}{2},\frac{\beta+1}{2},0\end{matrix}\right] \tag{4.72}$$

In Figures 4.6(b)-(d), the BER results of the FSOC links in all the cities of interest are generated using (4.1)-(4.3), (4.15), (4.35), (4.38), (4.40), (4.41), (4.46), and (4.67) because the scintillation parameters in those locations fall within the weak atmospheric turbulence regime over a link distance of 1.5, 1, and 0.5 km, respectively. The BER results of the cities in Figure 4.6(a) are computed using (4.1)-(4.3), (4.15), (4.30), (4.31), (4.35), (4.46), and (4.72). Figures 4.6(a)-(d) present the BERs computed for the zero inner scale and infinite outer scale model and finite inner and finite outer scale model for different receive SNRs, and are based on the numerical values in Tables 4.2, 4.3, 4.4, and 4.5, respectively. It is imperative to state that the presence of misalignment errors ($\frac{\sigma_s}{r}=2$) in Figures 4.6(a) and (b) strongly impacts on the BER performance of the FSOC links, while the low presence of pointing errors ($\frac{\sigma_s}{r}=1$) in Figures 4.6(c) and (d) indicate better BERs for all the locations investigated. Additionally, the presence of the inner and outer scales of turbulence where l_o = 0.005 m and L_o = 10 m, cause poorer BERs when compared to the results of the zero inner scale and infinite outer scale model. It is also important to note that the inner scale bump is responsible for the higher values of scintillation obtained when the modified atmospheric spectrum is employed. The BER performances of the FSOC links deployed in the cities investigated are quite similar, as shown in the four figures.

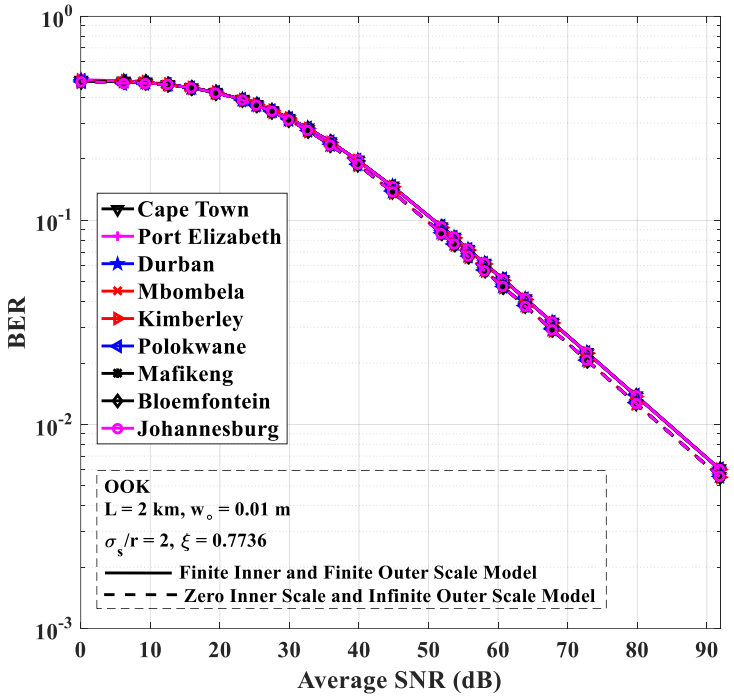

(a) Average values

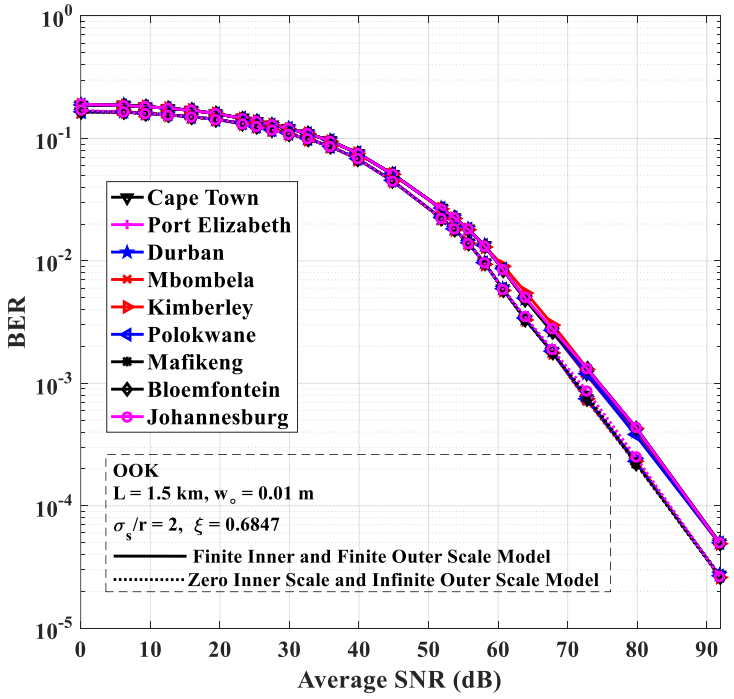

(b) Values not exceeded 99% of the time

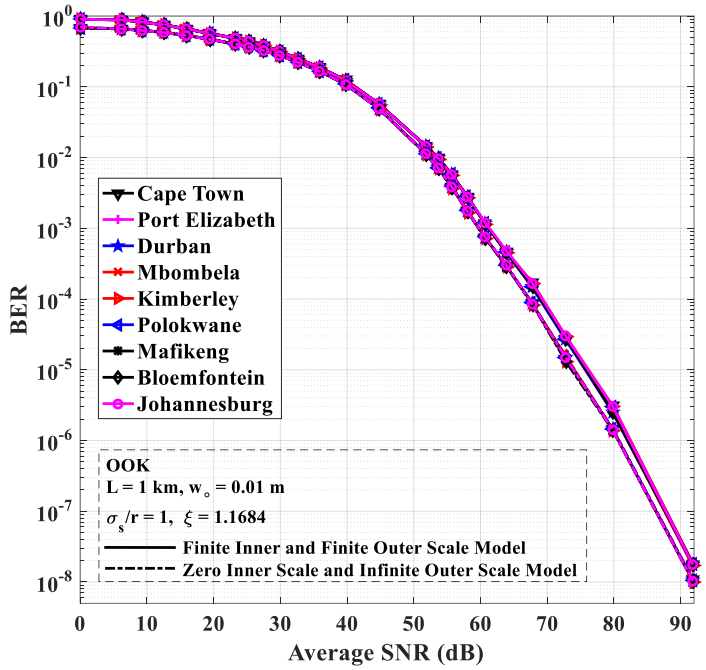

(c) Values not exceeded 99.9% of the time

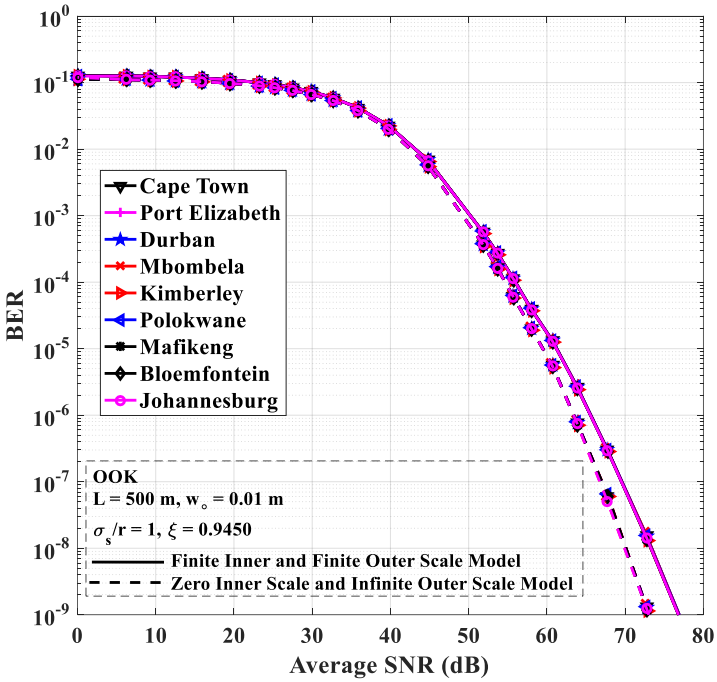

(d) Values not exceeded 99.99% of the time

Figure 4.6: BER of OOK FSOC links vs Average SNR (dB) over weak and moderate to strong atmospheric turbulence channels for various cities in South Africa.

4.8.2 Binary Phase Shift Keying (BPSK) FSO Links

The conditional BER for BPSK SISO FSOC links in the absence of atmospheric turbulence is presented in [57], [64] as:

$$P_{BPSK}\left(e/\gamma\right)=Q\left(\sqrt{\gamma}\right)=0.5erfc\left(\frac{\gamma^{0.5}}{\sqrt{2}}\right) \tag{4.73}$$

1) Weak Atmospheric Turbulence

Inserting (4.51) and (4.73) into (4.56) yields the expression for the BER of BPSK SISO FSOC links in the presence of weak atmospheric turbulence and pointing errors:

$$P_{BPSK}=\int_0^{\infty}\left(0.5erfc\left(\frac{\gamma^{0.5}}{\sqrt{2}}\right)\bullet\frac{\xi^2}{\left(A_o\right)^{\xi^2}}\frac{\gamma^{\left(0.5\xi^2\right)-1}}{\bar{\gamma}^{0.5\xi^2}}\frac{\exp\left(q\right)}{\sqrt{\pi}}\bullet\left[\frac{1}{12}\exp\left(-\left(\frac{0.5In\left(\frac{\gamma}{\bar{\gamma}A_o^2}\right)+p}{4\sigma_{SI}}\right)^2\right)+\frac{1}{4}\exp\left(-\left(\frac{2In\left(\frac{\gamma}{\bar{\gamma}A_o^2}\right)+4p}{9\sigma_{SI}}\right)^2\right)\right]\right)d\gamma \tag{4.74}$$

Further simplification of (4.74), by substituting (4.59)-(4.64) into it, gives an expression in the form:

$$\begin{aligned}P_{BPSK}=&\int_0^{\infty}\left(\frac{\xi^2\sigma_{SI}\exp(q)}{3\sqrt{\pi}}\left(\left(\exp\left(8z_1\sigma_{SI}-2p\right)\right)^{\left(0.5\xi^2\right)}\bullet erfc\left(\frac{\sqrt{\bar{\gamma}A_o^2\exp\left(8z_1\sigma_{SI}-2p\right)}}{\sqrt{2}}\right)\right)\bullet\exp\left(-z_1^2\right)\right)dz_1\\&+\\&\int_0^{\infty}\left(\frac{9\xi^2\sigma_{SI}\exp(q)}{16\sqrt{\pi}}\left(\left(\exp\left(4.5z_2\sigma_{SI}-2p\right)\right)^{\left(0.5\xi^2\right)}\bullet erfc\left(\frac{\sqrt{\bar{\gamma}A_o^2\exp\left(4.5z_2\sigma_{SI}-2p\right)}}{\sqrt{2}}\right)\right)\bullet\exp\left(-z_2^2\right)\right)dz_2\end{aligned} \tag{4.75}$$

Therefore, evaluating (4.75) using the Gauss-Hermite quadrature approximation in (4.66) yields the BER of BPSK SISO FSOC links in the presence of weak atmospheric turbulence and pointing errors:

$$P_{BPSK}=\frac{\xi^2\sigma_{SI}\exp(q)}{2\sqrt{\pi}}\bullet\left(\begin{array}{c}\left(\frac{1}{3}\sum_{i=1}^{N}W_i\left(\left(\exp\left(8z_1\sigma_{SI}-2p\right)\right)^{\left(0.5\xi^2\right)}\bullet erfc\left(\frac{\sqrt{\bar{\gamma}A_o^2\exp\left(8z_1\sigma_{SI}-2p\right)}}{\sqrt{2}}\right)\right)\right)\\+\\\left(\frac{9}{16}\sum_{i=1}^{N}W_i\left(\left(\exp\left(4.5z_2\sigma_{SI}-2p\right)\right)^{\left(0.5\xi^2\right)}\bullet erfc\left(\frac{\sqrt{\bar{\gamma}A_o^2\exp\left(4.5z_2\sigma_{SI}-2p\right)}}{\sqrt{2}}\right)\right)\right)\end{array}\right) \tag{4.76}$$

where the values of the weights, W_i, and zeros of the Hermite polynomial, z_i, are given in [62], [63].

2) Moderate to Strong Atmospheric Turbulence

The conditional BER for BPSK SISO FSOC links in terms of the Meijer G function and in the absence of atmospheric turbulence is presented in [65] as:

$$P_{BPSK}(e|\gamma)=\frac{0.5}{\pi^{0.5}}G_{1,2}^{2,0}\left[0.5\gamma\left|\begin{matrix}1\\0,0.5\end{matrix}\right.\right] \tag{4.77}$$

Substituting (4.52) and (4.77) into (4.56) gives:

$$P_{BPSK}=\frac{\xi^2}{4\Gamma(\alpha)\Gamma(\beta)\pi^{0.5}}\bullet\int_0^{\infty}\gamma^{-1}\bullet G_{1,2}^{2,0}\left[0.5\gamma\left|\begin{matrix}1\\0,0.5\end{matrix}\right.\right]\bullet G_{1,3}^{3,0}\left[\frac{\alpha\beta\xi^2}{\xi^2+1}\left(\frac{\gamma}{\bar{\gamma}}\right)^{0.5}\left|\begin{matrix}\xi^2+1\\\xi^2,\alpha,\beta\end{matrix}\right.\right]d\gamma \tag{4.78}$$

Applying equation (07.34.21.0013.01) in [53] to evaluate (4.78) yields:

$$P_{BPSK}=\frac{\xi^2 2^{\alpha+\beta-4}}{\pi^{1.5}\Gamma(\alpha)\Gamma(\beta)}G_{4,7}^{6,2}\left[\left(\frac{\alpha\beta\xi^2}{\xi^2+1}\right)^2\frac{1}{8\bar{\gamma}}\left|\begin{matrix}1,0.5,\frac{\xi^2+1}{2},\frac{\xi^2+2}{2}\\\frac{\xi^2}{2},\frac{\xi^2+1}{2},\frac{\alpha}{2},\frac{\alpha+1}{2},\frac{\beta}{2},\frac{\beta+1}{2},0\end{matrix}\right.\right] \tag{4.79}$$

The BERs estimated for the zero inner scale and infinite outer scale model and finite inner and finite outer scale model for different receive SNRs are presented in Figures 4.7(a), (b), (c), and (d), and are based on the numerical values in Tables 4.2, 4.3, 4.4, and 4.5, respectively. Equations (4.1)-(4.3), (4.15), (4.35), (4.38), (4.40), (4.41), (4.46), and (4.76) are employed for plotting the BER results of the FSOC links deployed in all the cities in Figure 4.7(b)-(d), while Figure 4.7(a) is computed using (4.1)-(4.3), (4.15), (4.30), (4.31), (4.35), (4.46), and (4.79). Figures 4.7(a)-(d) also show that the presence of finite microscale and macroscale eddies result in poorer BER performances when compared with instances when those eddies have sizes of zero and infinity in the Kolmogorov model with infinitely large inertial range.

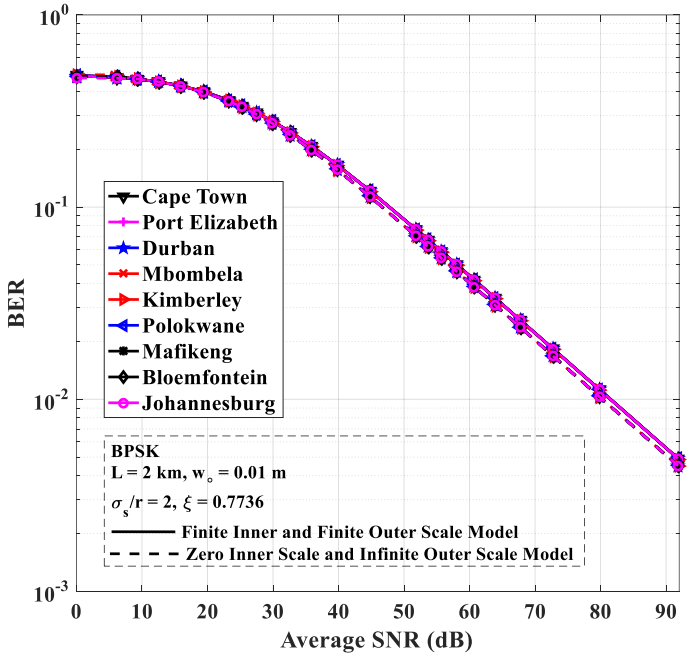

(a) Average values

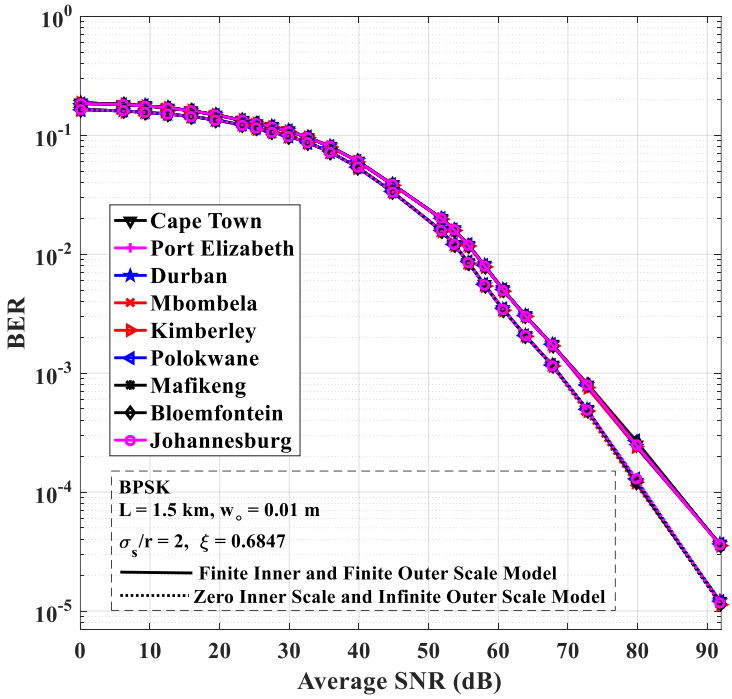

(b) Values not exceeded 99% of the time

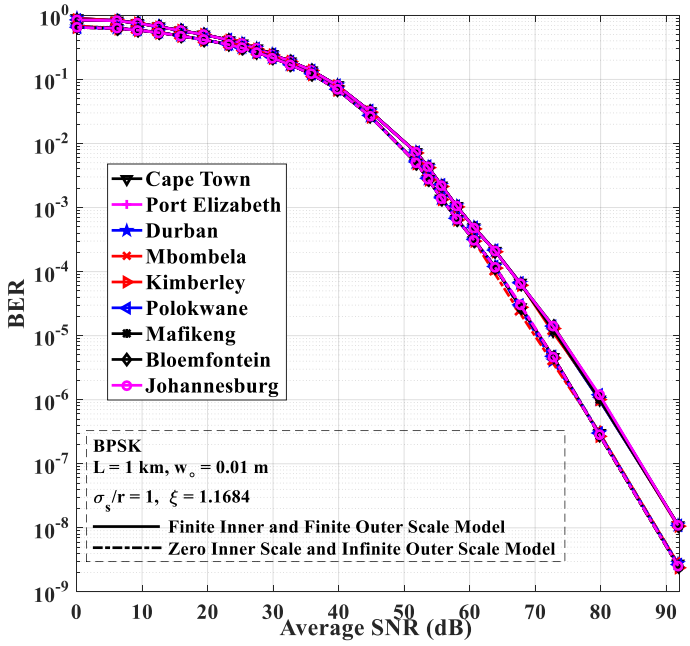

(c) Values not exceeded 99.9% of the time

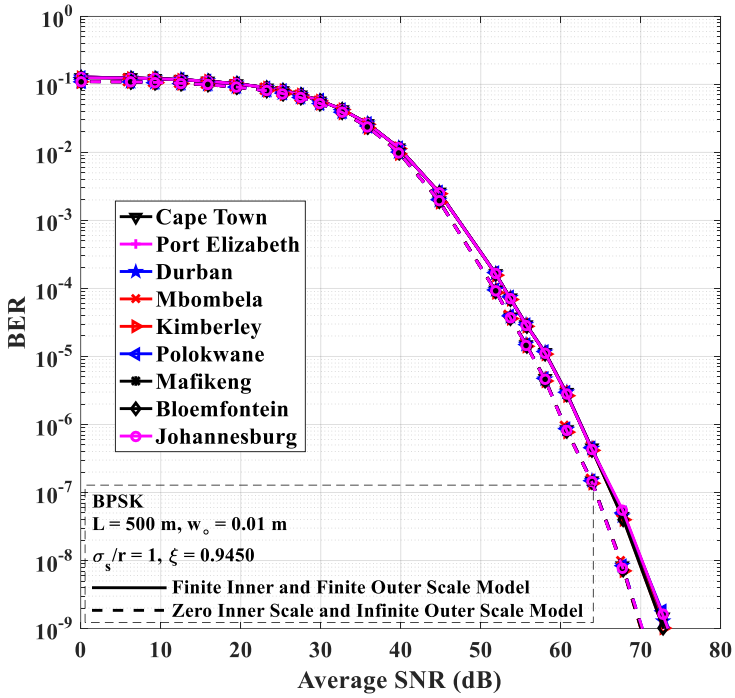

(d) Values not exceeded 99.99% of the time

Figure 4.7: BER of BPSK FSOC links vs average SNR (dB) over weak and moderate to strong atmospheric turbulence channels for various cities in South Africa.

In order to obtain a BER of 10^{-2} over a link distance of 2 km for FSOC links in all the cities investigated, receive SNRs of ~84 and ~81 dB are required based on the finite inner and finite outer scale model in Figures 4.6(a) and 4.7(a), respectively. The BPSK FSOC links investigated in Figures 4.7(a)-(d) generally outperform the OOK FSOC links in Figures 4.6(a)-(d).

4.8.3 Quadrature Amplitude Modulation (SIM-QAM) FSOC Links

4.8.3.1 M-ary Square SIM-QAM FSOC Links

The conditional probability of error for M-ary square SIM-QAM signals in the absence of atmospheric turbulence as derived in [64], [66] is given as:

$$P_{MQAM}\left(e/\gamma\right)=\left(\frac{\sqrt{M}-1}{\sqrt{M}\log_2\sqrt{M}}\right)erfc\left(\sqrt{\frac{3\gamma\log_2 M}{2\left(M-1\right)}}\right) \tag{4.80}$$

where M is the even number of bits per symbol for square constellations.

1) Weak Atmospheric Turbulence

Similar to the previous computations of the BER expressions of RZ-OOK and BPSK modulated signals, substituting (4.53), (4.59)-(4.64), and (4.80) into (4.56) gives:

$$P_{MQAM}=\left(\frac{2\xi^2\sigma_{SI}\exp(q)}{\sqrt{\pi}}\bullet\frac{\sqrt{M}-1}{\sqrt{M}\log_2\sqrt{M}}\right)\times \left(\int_0^{\infty}\left(\frac{1}{3}\left(\left(\exp\left(8z_1\sigma_{SI}-2p\right)\right)^{\left(0.5\xi^2\right)}\bullet erfc\left(\sqrt{\frac{3\log_2(M)\bullet\bar{\gamma}A_o^2\exp\left(8z_1\sigma_{SI}-2p\right)}{2(M-1)}}\right)\right)\bullet\exp\left(-z_1^2\right)\right)dz_1 + \int_0^{\infty}\left(\frac{9}{16}\left(\left(\exp\left(4.5z_2\sigma_{SI}-2p\right)\right)^{\left(0.5\xi^2\right)}\bullet erfc\left(\sqrt{\frac{3\log_2(M)\bullet\bar{\gamma}A_o^2\exp\left(4.5z_1\sigma_{SI}-2p\right)}{2(M-1)}}\right)\right)\bullet\exp\left(-z_2^2\right)\right)dz_2\right) \tag{4.81}$$

where further similar mathematical calculations produce the expression for the BER of M-ary square SIM-QAM SISO FSOC links in the presence of weak atmospheric turbulence and pointing errors:

$$P_{MQAM}=\left(\frac{\xi^2\sigma_{SI}\exp(q)}{\sqrt{\pi}}\bullet\frac{\sqrt{M}-1}{\sqrt{M}\log_2\sqrt{M}}\right)\times \left(\left(\frac{1}{3}\sum_{i=1}^{N}W_i\left(\left(\exp\left(8z_1\sigma_{SI}-2p\right)\right)^{\left(0.5\xi^2\right)}\bullet erfc\left(\sqrt{\frac{3\log_2(M)\bullet\bar{\gamma}A_o^2\exp\left(8z_1\sigma_{SI}-2p\right)}{2(M-1)}}\right)\right)\right) + \left(\frac{9}{16}\sum_{i=1}^{N}W_i\left(\left(\exp\left(4.5z_2\sigma_{SI}-2p\right)\right)^{\left(0.5\xi^2\right)}\bullet erfc\left(\sqrt{\frac{3\log_2(M)\bullet\bar{\gamma}A_o^2\exp\left(4.5z_1\sigma_{SI}-2p\right)}{2(M-1)}}\right)\right)\right)\right) \tag{4.82}$$

2) Moderate to Strong Atmospheric Turbulence

The average BER for M-ary Square SIM-QAM SISO FSOC links in the presence of moderate to strong atmospheric turbulence, while taking in account the effect of pointing errors, is derived in [67] as:

$$P_{MQAM}=\frac{\xi^2 2^{\alpha+\beta-3}}{\pi^{1.5}\Gamma(\alpha)\Gamma(\beta)}\left(\frac{\sqrt{M}-1}{\sqrt{M}\log_2\sqrt{M}}\right)G_{3,6}^{5,2}\left[\left(\frac{\alpha\beta\xi^2}{\xi^2+1}\right)^2\frac{(M-1)}{24\bar{\gamma}\log_2 M}\middle|\begin{matrix}1,0.5,\frac{\xi^2+2}{2}\\ \frac{\xi^2}{2},\frac{\alpha}{2},\frac{\alpha+1}{2},\frac{\beta}{2},\frac{\beta+1}{2},0\end{matrix}\right] \tag{4.83}$$

Equations (4.1)-(4.3), (4.15), (4.35), (4.38), (4.40), (4.41), (4.46), and (4.82) are used in plotting the BER results for the FSOC links in all the investigated cities based on the zero inner scale and infinite outer scale model and finite inner and finite outer scale model for different receive SNRs in Figures 4.8(b)-(d). The results in Figure 4.8(a) are generated using Equations (4.1)-(4.3), (4.15), (4.30), (4.31), (4.35), (4.46), and (4.83). Additionally, the numerical values in Tables 4.2-4.5 determine the BERs for the SIM 16-QAM FSOC links in Figures 4.8(a)-(d).

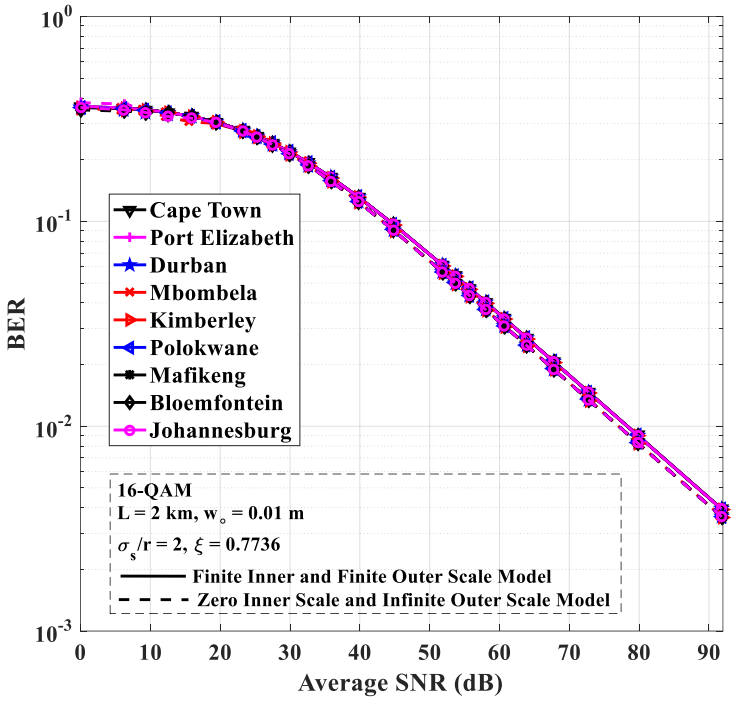

(a) Average values

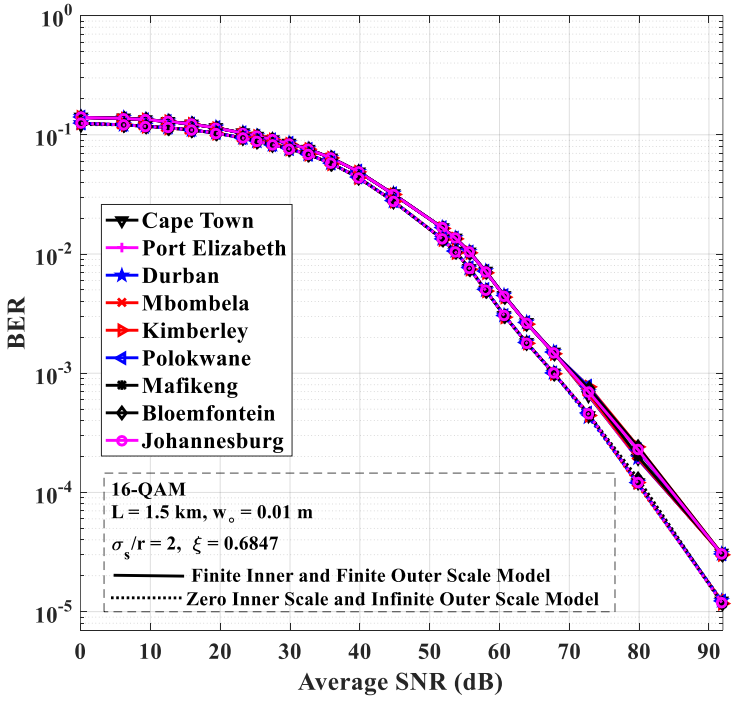

(b) Values not exceeded 99% of the time

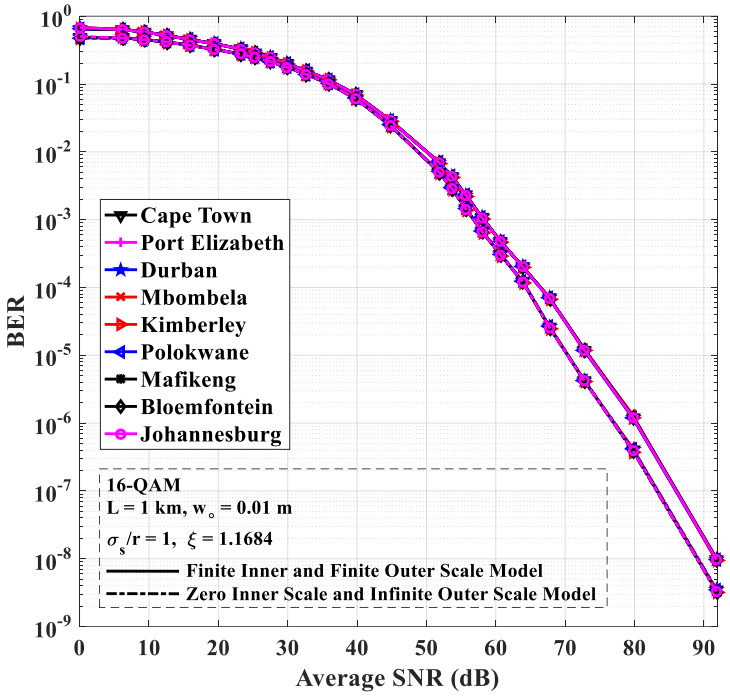

(c) Values not exceeded 99.9% of the time

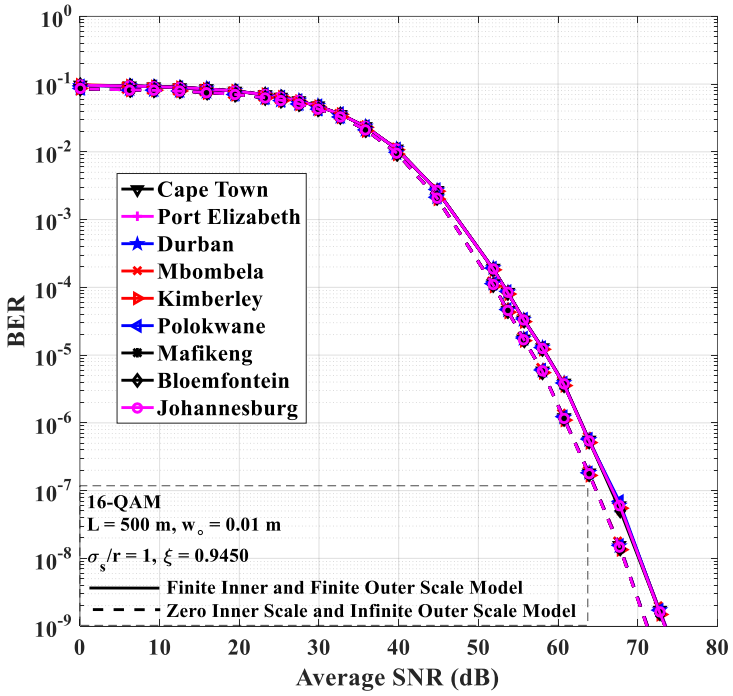

(d) Values not exceeded 99.99% of the time

Figure 4.8: BER of SIM 16-QAM FSOC links vs average SNR (dB) over weak and moderate to strong atmospheric turbulence channels for various cities in South Africa.

In the instance when turbulence eddies have sizes of zero and infinity in the Kolmogorov model with infinitely large inertial range, receive SNRs of ~70 dB are required to obtain a BER of 10^{-5} for 16-QAM FSOC links deployed in all the investigated cities, over a link distance of 1 km, as shown in Figure 4.8(c). The BERs of 16-QAM FSOC links in Figures 4.8(a)-(d) surpass the BER results of conventional OOK FSOC links in Figures 4.6(a)-(d).

4.8.3.2 I × J Rectangular QAM FSOC Links

The conditional probability of error for I × J rectangular SIM-QAM signals in the absence of atmospheric turbulence is given in [66] as:

$$P_{(I\times J)QAM}\left(e/\gamma\right)=\frac{1}{\log_2\left(I\bullet J\right)}\left(\frac{I-1}{I}erfc\left(\sqrt{\frac{3\gamma\log_2\left(I\bullet J\right)}{I^2+J^2-2}}\right)+\frac{J-1}{J}erfc\left(\sqrt{\frac{3\gamma\log_2\left(I\bullet J\right)}{I^2+J^2-2}}\right)\right) \tag{4.84}$$

where I and J are the dimensions of the in-phase and quadrature signals [24], [66].

1) Weak Atmospheric Turbulence

Similarly, inserting (4.53), (4.59)-(4.64), and (4.84) into (4.56) gives:

$$\begin{aligned}P_{(I\times J)QAM}=&\frac{2\xi^2\sigma_{SI}\exp(q)}{\sqrt{\pi}\log_2\left(I\bullet J\right)}\bullet\left(\left(\frac{I-1}{I}\right)+\left(\frac{J-1}{J}\right)\right)\times\\&\left(\int_0^\infty\left(\frac{1}{3}\left(\left(\exp\left(8z_1\sigma_{SI}-2p\right)\right)^{\left(0.5\xi^2\right)}\bullet erfc\left(\sqrt{\frac{3\bar{\gamma}A_o^2\exp\left(8z_1\sigma_{SI}-2p\right)\bullet\log_2\left(I\bullet J\right)}{I^2+J^2-2}}\right)\right)\bullet\exp\left(-z_1^2\right)\right)dz_1\right.\\&+\\&\left.\int_0^\infty\left(\frac{9}{16}\left(\left(\exp\left(4.5z_2\sigma_{SI}-2p\right)\right)^{\left(0.5\xi^2\right)}\bullet erfc\left(\sqrt{\frac{3\bar{\gamma}A_o^2\exp\left(4.5z_1\sigma_{SI}-2p\right)\bullet\log_2\left(I\bullet J\right)}{I^2+J^2-2}}\right)\right)\bullet\exp\left(-z_2^2\right)\right)dz_2\right)\end{aligned} \tag{4.85}$$

Employing the Gauss-Hermite quadrature approximation in (4.66) to evaluate (4.85) generates the expression for the BER of I × J rectangular SIM-QAM SISO FSOC links in the presence of weak atmospheric turbulence and pointing errors:

$$\begin{aligned}P_{(I\times J)QAM}=&\frac{2\xi^2\sigma_{SI}\exp(q)}{\sqrt{\pi}\log_2\left(I\bullet J\right)}\bullet\left(\left(\frac{I-1}{I}\right)+\left(\frac{J-1}{J}\right)\right)\times\\&\left(\left(\frac{1}{3}\sum_{i=1}^{N}W_i\left(\left(\exp\left(8z_1\sigma_{SI}-2p\right)\right)^{\left(0.5\xi^2\right)}\bullet erfc\left(\sqrt{\frac{3\bar{\gamma}A_o^2\exp\left(8z_1\sigma_{SI}-2p\right)\bullet\log_2\left(I\bullet J\right)}{I^2+J^2-2}}\right)\right)\right)\right.\\&+\\&\left.\left(\frac{9}{16}\sum_{i=1}^{N}W_i\left(\left(\exp\left(4.5z_2\sigma_{SI}-2p\right)\right)^{\left(0.5\xi^2\right)}\bullet erfc\left(\sqrt{\frac{3\bar{\gamma}A_o^2\exp\left(4.5z_1\sigma_{SI}-2p\right)\bullet\log_2\left(I\bullet J\right)}{I^2+J^2-2}}\right)\right)\right)\end{aligned} \tag{4.86}$$

2) Moderate to Strong Atmospheric Turbulence

The average BER for I × J Rectangular SIM-QAM SISO FSOC links in the presence of moderate to strong atmospheric turbulence while considering the effect pointing errors is presented in [67] as:

$$P_{(I\times J)QAM}=\frac{\xi^2 2^{\alpha+\beta-3}}{\pi^{1.5}\Gamma(\alpha)\Gamma(\beta)}\frac{1}{\log_2(I\bullet J)}\left(\frac{I-1}{I}+\frac{J-1}{J}\right)G_{3,6}^{5,2}\left[\left(\frac{\alpha\beta\xi^2}{\xi^2+1}\right)^2\frac{\left(I^2+J^2-2\right)}{48\bar{\gamma}\log_2(I\bullet J)}\middle|\begin{matrix}1,0.5,\frac{\xi^2+2}{2}\\ \frac{\xi^2}{2},\frac{\alpha}{2},\frac{\alpha+1}{2},\frac{\beta}{2},\frac{\beta+1}{2},0\end{matrix}\right] \tag{4.87}$$

The BER performance of SIM rectangular 8 x 4 or 32-QAM FSOC links is presented for zero inner scale and infinite outer scale model and finite inner and finite outer scale model for different receive SNRs in Figures 4.9(a)-(d). In Figures 4.9(b)-(d), the BER results of the FSOC links deployed in all the investigated cities are plotted using (4.1)-(4.3), (4.15), (4.35), (4.38), (4.40), (4.41), (4.46), and (4.86), while the BER results in Figure 4.9(a) are computed using (4.1)-(4.3), (4.15), (4.30), (4.31), (4.35), (4.46), and (4.87). Similarly, the results in Figures 4.9(a), (b), (c), and (d) are based on the numerical values in Tables 4.2, 4.3, 4.4, and 4.5, respectively. As expected, the BER performance of SIM 32-QAM FSOC links is poorer than SIM 16-QAM FSOC links in Figures 4.8(a)-(d), but the 32-QAM links transmits a greater amount of information. Additionally, when turbulence eddies have sizes of zero and infinity in the Kolmogorov model with an infinitely large inertial range, the BERs have better performances based on the zero inner scale and infinite outer scale model, as shown in Figures 4.9(a)-(d).

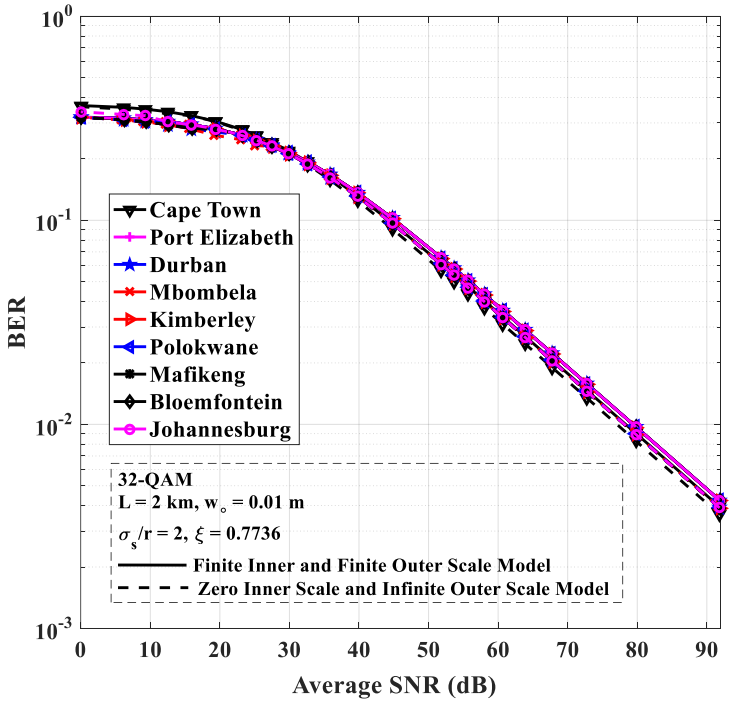

(a) Average values

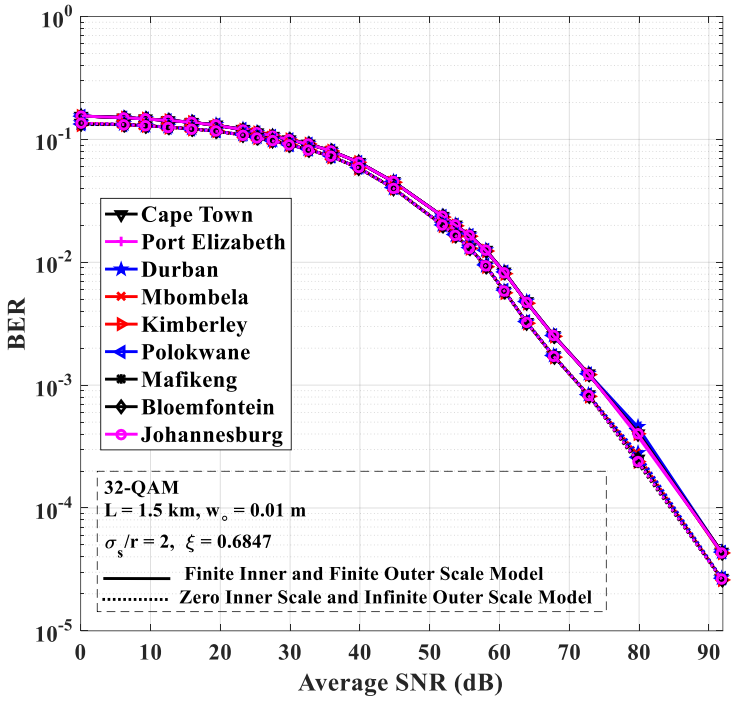

(b) Values not exceeded 99% of the time

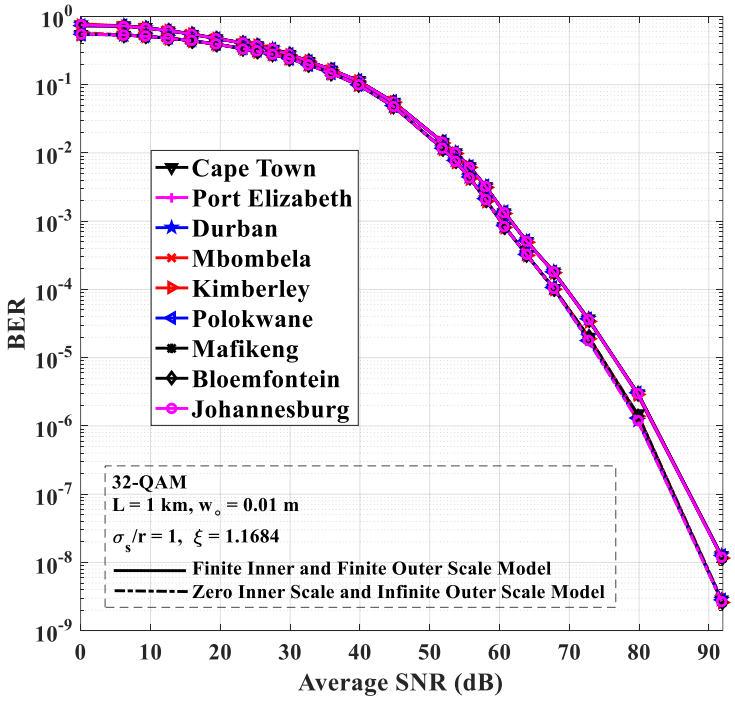

(c) Values not exceeded 99.9% of the time

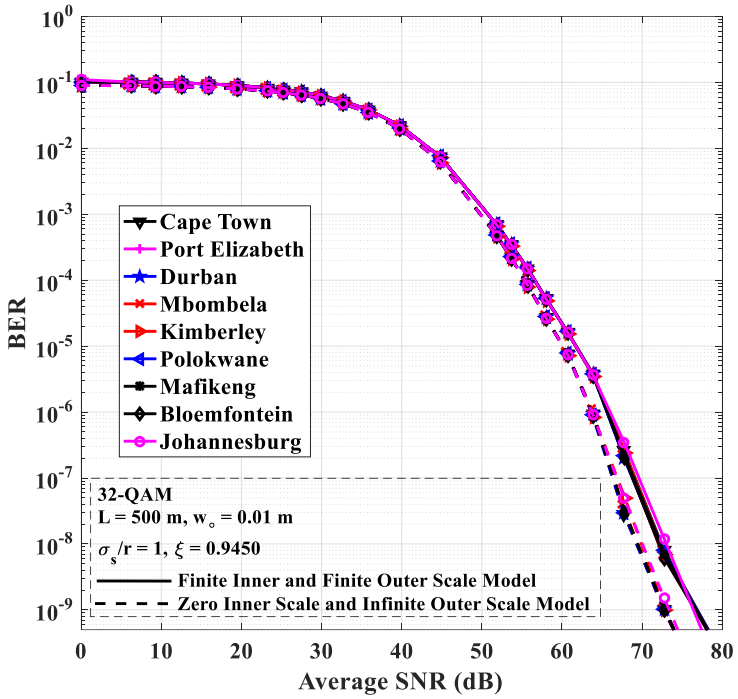

(d) Values not exceeded 99.99% of the time

Figure 4.9: BER of 32-QAM FSOC links vs average SNR (dB) over weak and moderate to strong atmospheric turbulence channels for various cities in South Africa.

4.9 Conclusion

In this paper, analysis of atmospheric turbulence effects on terrestrial SISO FSOC links based on the RMS and ground wind speeds prevalent in various cities of South Africa are presented. Wind speed data provided by the SAWS were statistically processed and the corresponding CDF, PDF, and percentage of time plots are shown for each location of interest. The C_n^2 based on RMS wind speeds during clear and sunny weather are computed. The scintillation indices not exceeded 50%, 99%, 99.9%, and 99.99% of the time, based on the zero inner scale and infinite outer scale model and finite inner and finite outer scale model are calculated. Aerosol scattering losses based on visibilities not exceeded 50%, 99%, 99.9%, and 99.99% of the time for the various cities of South Africa are shown. Outage probability and BER analysis, taking into account the effect of pointing errors over weak and moderate to strong atmospheric turbulence channels, were then carried out for OOK, BPSK, and SIM-QAM SISO FSOC links deployed at the different locations of interest. All through Figures 4.5 to 4.9, the SISO FSOC links deployed in all the locations of interest have similar outage probability and BER performances based on the zero inner scale and infinite outer scale

model and finite inner and finite outer scale model. This is because the values of C_n^2 in all the investigated cities are approximately equivalent over all the time intervals (Table 4.2-4.5) considered in this work. As part of future work, all the analytical results in this work would be verified experimentally. The C_n^2 based on important meteorological parameters such as temperature, pressure, and the structure parameter for temperature, as well as three-dimensional pointing errors effects, will also be investigated for FSOC links deployed in the locations of interest.

References

[1] I. T. U., "Detailed specifications of the terrestrial radio interfaces of International Mobile Telecommunications-2020 (IMT-2020)," *Recommendation ITU-R M.2150-0,* M Series, pp. 1-253, February 2021. [Online]. Available: https://www.itu.int/rec/R-REC-M.2150-0-202102-I/en

[2] O. O. Erunkulu, A. M. Zungeru, C. K. Lebekwe, M. Mosalaosi, and J. M. Chuma, "5G mobile communication applications: a survey and comparison of use cases," *IEEE Access,* vol. 9, pp. 97251-97295, July 2021. DOI: 10.1109/ACCESS.2021.3093213.

[3] I. Rasheed, and F. Hu, "Intelligent super-fast Vehicle-to-Everything 5G communications with predictive switching between mmWave and THz links," *Vehicular Communications,* vol. 27, no. 100303, pp. 1 - 12, Jan. 2021. DOI: 10.1016/j.vehcom.2020.100303.

[4] Y. B. Lin, C. C. Tseng, and M. H. Wang, "Effects of transport network slicing on 5G applications," *MDPI Future Internet,* vol. 13, no. 3, pp. 1 - 17, March 2021. DOI: 10.3390/fi13030069.

[5] Y. Siriwardhana, P. Porambage, M. Liyanage, and M. Ylianttila, "A Survey on Mobile Augmented Reality With 5G Mobile Edge Computing: Architectures, Applications, and Technical Aspects," *IEEE Communications Surveys & Tutorials,* vol. 23, no. 2, pp. 1160-1192, Feb.2021. DOI: 10.1109/COMST.2021.3061981.

[6] S. Malik, and P. K. Sahu, "Free space optics/millimeter-wave based vertical and horizontal terrestrial backhaul network for 5G," *Optics Communications,* vol. 459, no. 125010, pp. 1 - 29, March 2020. DOI: 10.1016/j.optcom.2019.125010.

[7] V. Palliyembil, J. Vellakudiyan, and P. Muthuchidambaranathan, "Performance analysis of RF-FSO communication systems over the Málaga distribution channel with pointing error," *Optik - International Journal for Light and Electron Optics,* vol. 247, no. 167891, pp. 1 - 11, Sept. 2021. DOI: 10.1016/j.ijleo.2021.167891.

[8] M. Garlinska, A. Pregowska, K. Masztalerz, and M. Osial, "From mirrors to free-space optical communication—historical aspects in data transmission," *Future Internet,* vol. 12, no. 11, pp. 1-18, 22 Oct. 2020. DOI: 10.3390/fi12110179.

[9] O. Kolawole, T. Afullo, and M. Mosalaosi, "Estimation of Optical Wireless Communication Link Availability Using Meteorological Visibility Data for Major Locations in South Africa," in *2019 PhotonIcs & Electromagnetics Research Symposium-Spring (PIERS-Spring)*, Rome, Italy, 2019, pp. 319-325. DOI: 10.1109/PIERS-Spring46901.2019.9017842.

[10] O. O. Kolawole, T. J. O. Afullo, M. Mosalaosi, "Initial Modeling of Atmospheric Turbulence Effect on Optical Wireless Communication Links in South Africa," in *Southern Africa Telecommunication Networks and Applications Conference (SATNAC) 2019*, Ballito, KwaZulu-

Natal, South Africa, Sept. 1-4, 2019, pp. 68 - 72. [Online]. Available: https://www.researchgate.net/publication/354747988_Initial_Modeling_of_Atmospheric_Turbulence_Effect_on_Optical_Wireless_Communication_Links_in_South_Africa

[11] O. O. Kolawole, T. J. O. Afullo, P. A. Owolawi, "Performance Analysis of Cross M-QAM over Weak Atmospheric Turbulence Channel," in *Southern Africa Telecommunication Networks and Applications Conference (SATNAC) 2016*, George, Western Cape, South Africa, Sept. 4-7, 2016, pp. 80 - 84. [Online]. Available: https://www.researchgate.net/publication/354749030_Performance_Analysis_of_Cross_M-QAM_over_Weak_Atmospheric_Turbulence_Channel

[12] L. Dordová, and O. Wilfert, "Calculation and comparison of turbulence attenuation by different methods," *Radioengineering*, vol. 19, no. 1, pp. 162-167, 2010. [Online]. Available: https://www.radioeng.cz/fulltexts/2010/10_01_162_167.pdf

[13] D. Dubey, Y. K. Prajapati and R. Tripathi, "Error performance analysis of PPM-and FSK-based hybrid modulation scheme for FSO satellite downlink," *Optical and Quantum Electronics*, vol. 52, no. 286, pp. 1-16, May 2020. DOI: 10.1007/s11082-020-02404-7.

[14] H. AlQuwaiee, H. Yang and M. Alouini, "On the Asymptotic Capacity of Dual-Aperture FSO Systems With Generalized Pointing Error Model," *IEEE Transactions on Wireless Communications*, vol. 15, no. 9, pp. 6502-6512, Sept. 2016. DOI: 10.1109/TWC.2016.2585486.

[15] D. K. Borah and D. G. Voelz, "Pointing Error Effects on Free-Space Optical Communication Links in the Presence of Atmospheric Turbulence," *Journal of Lightwave Technology*, vol. 27, no. 18, pp. 3965-3973, Sept.15, 2009. DOI: 10.1109/JLT.2009.2022771.

[16] D. Dubey, Y. K. Prajapati, R. Tripathi, "Optimization of hybrid high-throughput MIMO system with misaligned FSO link under varied weather," *Optical Engineering*, vol. 60, no. 8, pp. 1-20, Aug. 23, 2021. DOI: 10.1117/1.OE.60.8.086106.

[17] A. A. Farid and S. Hranilovic, "Outage Capacity Optimization for Free-Space Optical Links With Pointing Errors," *Journal of Lightwave Technology*, vol. 25, no. 7, pp. 1702-1710, July 2007. DOI: 10.1109/JLT.2007.899174.

[18] H. D. Trung, D. T. Tuan, and A. T. Pham, "Pointing error effects on performance of free-space optical communication systems using SC-QAM signals over atmospheric turbulence channels," *AEU - International Journal of Electronics and Communications*, vol. 68, no. 9, pp. 869-876, Sept. 2014. DOI: 10.1016/j.aeue.2014.04.008.

[19] R. B. Ruiz, A. G. Zambrana, B. C. Vázquez, and C. C. Vázquez, "Impact of nonzero boresight pointing error on ergodic capacity of MIMO FSO communication systems," *Opt. Express*, vol. 24, no.4, pp. 3513-3534, Feb. 2016. DOI: 10.1364/OE.24.003513

[20] H. Liu, R. Liao, Z. Wei, Z. Hou, and Y. Qiao, "BER analysis of a hybrid modulation scheme based on PPM and MSK subcarrier intensity modulation," *IEEE Photonics Journal*, vol. 7, no. 4, pp. 1-10, Aug. 2015. DOI: 10.1109/JPHOT.2015.2449265

[21] K. Sharma and S. K. Grewal, "Performance assessment of hybrid PPM–BPSK–SIM based FSO communication system using time and wavelength diversity under variant atmospheric turbulence," *Optical and Quantum Electronics*, vol. 52, no. 430, pp. 1-25, Sept. 2020. DOI: 10.1007/s11082-020-02547-7

[22] P. K. Singya, P. Shaik, N. Kumar, V. Bhatia, and M. S. Alouini, "A Survey on Higher-Order QAM Constellations: Technical Challenges, Recent Advances, and Future Trends," *IEEE Open Journal of the Comm. Society*, vol. 2, pp. 617-655, March 2021. DOI: 10.1109/OJCOMS.2021.3067384

[23] B. T. Vu, C. T. Truong, A. T. Pham, and N. T. Dang, "Performance of rectangular QAM/FSO systems using APD receiver over atmospheric turbulence channels," in *TENCON 2012 IEEE Region 10 Conference*, Cebu, Philippines, Nov. 19-22, 2012, pp. 1-5. DOI: 10.1109/TENCON.2012.6412187

[24] B. T. Vu, N. T. Dang, T. C. Thang, and A. T. Pham, "Bit error rate analysis of rectangular QAM/FSO systems using an APD receiver over atmospheric turbulence channels," *Journal of Opt. Comm. and Networking*, vol. 5, no. 5, pp. 437-446, May 2013. DOI: 10.1364/JOCN.5.000437.

[25] D. Sprung, A. M. J. van Eijk, E. Sucher, C. Eisele, D. Seiffer, and K. Stein, "First results on the Experiment FESTER on optical turbulence over False Bay South Africa: dependencies and consequences," in *Proc. SPIE 10002, Optics in Atmospheric Propagation and Adaptive Systems XIX, 1000209*, Edinburgh, United Kingdom, Oct. 19, 2016, pp. 1-9. DOI: 10.1117/12.2240651

[26] D. Sprung, A. M. J. van Eijk, C. Ullwer, W. Gunter, C. Eisele, D. Seiffer, E. Sucher, and K. Stein "Optical turbulence in the coastal area over False Bay, South Africa: comparison of measurements and modeling results", in *Proc. SPIE 10787, Environmental Effects on Light Propagation and Adaptive Systems, 1078703*, Berlin, Germany, Oct. 10, 2018, pp. 1-8. DOI: 10.1117/12.2325609

[27] A. M. Aly, H. A. Fayed, N. E. Ismail, M. H. Aly, "Plane wave scintillation index in slant path atmospheric turbulence: closed form expressions for uplink and downlink," *Optical and Quantum Electronics*, vol. 52, no. 350, pp. 1-14, July 2020. DOI: 10.1007/s11082-020-02463-w

[28] M. Handura, K. Ndjavera, C. Nyirenda, and T. O. Olwal, "Determining the feasibility of free space optical communication in Namibia," *Optics Communications*, vol. 366, pp. 425-430, May 2016. DOI: 10.1016/j.optcom.2015.12.057.

[29] J. Mohale, M. R. Handura, T. O. Olwal, and C. N. Nyirenda, "Feasibility study of free-space optical communication for South Africa," *Optical Engineering*, vol. 55, no. 5, pp. 1-10, May 2016. DOI: 10.1117/1.OE.55.5.056108.

[30] A. Mukherjee, S. Kar, and V. K. Jain, "Analysis of beam wander effect in high turbulence for FSO communication link," *IET Communications*, vol. 12, no. 20, pp. 2533-2537, Aug. 2018. DOI: 10.1049/iet-com.2018.5409

[31] M. Abaza, R. Mesleh, A. Mansour, and el-Hadi Aggoune, "Performance analysis of MISO multi-hop FSO links over log-normal channels with fog and beam divergence attenuations," *Optics Communications*, vol. 334, pp. 247-252, Jan. 2015.

[32] O. O. Kolawole, T. J. Afullo, and M. Mosalaosi, "Initial Estimation of Scintillation Effect on Free Space Optical Links in South Africa," in *2019 IEEE AFRICON*, Accra, Ghana, Sept. 25-27, 2019, pp. 1-6. DOI: 10.1109/AFRICON46755.2019.9134032

[33] K. Shahiduzzaman, M. F. Haider, B. K. Karmaker, and C. Engineering, "Terrestrial free space optical communications in bangladesh: transmission channel characterization," *International Journal of Elect. and Comp. Eng. (IJECE)*, vol. 9, no. 4, pp. 3130-3138, Aug. 2019. DOI: 10.11591/ijece.v9i4.pp3130-3138.

[34] Global Wind Atlas, "Average Wind speed for South Africa," ed, 2021. [Online]. Available: https://globalwindatlas.info/, Accessed on: Sept. 21, 2021

[35] S. Karp, and L.B. Stotts, "Communications in the turbulent channel," in *Fundamentals of electro-optic systems design: communications, LiDAR, and imaging*, Cambridge, UK: Cambridge University Press, 2013, pp. 179-248.

[36] L. B. Stotts, "Optical channel effects," in *Free Space Optical Systems Engineering: Design and Analysis*, Ist ed., New Jersey, USA: John Wiley & Sons, Inc., Hoboken, 2017, pp. 239-295.

[37] L. C. Andrews, R. L. Phillips, R. Crabbs, D. Wayne, T. Leclerc, and P. Sauer, "Atmospheric channel characterization for ORCA testing at NTTR," in *Proceedings of Atmospheric and Oceanic Propagation of Electromagnetic Waves IV, 758809*, San Francisco, California, USA, Feb. 26, 2010, pp. 1-12. DOI: 10.1117/12.842441

[38] L. C. Andrews, and R. L. Phillips, *Laser beam propagation through random media*, 2nd ed. Bellingham, Washington, USA: SPIE press, 2005, pp. 1-773.

[39] L. C. Andrews, *Field guide to atmospheric optics*, 2nd ed. Bellingham, Washington USA: SPIE press, 2004, pp. 1-90.

[40] C. J. Engelbrecht, and F. A. Engelbrecht, "Shifts in Köppen-Geiger climate zones over southern Africa in relation to key global temperature goals," *Theor Appl Climatol*, vol. 123, pp. 247–261, Jan. 2015. DOI: 10.1007/s00704-014-1354-1

[41] P. D. Tyson and R. A. Preston-Whyte, "Atmospheric circulation and weather over southern africa," in *Weather and climate of southern Africa*, 2nd ed. Cape Town, South Africa: Oxford University Press Southern Africa, 2000, ch. 12, pp. 176-217.

[42] O. O. Kolawole, T. J. O. Afullo, and M. Mosalaosi, "Terrestrial Free Space Optical Communication Systems Availability based on Meteorological Visibility Data for South Africa," in *SAIEE Africa Research Journal*, vol. 113, no. 1, pp. 20-36, March 2022. DOI: 10.23919/SAIEE.2022.9695423.

[43] A. Prokeš, "Modeling of atmospheric turbulence effect on terrestrial FSO link," *Radioengineering*, vol. 18, no. 1, pp. 42-47, April 2009. [Online]. Available: https://core.ac.uk/download/pdf/44395516.pdf

[44] L. C. Andrews, R. L. Phillips, and C. Y. Hopen, *Laser beam scintillation with applications*, 1st ed. Bellingham, Washington USA: SPIE press, 2001, pp. 1-368.

[45] T. D. Katsilieris, G. P. Latsas, H. E. Nistazakis, and G. S. Tombras, "An accurate computational tool for performance estimation of FSO communication links over weak to strong atmospheric turbulent channels," *Computation*, vol. 5, no. 18, pp. 1-16, March 2017. DOI: 10.3390/computation5010018.

[46] J. Recolons, L. C. Andrews, and R. L. Phillips, "Analysis of beam wander effects for a horizontal-path propagating Gaussian-beam wave: focused beam case," *Optical Engineering*, vol. 46, no. 8, pp. 1-11, Aug. 2007. DOI: 10.1117/1.2772263

[47] A. Prokes, "Atmospheric effects on availability of free space optics systems," *Optical Engineering*, vol. 48, no. 6, pp. 1-10, June 2009. DOI: 10.1117/1.3155431

[48] I. I. Kim, B. McArthur, and E. J. Korevaar, "Comparison of laser beam propagation at 785 nm and 1550 nm in fog and haze for optical wireless communications," in *Proc. SPIE 4214, Optical Wireless Communications III*, Feb. 2001, pp. 26-37, DOI: 10.1117/12.417512.

[49] M. Ijaz, "Experimental characterisation and modelling of atmospheric fog and turbulence in FSO," Ph.D. dissertation, Faculty Eng. Env., Northumbria University, Newcastle upon Tyne, UK, 2013.

[50] M. Ijaz, Z. Ghassemlooy, J. Pesek, O. Fiser, H. Le Minh, and E. Bentley, "Modeling of fog and smoke attenuation in free space optical communications link under controlled laboratory conditions," *Journal of Lightwave Technology*, vol. 31, no. 11, pp. 1720-1726, June 2013, DOI: 10.1109/JLT.2013.2257683.

[51] D. A. Luong, T. C. Thang, and A. T. Pham, "Effect of avalanche photodiode and thermal noises on the performance of binary phase-shift keyingsubcarrier-intensity modulation/free-space optical systems over turbulence channels," *IET Communications*, vol. 7, no. 8, pp. 738-744, May 2013. DOI: 10.1049/iet-com.2012.0600.

[52] L. C. Andrews, and R. L. Phillips, *Field guide to probability, random processes, and random data analysis*, 1st ed. Bellingham, Washington USA: SPIE press, 2012, pp. 1-89.

[53] Wolfram Research, Inc., 2008. [Online]. Available: https://functions.wolfram.com/PDF/MeijerG.pdf

[54] L. C. Andrews, *Field guide to special functions for engineers*, 1st ed. Bellingham, Washington USA: SPIE press, 2011, pp. 1-101.

[55] G. T. Djordjevic, M. I. Petkovic, A. M. Cvetkovic and G. K. Karagiannidis, "Mixed RF/FSO Relaying With Outdated Channel State Information," *IEEE Journal on Selected Areas in Communications*, vol. 33, no. 9, pp. 1935-1948, Sept. 2015. DOI: 10.1109/JSAC.2015.2433055.

[56] J. Feng, and X. Zhao, "Performance analysis of OOK-based FSO systems in Gamma–Gamma turbulence with imprecise channel models," *Optics Communications*, vol. 402, pp. 340-348, Nov. 2017. DOI: 10.1016/j.optcom.2017.06.016.

[57] X. Song, F. Yang and J. Cheng, "Subcarrier BPSK modulated FSO communications with pointing errors," *2013 IEEE Wireless Communications and Networking Conference (WCNC)*, 2013, pp. 4261-4265, DOI: 10.1109/WCNC.2013.6555262.

[58] T. Ismail and E. Leitgeb, "Performance analysis of SIM-DPSK FSO system over lognormal fading with pointing errors," *2016 18th International Conference on Transparent Optical Networks (ICTON)*, 2016, pp. 1-4, DOI: 10.1109/ICTON.2016.7550350.

[59] M. I. Petković, G. T. Đorđević, and D. N. Milić, "Average BER performance of SIM-DPSK FSO system with APD receiver," *Automatic Control, and Robotics*, vol. 14, no. 2, pp. 111-121, June 2015. [Online]. Available: http://casopisi.junis.ni.ac.rs/index.php/FUAutContRob/article/download/1092/768

[60] M. I. Petković, G. T. Đorđević, and D. N. Milić, "BER performance of IM/DD FSO system with OOK using APD receiver," *Radioengineering*, vol. 23, no. 1, pp. 480-487, April 2014. [Online]. Available: https://www.radioeng.cz/fulltexts/2014/14_01_0480_0487.pdf

[61] E. Zedini, I. S. Ansari, and M. S. Alouini, "Performance Analysis of Mixed Nakagami-m and Gamma–Gamma Dual-Hop FSO Transmission Systems," *IEEE Photonics Journal*, vol. 7, no. 1, pp. 1-20, Dec. 2014. DOI: 10.1109/JPHOT.2014.2381657.

[62] M. Abramowitz and I. A. Stegun, *Handbook of mathematical functions with formulas, graphs, and mathematical tables*. vol. 55: US Government printing office, Washington, DC, USA, 1964.

[63] F. Scheid, *Schaum's outline of theory and problems of numerical analysis*: McGraw-Hill, 1988.

[64] A. Mishra and R. K. Giri, "Performance Analysis Of Different Modulation Techniques In SIM Based FSO Using Different Receivers Over Turbulent Channel," *2018 International Conference on Communication, Computing and Internet of Things (IC3IoT)*, 2018, pp. 459-464, DOI: 10.1109/IC3IoT.2018.8668104.

[65] Z. Xu, G. Xu, and Z. Zheng, "BER and Channel Capacity Performance of an FSO Communication System over Atmospheric Turbulence with Different Types of Noise," *Sensors*, vol. 21, no. 3454, pp. 1-14, May 2021. DOI: 10.3390/s21103454.

[66] K. Cho and D. Yoon, "On the general BER expression of one- and two-dimensional amplitude modulations," *IEEE Transactions on Communications*, vol. 50, no. 7, pp. 1074-1080, July 2002. DOI: 10.1109/TCOMM.2002.800818.

[67] G. T. Djordjevic, and M. I. Petkovic, "Average BER performance of FSO SIM-QAM systems in the presence of atmospheric turbulence and pointing errors," *Journal of Modern Optics*, vol. 63, no. 8, pp. 715-723, Oct. 2015. DOI: 10.1080/09500340.2015.1093662.

Chapter 5

5 Conclusion

In this chapter, concise summaries of the key research contributions and outcomes provided in this thesis are presented. The integration, implications, and significance of the results with respect to the research objectives are also clearly stated. Further recommendations for future work are highlighted.

5.1 Thesis Conclusion

In chapter 2, regression analysis was used to illustrate the modeling of visibility. It was demonstrated that meteorological parameters at a given location may be utilized to model and possibly forecast optical signal visibility. All of the models provided have an excellent agreement with the measured data, as shown in the results obtained. The significance of model parameters was improved in the multiple regression models by mitigating the effects of multicollinearity. The model's selection may be influenced not only by its performance but also by the parameters' availability. In circumstances where a single meteorological parameter is accurately measured over a lengthy period of time in the absence of others, SLR models can be employed. Otherwise, MLR models should be used to account for all of the different constructs that each parameter specifies. To avoid model over-specification, caution should be exercised when there are too many parameters available. In such circumstances, the fitting method may capture the unique aspects of the data rather than the genuine underlying trend of how visibility varies.

Visibility can be extrapolated from measurement data obtained in regions with comparable weather patterns for locations where measured visibility data is not available. The contributions in Chapter 2 are significant because the regression models presented reliably forecast atmospheric visibility from other meteorological parameters in locations where FSOC links may be deployed. These models provided here are good alternatives for estimating visibility in the absence of optical visibility sensors, transmissiometers, and optical scatterometers, saving costs and avoiding the complexities of measuring FSO visibility in the investigated locations.

The availability analysis of terrestrial FSOC links based on the climatic characteristics of several South African cities is presented in Chapter 3. Using visibility data for the locations of interest, cumulative distributions of aerosol scattering attenuation based on the Kim and Ijaz models were generated. Both models are suitable, experimentally verified, and independent aerosol scattering attenuation models. The

probabilities of exceedance, deceedance, and encountering scattering attenuation for optical wavelengths of 850 and 1550 nm are presented. These transmission wavelengths were selected because they are in the range of wavelengths (800–890 nm and 1550 nm) where optical signals are least susceptible to absorption effects. The results showed that during foggy weather, the optical signals at a wavelength of 1550 nm encounter more scattering attenuation than those transmitted at the 850 nm wavelength. The reverse is the case during clear weather periods. Link budget analysis was done for 850 and 1550 nm FSOC links.

The resulting link margin equations were used to evaluate the minimum required visibilities for these links under foggy and clear weather conditions. Approximate polynomial equations are derived for computing the minimum required visibility CDFs for all cities investigated, and these equations are then used to estimate the availabilities of two commercial FSOC links. In foggy weather conditions, plots of the received SNR and data rate performance are shown. Based on average weather data from various South African cities, BER and link performance plots are presented for two links under the influence of weak atmospheric turbulence.

In terms of all of the performance criteria examined, the FSOC system propagating at 1550 nm outperforms the one transmitting at 850 nm. In terms of link availability, the minimum required visibility needed to attain a certain link distance at 1550 nm is lower when compared with the link transmitting at 850 nm. Hence, the 1550 nm link has a longer optimal link length. Also, optical signals in the short-wavelength IR range (1530–1560 nm) are the dominant spectral region for long-distance telecommunications. This is because of their inherent characteristics of minimal absorption within the IR spectrum. This plays a major role in the better BER performance of the FSOC links transmitting in the short-wavelength infrared range (1530–1560 nm) over weak and moderate to strong atmospheric turbulence regimes as compared to those transmitting in the near IR range (780–1400 nm).

In chapter 4, analysis of atmospheric turbulence effects on terrestrial SISO FSOC links based on the RMS and ground wind speeds peculiar to various cities in South Africa is presented. Wind speed data obtained from the SAWS was statistically analyzed and the corresponding CDF, PDF, and percentage of time plots are shown for each location of interest. The C_n^2 based on RMS wind speeds during clear and sunny weather are calculated using the Hufnagel-Andrews-Phillips (HAP) model. The scintillation indices for Gaussian beam waves were determined based on the zero inner scale and infinite outer scale model and finite inner scale and finite outer scale model for periods not exceeded 50%, 99%, 99.9%, and 99.99% of the time. Aerosol scattering losses based on visibility not exceeding 50%, 99%, 99.9%, and 99.99% of the time for the various cities in South Africa are presented. The scintillation indices and the aerosol scattering losses

were computed for FSOC links transmitting at a wavelength of 1550 nm. The choice of selecting the 1550 nm wavelength, despite the relatively lower cost of optical sources and detectors that operate at wavelengths within the spectral range of 700-1000 nm, is the higher level of eye safety of optical signals on the 1550 nm wavelength compared to optical signals transmitting at near IR wavelengths.

Outage probability and BER analysis are then performed for OOK, BPSK, and SIM-QAM SISO FSOC links deployed at various locations of interest, taking into consideration the influence of misalignment errors under weak and moderate to strong atmospheric turbulence regimes. According to the results obtained, SISO FSOC links deployed to all the locations of interest have similar outage probability and BER performances based on the zero inner scale and infinite outer scale model and finite inner scale and finite outer scale model for transmission wavelengths of 1550 nm. This is because the estimated values of the C_n^2 based on the HAP model in all the locations investigated are approximately equal over all the time intervals considered in this work.

5.2 Recommendations for Future Research

1) Develop empirical models for the accurate estimation of the total attenuation coefficient for OWC links for the locations of interest in this study.

2) Investigate the C_n^2 based on important meteorological parameters such as temperature, pressure, and the structure parameter for temperature for the various cities of South Africa.

3) Investigate the performance of the developed attenuation coefficient models with various machine and deep learning predictive models.

4) Investigate the performance of various line coding schemes such as binary differential phase shift keying (BDPSK), dual polarization quadrature phase shift keying (DP-QPSK), optical orthogonal frequency division multiplexing (O-OFDM) etc. for SISO, single-input multiple-output (SIMO), multiple-input single-output (MISO), multiple-input multiple-output (MIMO) and several hybrid OWC systems while considering misalignment errors using time and wavelength diversity under various atmospheric turbulence regimes.

References

[1] S. Chauhan, R. Miglani, L. Kansal, G. S. Gaba, and M. Masud, "Performance Analysis and Enhancement of Free Space Optical Links for Developing State-of-the-Art Smart City Framework," *Photonics*, vol. 7, no. 4, p. 132, Dec. 2020, DOI: 10.3390/photonics7040132.

[2] M. A. Khalighi and M. Uysal, "Survey on Free Space Optical Communication: A Communication Theory Perspective," *IEEE Communications Surveys & Tutorials*, vol. 16, no. 4, pp. 2231-2258, Fourth quarter 2014, DOI: 10.1109/COMST.2014.2329501.

[3] A. K. Majumdar, *Optical wireless communications for broadband global internet connectivity: fundamentals and potential applications*. 1st ed. Amsterdam, Netherlands: Elsevier, 2018, pp. 1-283.

[4] S. Malik, and P. K. Sahu, "Free space optics/millimeter-wave based vertical and horizontal terrestrial backhaul network for 5G," *Optics Communications*, vol. 459, no. 125010, pp. 1 - 29, March 2020. DOI: 10.1016/j.optcom.2019.125010.

[5] A. T. Pham, P. V. Trinh, V. V. Mai, N. T. Dang and Cong-Thang Truong, "Hybrid free-space optics/millimeter-wave architecture for 5G cellular backhaul networks," *2015 Opto-Electronics and Communications Conference (OECC)*, 2015, pp. 1-3, DOI: 10.1109/OECC.2015.7340269.

[6] A. N. Stassinakis, G. A. Papavgeris, H. E. Nistazakis, A. D. Tsigopoulos, N. A. Androutsos, and G. S. Tombras, "Experimental Model Development for the Attenuation Coefficient Estimation of Terrestrial Optical Wireless Links over the Sea" *Telecom*, vol. 2, no. 1, pp. 93-107, March 2021. DOI: 10.3390/telecom2010007.

[7] M. Garlinska, A. Pregowska, K. Masztalerz, and M. Osial, "From Mirrors to Free-Space Optical Communication—Historical Aspects in Data Transmission," *Future Internet*, vol. 12, no. 11, p. 179, Oct. 2020, DOI: 10.3390/fi12110179.

[8] A. Malik and P. Singh, "Free space optics: current applications and future challenges," *International Journal of Optics*, vol. 2015, Article ID 945483, pp. 1-7, Nov. 2015. DOI: 10.1155/2015/945483.

[9] Z. Ghassemlooy, W. Popoola, and S. Rajbhandari, *Optical wireless communications: system and channel modelling with Matlab®*, 2nd ed. Boca Raton, FL, USA: CRC press, 2019, pp. 1-541.

[10] R. Miglani and J. S. Malhotra, "An innovative approach for performance enhancement of 320 Gbps free space optical communication system over turbulent channel" *Optical Quantum Electronics*, vol. 51, no. 289, pp. 1-26, Aug. 2019. DOI: 10.1007/s11082-019-2004-8.

[11] S. Ghoname, H. A. Fayed, A. A. El Aziz and M. H. Aly, "Performance analysis of FSO communication system: Effects of fog, rain and humidity," *2016 Sixth International Conference on*

Digital Information Processing and Communications (ICDIPC), 2016, pp. 151-155, DOI: 10.1109/ICDIPC.2016.7470809.

[12] F. Nadeem, B. Flecker, E. Leitgeb, M. S. Khan, M. S. Awan and T. Javornik, "Comparing the fog effects on hybrid network using optical wireless and GHz links," *2008 6th International Symposium on Communication Systems, Networks and Digital Signal Processing*, 2008, pp. 278-282, DOI: 10.1109/CSNDSP.2008.4610745.

[13] M. Ijaz, Z. Ghassemlooy, S. Rajbhandari, H. Le Minh, J. Perez and A. Gholami, "Comparison of 830 nm and 1550 nm based free space optical communications link under controlled fog conditions," *2012 8th International Symposium on Communication Systems, Networks & Digital Signal Processing (CSNDSP)*, 2012, pp. 1-5, DOI: 10.1109/CSNDSP.2012.6292739.

[14] A. S. El-Wakeel, N. A. Mohammed, and M. H. Aly, "Free space optical communications system performance under atmospheric scattering and turbulence for 850 and 1550 nm operation," *Appl. Opt.* vol. 55, no. 26, pp. 7276-7286, Sept. 2016. DOI: 10.1364/AO.55.007276.

[15] M. C. Al Naboulsi, H. Sizun, F. de Fornel, "Fog attenuation prediction for optical and infrared waves," *Optical Engineering*, vol. 43, no. 2, pp. 319-329, Feb. 2004. DOI: 10.1117/1.1637611.

[16] E. Ferdinandov, K. Dimitrov, A. Dandarov, and I. Bakalski, "A general model of the atmospheric scattering in the wavelength interval 300–1100 nm," *Radioengineering*, vol. 18, no. 4, pp. 517-521, Dec. 2009. [Online] Available: https://core.ac.uk/download/pdf/44395688.pdf

[17] M. Grabner and V. Kvicera, "Case study of fog attenuation on 830 nm and 1550 nm free-space optical links," *Proceedings of the Fourth European Conference on Antennas and Propagation*, 2010, pp. 1-4.

[18] M. Ijaz, "Experimental characterisation and modelling of atmospheric fog and turbulence in FSO," Ph.D. dissertation, Faculty Eng. Env., Northumbria University, Newcastle upon Tyne, UK, 2013.

[19] I. I. Kim, B. McArthur, and E. J. Korevaar, "Comparison of laser beam propagation at 785 nm and 1550 nm in fog and haze for optical wireless communications," in *Proc. SPIE 4214, Optical Wireless Communications III*, Feb. 2001, pp. 26-37, DOI: 10.1117/12.417512.

[20] F. Nadeem, T. Javornik, E. Leitgeb, V. Kvicera, and G. Kandus, "Continental fog attenuation empirical relationship from measured visibility data," *Radioengineering*, vol. 19, no. 4, pp. 596-600, 2010. [Online] Available: https://www.radioeng.cz/fulltexts/2010/10_04_596_600.pdf

[21] M. Ijaz, Z. Ghassemlooy, J. Pesek, O. Fiser, H. Le Minh and E. Bentley, "Modeling of Fog and Smoke Attenuation in Free Space Optical Communications Link Under Controlled Laboratory Conditions," *Journal of Lightwave Technology*, vol. 31, no. 11, pp. 1720-1726, June 2013, DOI: 10.1109/JLT.2013.2257683.

[22] M. Ninos, H. Nistazakis, and G. S. Tombras, "On the BER performance of FSO links with multiple receivers and spatial jitter over gamma-gamma or exponential turbulence channels," *Optik*, vol. 138, pp. 269-279, June 2017. DOI: 10.1016/j.ijleo.2017.03.009.

[23] A. Stassinakis, H. Nistazakis, K. Peppas, G. S. Tombras, and L. Technology, "Improving the availability of terrestrial FSO links over log normal atmospheric turbulence channels using dispersive chirped Gaussian pulses," *Optics & Laser Technology*, vol. 54, pp. 329-334, Dec. 2013. DOI: 10.1016/j.optlastec.2013.06.008.

[24] G. K. Varotsos, H. E. Nistazakis, W. Gappmair, H. G. Sandalidis, and G. S. Tombras, "DF relayed subcarrier FSO links over Malaga turbulence channels with phase noise and non-zero boresight pointing errors," *Applied Sciences*, vol. 8, no. 5, pp. 1-15, April 2018. DOI: 10.3390/app8050664

[25] R. Miglani, J. S. Malhotra, A. K. Majumdar, F. Tubbal and R. Raad, "Multi-Hop Relay Based Free Space Optical Communication Link for Delivering Medical Services in Remote Areas," in *IEEE Photonics Journal*, vol. 12, no. 4, pp. 1-21, Aug. 2020, Art no. 7904621, DOI: 10.1109/JPHOT.2020.3013525.

[26] L. C. Andrews, and R. L. Phillips, *Laser beam propagation through random media*, 2nd ed. Bellingham, Washington, USA: SPIE press, 2005, pp. 1-773.

[27] L. C. Andrews, R. L. Phillips, and C. Y. Hopen, *Laser beam scintillation with applications*, 1st ed. Bellingham, Washington USA: SPIE press, 2001, pp. 1-368.

[28] I. Toselli, L. C. Andrews, R. L. Phillips, and V. Ferrero, "Free-space optical system performance for laser beam propagation through non-Kolmogorov turbulence," *Optical Engineering*, vol. 47, no. 2, pp. 1-9, Feb. 2008. DOI: 10.1117/1.2870113.

[29] S. A. Al-Gailani, A. B. Mohammad, M. S. Islam, U. U. Sheikh, and R. Q. Shaddad, "Tropical temperature and humidity modeling for free space optical link," *Journal of Optics*, vol. 45, no. 1, pp. 87-91, 2016. DOI: 10.1007/s12596-015-0300-7

[30] A. N. Stassinakis, H. E. Nistazakis, and G. S. Tombras, "Comparative performance study of one or multiple receivers schemes for FSO links over gamma–gamma turbulence channels," *Journal of Modern Optics*, vol. 59, no. 11, pp. 1023-1031, 2012. DOI: 10.1080/09500340.2012.697200.

[31] C. J. Engelbrecht and F. A. Engelbrecht, "Shifts in Köppen-Geiger climate zones over southern Africa in relation to key global temperature goals," *Theoretical and applied climatology*, vol. 123, pp. 247-261, 2016, DOI: 10.1007/s00704-014-1354-1.

[32] P. D. Tyson and R. A. Preston-Whyte, "Atmospheric circulation and weather over southern africa," in Weather and climate of southern Africa, 2nd ed. Cape Town, South Africa: Oxford University Press Southern Africa, 2000, ch. 12, pp. 176-217.

[33] M. O. Odedina, "A semi-empirical formulation for determination of rain attenuation on terrestrial radio links," Ph.D. dissertation, Sch. Elect. Electron. Comp. Eng., Univ. KwaZulu-Natal, Durban, South Africa, 2010.

[34] P. A. Owolawi, "Characteristics of rain at microwave and millimetric bands for terrestrial and satellite links attenuation in South Africa and surrounding islands," Ph.D. dissertation, Sch. Elect. Electron. Comp. Eng., Univ. KwaZulu-Natal, Durban, South Africa, 2010.

[35] M. Tadross and P. Johnston, , "Climate systems regional report: Southern Africa," ICLEI–Local Governments for Sustainability–Africa, Cape Town, South Africa, 105868-001, Aug. 2012, [Online]. Available: https://idl-bnc-idrc.dspacedirect.org/bitstream/handle/10625/50398/IDL-50398.pdf?sequence=1&isAllowed=y.

[36] M. Grabner and V. Kvicera, "Fog attenuation dependence on atmospheric visibility at two wavelengths for FSO link planning," *2010 Loughborough Antennas & Propagation Conference*, 2010, pp. 193-196, DOI: 10.1109/LAPC.2010.5666176.

[37] K. Fischer, M. Witiw, and E. Eisenberg, "Optical attenuation in fog at a wavelength of 1.55 micrometers," *Atmospheric Research*, vol. 87, no. 3-4, pp. 252-258, 2008, DOI: 10.1016/j.atmosres.2007.11.006.